1984

Barium titanium silicate thin films.

Michiteru. Ayukawa
University of Windsor

CANADIAN THESES

THÈSES CANADIENNES

NOTICE

AVIS

Canada

$Ba_2Si_2TiO_8$ THIN FILMS

by

Michiteru Ayukawa

A Thesis
Submitted to the Faculty of Graduate Studies and Research
Through the Department of Engineering Materials
in Partial Fulfillment of the Requirements for
the Degree of Master of Applied Science
at the University of Windsor

Windsor, Ontario

© 1983

797691

ABSTRACT

Fresnoite ($Ba_2Si_2TiO_8$) ceramic disks for the sputtering target were sintered. Using the ceramic targets, thin films of $Ba_2Si_2TiO_8$ were fabricated by means of both R.F. diode-magnetron and R.F. triode sputtering-deposition techniques.

Pure $Ba_2Si_2TiO_8$ ceramics were obtained when the green disks with the stoichiometric composition were sintered at $1250^\circ C$ for 5 hours. The composition of sintered $Ba_2Si_2TiO_8$ ceramics was analysed by means of both energy-dispersive spectrometry and x-ray fluorescence analysis. When the composition of a green powder mixture was off-stoichiometric by 5wt% in the concentration of any one of $BaCO_3$, SiO_2 and TiO_2, coexistence of a second phase such as $BaTiO_3$ or SiO_2 with the $Ba_2Si_2TiO_8$ phase was observed. c-axis oriented thin films of $Ba_2Si_2TiO_8$ were deposited on a single crystal NaCl (200) cleaved surface heated at $170^\circ C$. On the other hand, thin films deposited at the same substrate temperature on window glass and fused quartz substrates had amorphous structures. The amorphous-to-crystalline transition temperature of $Ba_2Si_2TiO_8$ thin films deposited on fused quartz substrate was found in the temperature range between 700 and $800^\circ C$. A novel method for evaluating the degree of crystallinity in partially crystallized thin films using x-ray diffraction patterns was developed and applied for specimens annealed at temperatures 800, 900 and $950^\circ C$.

Average sizes of crystallites in partially crystallized specimens annealed at 800 and 950°C were ~180 and ~250 Å, respectively, according to the Scherrer formula applied to the 201 and 002 diffraction peaks. Both c-axis oriented crystalline and amorphous films sputter-deposited from a pure $Ba_2Si_2TiO_8$ target had compositions very close to the stoichiometric one. In the present experiment, the maximum thickness of sputter-deposited thin films was limited to about 4000Å due to various experimental factors.

ACKNOWLEDGEMENTS

TABLE OF CONTENTS

ix

LIST OF TABLES

CHAPTER I

INTRODUCTION

A considerable advance has taken place in electrical and electronics technology in the past two decades, both in basic research and its commercial applications. As a result, efforts are being devoted to the development of appropriate electronic materials to meet a wide spectrum of applications.

The technical interests have also been rewarded in the field of thin film technology in the form of useful inventions such as a variety of active and passive microminiaturized components and devices, solar cells, radiation sources and detectors, magnetic memory devices, interference filters, etc.

Piezoelectric crystalline thin film has been widely studied and produced in the past two decades. Piezoelectric thin films are of great interest in a number of applications because of their electrical, optical, and acoustic properties. Their applications include transducers, surface acoustic wave (SAW) devices such as TV-IF filters, oscillators, convolvers, optical image scanners, and various other acousto-opto devices. In 1963, N.F. Foster (1) introduced a thin film of CdS for an ultrasonic transducer in VHF and UHF bands. This was the first fabrication of piezoelectric thin film by vapour deposition technique. In 1965, ZnO thin film was produced by reactive sputtering (2). ZnO film has been utilized as a most effective piezoelectric film since its

1

first productions. AlN film was deposited on sapphire sub-
strate at high temperatures in 1968 (3). AlN film is now
available for an ultrasonic transducer in UHF bands.
Recently it was reported that AlN axis-controlled thin films
were obtained by the magnetron sputtering technique even at
room temperature(4). In 1969, $LiNbO_3$ piezoelectric crystal-
line film was produced both on fused quartz and sapphire
substrates by means of a D.C. triode sputtering deposition
technique (5). It was reported that even c-axis oriented
complex compound crystalline film can be obtained by the
sputtering deposition technique (6).

Applications of the c-axis oriented piezoelectric
thin film are not only for the substitution of piezoelectric
single crystals and ceramics, but also for its excellent
characteristics in ultrasonic signal processing devices.
Furthermore, it may be possible in future that semiconductor
circuits will be monolithically integrated with the piezo-
electric thin film device.

In the present research on a metallic oxide called
Fresnoite ($Ba_2Si_2TiO_8$ abbreviated as BST henceforth)has been
sputter deposited in order to obtain a new piezoelectric
thin film.

BST was originally found in a mineral form (7). It
has a noncentrosymmetric tetragonal structure
which permits the appearance of piezoelectricity (7,8,9).
Single crystals of BST were grown by means of Czochralski
method independently by two groups (10,11). The various

material constants were measured (12,13,14). Characteristics
of SAW's on various cut-planes of the BST single crystal
were calculated by H. Yamauchi (14).

SAW characteristics of the BST thin film deposited on
a fused quartz substrate, having the c-axis perpendicular to
the substrate, was also theoretically studied by H. Yamauchi
et al. (15). It was concluded that the characteristics of
the fundamental modified Rayleigh wave (one of possible SAW
modes) on (z-45°Y-BST)/(Fused quartz)*should be excellent in
a range of kh from 2.0 to 3.2 (where k is the wave number
and h is the layer thickness): the electromechanical coupling
factor = 0.0158 - 0.0165, and the temperature coefficient of
delay = 0 - 25 x 10^{-6}/k. This has motivated the present
research for the fabrication of c-axis controlled BST thin
films.

7

---

* SAW on a Z plane, of BST thin film deposited on a fused
  quartz substrate, with a wave propagation at 45° to the
  Y axis.

CHAPTER 2

LITERATURE SURVEY

2.1 Piezoelectricity

Piezoelectric effects were first discovered by Jacques and Pierre Curie in 1880. If a mechanical stress such as tension or pressure is applied to a piezoelectric crystal, it produces an electric polarization or voltage whose magnitude is proportional to the applied stress. This is known as the direct piezoelectric effect. On the other hand, when an electric field is applied to a piezoelectric crystal, it causes strain and produces stress. This is known as the converse piezoelectric effect. Both of these are called piezoelectric effects. There is a linear relation between the components of the strain or stress and electric field or polarization. This phenomenon is called electromechanical coupling. Recently, such piezoelectric materials have been widely applied to surface-acoustic-wave (SAW) devices.

2.1.1 Piezoelectric Relations

The piezoelectric relations are derived from thermodynamic relations. The piezoelectric-strain constant· $\underset{\sim}{d}$ relates a vector (or first-rank tensor), namely electric field, $\vec{E}$, or electric displacement, $\vec{D}$, to a second-rank tensor, namely strain, $\underline{S}$, or stress $\underline{T}$. Strain has contributions not only from the piezoelectric effect but also from the applied stress via elastic compliance tensor, $\underset{\sim}{s}^{E}$ (when applied electric field $\vec{E}$ is kept constant) which is a fourth-rank tensor:

$$S_\lambda = s_{\lambda\mu}^E T_\mu + d_{i\lambda} E_i , \qquad (1)$$

where "matrix notation" ($\lambda, \mu = 1, 2, \ldots 6$) as well as "tensor notation" ($i, j = 1, 2, 3$) are employed. Note that Einstein's summation convention is used in Equation (1) and will be employed hereafter. Electric displacement receives contributions from the piezoelectric effect as well as the external electric field via dielectric constant, ε^T (for isothermal condition) which is a second-rank tensor:

$$D_i = d_{i\lambda} T_\lambda + \varepsilon_{ij}^T E_j, \qquad (2)$$

where suffixes have the same meanings as in Equation (1). If piezoelectric-stress constants, $\underset{\sim}{e}$ are utilized, the following relations are obtained:

$$T_\lambda = c_{\lambda\mu}^E S_\mu - e_{i\lambda} E_i, \qquad (3)$$

$$D_i = e_{i\lambda} S_\lambda + \varepsilon_{ij}^S E_j, \qquad (4)$$

where $c_{\lambda\mu}^E$ are the elastic stiffness tensor elements measured with the external electric field, $\vec{E}$, being kept constant and ε_{ij}^S are the dielectric constant tensor elements measured under an abiabatic condition.

From relations given by Eqs. (1) and (2), and Eqs. (3) and (4), piezoelectric constants, $\underset{\sim}{d}$ and $\underset{\sim}{e}$ are obtained:

$$d_{i\lambda} = \left(\frac{\partial S_\lambda}{\partial E_i}\right)_{\underset{\sim}{T}, \{E_{j\neq i}\}} = \left(\frac{\partial D_i}{\partial T_\lambda}\right)_{\vec{E}, \{T_{\mu\neq\lambda}\}}, \qquad (5)$$

$$e_{i\lambda} = \left(\frac{-\partial T_\lambda}{\partial E_i}\right)_{\underset{\sim}{S}, \{E_{j\neq i}\}} = \left(\frac{\partial D_i}{\partial S_\lambda}\right)_{\vec{E}, \{S_{\mu\neq\lambda}\}} \qquad (6)$$

where subscripts represent parameters being kept constant.
The interrelations of piezoelectric constants can be written
as follows:

$$d_{i\lambda} = e_{ij}s_{j\lambda}^{E} \qquad (7)$$

$$e_{i\lambda} = d_{ij}c_{j\lambda}^{E} \qquad (8)$$

where i, j = 1,2,3 and λ = 1,2,...,6.

The electromechanical coupling factor, k, is also an
important property of piezoelectric materials. The coupling
factor may be defined as the ratio of the mutual (elastic-
and-dielectric) energy density to the geometric mean of
the elastic and dielectric energy:

$$k = \frac{\bar{U}_m}{\sqrt{\bar{U}_e\bar{U}_d}} \qquad (9)$$

where $\bar{U}_m$ is the mutual energy, $\bar{U}_e$ is the elastic energy and
$\bar{U}_d$ is the dielectric energy. Note that k is not a scaler
but a tensor quantity. Actually the tensor element is
defined by:

$$k_{i\lambda}^{2} = \frac{d_{i\lambda}^{2}}{s_{\mu}^{E}\varepsilon_{ii}} \qquad (10)$$

The electromechanical coupling factor depends on the shape
of piezoelectric materials. For example, (a) if ferro-
electric ceramic disk is polarized along the direction of the
disk thickness (3-axis), the electromechanical coupling
factor for the wave resonating along a disk-diameter
direction (1-axis) is given by:

$$k_p^2 = \frac{2d_{31}^2}{\epsilon_{33}^T (s_{11}^E + s_{12}^E)} \tag{11}$$

and (b) when a ferroelectric ceramic thin plate is poled perpendicular to the plate surface (3-axis) the electro-mechanical coupling factor k_t for the wave resonating in the (thickness) direction (3-axis) is obtained as:

$$k_t^2 = \frac{h_{33}^2}{(\epsilon_{33}^S)^{-1} C_{33}^D} \tag{12}$$

where piezoelectric constant h_{33} is defined by:

$$h_{33} = (\frac{\partial T_3}{\partial D_3})_{S,D_1,D_2} = (\epsilon^S)_{3j}^{-1} e_{j3} \tag{13}$$

and $(\underset{\sim}{\epsilon}^S)^{-1}$ represents the inverse of $\underset{\sim}{\epsilon}^S$. It should be noted that for the piezoelectric resonance in the thickness direc-tion of a c-axis oriented polycrystalline thin film of $Ba_2Si_2TiO_8$ (see section 4.9.3), the formula given in Equa-tion (12) is applicable for the estimation of an electro-mechanical coupling factor.

2.1.2 Properties of Piezoelectric Materials

A necessary condition for the piezoelectric effects is the absence of a center of symmetry in crystal. It is known that the crystals which have a center of symmetry do not have piezoelectric effect (16).

All crystals may be classified into 32 groups; there are 20 groups which exhibit piezoelectric characteristics. The piezoelectric crystals can be classified into two

categories. One is for crystals which have a piezoelectri-
city by their original crystal structures. The other is for
ferroelectric crystals which have piezoelectricity only after
poling (i.e., applying high electric field) under the Curie
temperature. Single crystals of $Ba_2Si_2TiO_8$ (17) and zinc-
blend crystals such as ZnO, CdS and CdSe belong to the former
category. Perovskite crystals such as $BaTiO_3$ (18), $PbTiO_3$,
$PbZrO_3$ and $Pb(Zr,Ti)O_3$ (or PZT) (19) and ilmenite crystals
such as $LiNbO_3$ belong to the latter category. Note that, in
the present project, a non-ferroelectric but piezoelectric
material, $Ba_2Si_2TiO_8$, is investigated as a piezoelectric thin
film material.

2.2 Surface-Acoustic Waves (SAW) and Materials for SAW Devices

Surface acoustic waves (SAW) were discovered by Lord
Rayleigh in 1885. SAW's have both longitudinal and transversal
components in phase, propagating nondispersively along the
surface of materials as demonstrated in Figure 1 (20). For
example, earthquake sources produce such propagating waves
on the earth's surface. If the material has a piezoelec-
tricity, it can be applied to electronic devices. The
energy carried by the SAW on a piezoelectric material con-
tains a small amount of electric energy. This electric
energy gives the physical mechanism for the coupling of
electromagnetic signals and propagating SAW's. Such coupl-
ing is created at comb-shaped electrodes named interdigital
transducers (IDT) (21), as shown in Figure 1. SAW devices
have been utilized for analog signal processing in the
frequency range $10^7 - 10^9$ Hz. There are various types of

device applications such as bandpass filters, resonators, pulse compression filters, T.V. filters, radars, sonars, communication systems, non-destructive testing, acoustic microscopes and "ultrasound" image scanners.

2.2.1 Equations of SAW on Anisotropic Crystals

The theoretical solution of SAW propagation on an arbitrary (anisotropic) piezoelectric medium was originally introduced by Jones et al (22). The basic equations for the SAW propagation is, in standard tensor notation, given by (23):

$$\frac{\partial T_{ij}}{\partial x_i} = \rho \frac{\partial^2 u_j}{\partial t^2} \qquad \text{(Equation of Motion)} \qquad (14)$$

$$S_{k\ell} = \tfrac{1}{2} \left(\frac{\partial u_k}{\partial t_\ell} + \frac{\partial u_\ell}{\partial x_k} \right) \qquad \begin{array}{l}\text{(Linear Strain-Mechanical} \\ \text{Displacement Relations)}\end{array} \qquad (15)$$

$$\frac{\partial D_i}{\partial x_i} = 0, \quad E_i = -\frac{\partial \psi}{\partial x_i} \qquad \begin{array}{l}\text{(Derived from Maxwell's Equations} \\ \text{under the Quasi-Static Assump-} \\ \text{tion)} \end{array} \qquad (16)$$

$$T_{ij} = c^{E\,'}_{ijk\ell} S_{k\ell} - e'_{nij} E_n \qquad \text{(Linear Piezoelectric Relation)} \qquad (17)$$

$$D_m = e'_{mk\ell} S_{k\ell} + \varepsilon^{S'}_{mm} E_n \qquad \text{(Linear Piezoelectric Relation)} \qquad (18)$$

where T_{ij}'s are stress tensor elements, ρ is the mass density, u_j's are mechanical displacement, $S_{k\ell}$'s are the strain, D_i's are the electric displacement, E_i's are the electric field, and ψ is the electric potential. The primed quantities, such as the elastic constants ($c^{E'}_{ijk\ell}$), the piezo-electric constants (e'_{ijk}), and the dielectric constants ($\varepsilon^{S'}_{ij}$),

define a rotated coordinate system through the Euler trans-
formation matrix in which wave propagation will always be
along one direction. Note that Einstein's summation conven-
tion (over 1,2,3) for repeated indices is used.

From Equations (14) to (18), general equations for SAW
propagation are obtained:

$$c'_{ijk\ell} u_{k,\ell i} + e'_{kij} \psi_{,ki} = \rho \ddot{u}_j, \quad j=1,2,3 \qquad (19)$$

$$e'_{ik\ell} u_{k,\ell i} - \varepsilon'_{ik} \psi_{,ki} = 0 \qquad (20)$$

The dot notation indicates differentiation with respect to
time, while an index preceded by a comma indicates differ-
entiation with respect to a space. Equations (14)-(20) are
valid only inside the crystalline substrate, i.e., for $x_3 > 0$
in the coordinates defined in Figure 2 (20). This figure
also indicates the geometry under consideration and the
meaning of $\omega h = 0$, and $\omega h = \infty$ corresponding to a shorted surface
and a free surface, respectively.

2.2.2 SAW Characteristics of Materials

There are four major material characteristics for the
optimum design of SAW devices. They are: the velocity v_s,
the electro-mechanical coupling constant, k^2, (24) which can
be approximated by the quantity $2\Delta v/v$,
the temperature coefficients of delay (TCD), and the electro-
mechanical powerflow angle (PFA). The above quantities are
generally presented for various crystalline orientations as
continuous graphical functions of either direction of propagation
in the plane of a plate (Plates), as functions of the direction

of the plate normal (Boules), or for simultaneous rotation of both the plate normal and direction of propagation (Cylinders). For the above expressions, sets of Eulerian angles, λ, μ and θ which are defined in Figure 3 are used.

The quantity $2\Delta v/v_{\infty}$ (24) which is related to the electromechanical coupling factor is approximated by $2(v_{\infty} - v_{0})/v_{\infty}$, where v_{∞} is the SAW phase velocity for both mechanically and electrically free surface ($\omega h = 0$) and v_{0} is that for mechanically free but electrically shorted surface ($\omega h = \infty$) as shown in Figure 2. This quantity indicates the direct estimation of electromechanical coupling to interdigital transducers (25-26).

The temperature coefficient of delay (TCD) is defined as follows:

$$TCD = \alpha - \frac{1}{v_s} \frac{\partial v_s}{\partial T} \qquad (21)$$

where α is the thermal expansion coefficient along the SAW propagation direction, v_s is the SAW phase velocity and T indicates temperature.

The power flow angle (PFA), ϕ, is defined as the angle between the time average of electromechanical power flow direction and wave propagation as shown in Figure 4. Materials with the PFA equal to or nearly equal to zero are suitable for SAW devices. However, the electromechanical coupling and TCD parameters are more crucially important than PFA for the SAW device design.

Ideally, for SAW devices, the TCD should be zero and

the electromechanical coupling factor should be as high as possible. At present there are no such ideal materials; generally speaking, there is a trade-off relationship (27) between electromechanical coupling factor and TCD as shown in Figure 5 (14). Thus, a number of efforts have been made to develop new materials for SAW devices.

2.2.3 Materials for SAW Devices

Recent developments in SAW devices are remarkable. The attraction of SAW devices comes because the energy of a SAW is concentrated on the surface of the piezoelectric medium, so that the generation, detection and control of waves may be performed on the surface of a crystal (28). This makes it possible to produce SAW devices which have a planar structure so that the devices may be fabricated using the microelectronic device (or IC) technique.

There are three different types of piezoelectric materials used in SAW devices. They are single crystals, sintered ceramics, and thin films. Examples of each of these types of piezoelectric materials are discussed below.

2.2.3.1 Single Crystals

Quartz single crystal has been used in SAW devices for (narrow-band) signal processing. Quartz ST-cut*(29) and cut plane of ($\lambda=0^{\circ}$, $\mu=118^{\circ}$, $\theta=42.7^{\circ}$) (30), where (λ,μ,θ) are Euler's angles defined in Figure 3, have excellent temperature stability, i.e., TCD is nearly zero. The advantages of low cost fabrication and the availability of large single crystals makes this material good for mass

---

* cut plane and propagation direction of SAW with a zero TCD.

produced SAW devices. The only drawback is that its electro-mechanical coupling factor is quite low ($k^2 \sim 0.0018$) (30).

The 127.86° rotated Y cut x propagation of $LiNbO_3$ single crystal shows a reasonably high electromechanical coupling ($k^2 = 0.055$)[*](31). Several investigations for the choice of the cut plane have been made for $LiNbO_3$ single crystal(22)(32). However, the minimum values of TCD for $LiNbO_3$ is higher than that of quartz. $LiTaO_3$ single crystal indicates the best current compromise between electromechanical coupling and TCD. However, PFA for one of the best choices of cut plane, i.e., $(x \cdot 112^\circ Y)$[**](in which $k^2 = 0.0072$ and TCD=24 x 10^{-6}/K) is not exactly zero ($\sim 1.5^\circ$). A single-crystal growth technique for $LiTaO_3$ has already been developed (33). SAW characteristics of $Ba_2Si_2TiO_8$ (BST) were theoretically calculated (14) (See Figure 6). Parts of the calculated characteristics were experimentally confirmed (34). As shown in Figure 5, cut planes $(135^\circ Y \cdot x)$[**] and $(Z \cdot 45^\circ x)$[**] show good compromise between k^2 and TCD.

2.2.3.2 Piezoelectric ceramics

The piezoelectric ceramics have the highest electro-mechanical coupling factor among three types, i.e., single crystals, ceramics and thin films. The advantages (35) of piezoelectric ceramics compare to single crystals and thin films are:

1) the preparation process is easier than that of single crystals;

2) there are possibilities of various shape produc-

---

* Refer Figure 3.
** for exeample (X·Y); X=cut plane,Y=propagation direction.
   Ref.(20).

tions and the polarization axis can be selected;

3) the modification of their compositions and, therefore, characteristics for their purpose is relatively easy.

However, the piezoelectric ceramic for SAW devices are required to have a low dielectric constant, a non-porous structure and small TCD. Ito et al. has developed $(Pb_{1-3/2x+1/2z}Ndx)(Ti_{1-y-z}Mn_yIn_z)O_3$ ceramics with small TCD over a wide temperature range (36). This type of ceramic has very low porosity. Nevertheless, the loss is significantly high in such ceramics when operated in a high frequency range (100-300MH$_z$)

2.2.3.3 Piezoelectric Thin Film

The advantages of piezoelectric thin films are the following possibilities:

1) controlling the effective material constants by a suitable choice of layer- and substrate-materials;

2) controlling the piezoelectric characteristics of the layer by changing the layer thickness;

3) controlling the characteristics of devices (to which piezoelectric thin films have been applied) such as the electromechanical coupling and velocity by choosing a suit- able mode of acoustic waves, e.g., fundamental and first- order harmonic (modified stiffness) Rayleigh waves, Love wave, Sezawa wave, etc.;

4) controlling the piezoelectric characteristics of the layer by controlling the microscopic structure such as size and orientation of grains, local composition, etc.

5) application to devices for high frequency operation;

6) monolithic fabrication together with semiconductor devices, that is, applications to acousto-electronic devices such as convolvers;

7) relatively low cost fabrication.

A number of investigations have been made to fabricate piezoelectric thin films. The piezoelectric (or c-) axis of crystal should be oriented perpendicular to the substrate surface so that the thin film may have a piezoelectricity, even when a- and b-axes are randomly oriented in the plane parallel to the substrate surface. Presently, c-axis controlled ZnO thin film fabricated on a fused quartz substrate has been widely used. As a possible and promising piezoelectric thin film, fresnoite ($Ba_2Si_2TiO_8$) thin film has been proposed (15).

In the case of layer structured piezoelectric materials for SAW devices, the boundary conditions for theoretical calculations of SAW characteristics are different from the bulk case. All of the three SAW characteristics, namely, propagation velocity, v, TCD and electromechanical coupling factor, k^2, depend on the wave number, kh, normalized by the inverse of the film thickness, h. Therefore, the SAW characteristics for thin film layered on a bulk substrate depends directly on the thickness of the thin film. Usually four different electrical boundary conditions are considered:

a) both surface and interface are open. (The SAW velocity, v_s, is equal to v_∞^∞.)

b) the surface is shorted but interface is open. $(v_s = v_\infty^o)$;

c) the surface is open but the interface is shorted, $(v_s = v_o^\infty)$;

d) both surface and interface are shorted. $(v_s = v_o^o)$.

For all cases, the surface is mechanically free, and the interface keeps mechanical continuity from the layer to the substrate. Note that the symbols ∞ and o refer to electrically open and shorted conditions, respectively (15).

Using these four velocities, electromechanical coupling factors are approximated for four different arrangements of the interdigital transducer (IDT) and the short electrode, as shown in Figure 7.

$$k_a^2 \simeq 2(v_\infty^\infty - v_\infty^o)/v_\infty^\infty, \tag{22}$$

$$k_b^2 \simeq 2(v_\infty^\infty - v_o^\infty)/v_\infty^\infty, \tag{23}$$

$$k_c^2 \simeq 2(v_\infty^o - v_o^\infty)/v_\infty^o, \tag{24}$$

$$k_d^2 \simeq 2(v_o^\infty - v_o^o)/v_o^\infty, \tag{25}$$

where the subscripts a-d correspond to the arrangements (a)-(d) in Figure 7.

The TCD of a thin film layered system can be calculated using the phase velocities, $v_\infty (\equiv v_\infty^\infty)$ at different temperatures, T and T+ΔT:

$$TCD = \alpha - \frac{v_\infty(T+\Delta T) - v_\infty(T)}{v_\infty(T)\Delta T} \tag{26}$$

By assuming a perfect elastic junction at the interface, α is taken as a thermal expansion coefficient of substrate along the propagation direction.

2.2.3.4 $Ba_2Si_2TiO_8$ Thin Film

The single crystal of BST (point group 4 mm) is known as a piezoelectric crystal (7,10,11). SAW characteristics of a BST thin-layer structured device were theoretically predicted (15). Such an SAW device consists of a c-axis oriented BST thin-film layer fabricated on a fused quartz. (The c-axis of the BST crystallites must be oriented perpendicular to the substrate).

The calculated v_∞^∞, v_∞^O, v_O^∞ and v_O^O for BST layers on fused quartz substrate with respect to kh (in which k is the wave number and h is the layer thickness) are shown in Figure 8. As kh increases, v_∞^∞ decreases monotonically from the value of the Rayleigh wave velocity on fused quartz to that of the stiffened Rayleigh wave on the surface (z.45OY) of BST bulk. The velocity $v_\infty^{\infty(1)}$ for the first-order harmonics of the Rayleigh wave exists for the kh larger than 4.05 and decreases monotonically as kh increases. Using the calculated values of v_∞^∞, v_∞^O and v_O^O, and Equations (22)-(25), electromechanical coupling factors k_a^2, k_b^2, k_c^2 and k_d^2 for cases (a)-(d) defined in Figure 7 were obtained as shown in Figure 9. The calculated results of these electromechanical coupling factors were compared (15) to those of ZnO thin film fabricated on the fused quartz substrate. It is shown in Figure 9 that BST is not most suitable for very

thin film devices (kh<0.7) in contrast to the case of ZnO thin film, in which k_c^2 and k_d^2 have maxima (~0.008) at kh = 0.2. The maximum values of k_a^2 was equal to 0.0165 at kh = 2.8. This was 22% larger than k^2 for (z·45°Y) BST bulk, and also than that for a ZnO thin film. The TCD's for fundamental modified Rayleigh wave and the Love wave are shown in Figure 10. The minimum of TCD (for Rayleigh wave) was found at kh = 0.4 and then TCD increased to the value of the (z·45°Y) BST bulk (=52 x 10^{-6}/k) as kh increases. Thus, it is zero at kh = 2.05. The TCD for the Love wave can also be zero at kh = 0.7.

Thus it was concluded that characteristics of the fundamental modified Rayleigh wave for Z·45°Y BST thin film on fused quartz substrate were found to be excellent when kh = 2.0-3.2, where k_a^2 = 0.0158-0.0165, and TCD = 0-25x10^{-6}/ K. The above characteristics were predicted for the case in which the thin film is of a BST single crystal. However, it may well be expected that c-axis oriented polycrystalline thin films of BST have similar characteristics to those of BST single crystal thin films (15).

2.3 Sputtering Deposition

The sputtering phenomenon, which is the ejection of atoms or clusters of molecules from the surface of a target material by collision with energetic particles such as ions and high speed electrons, has been known for more than one hundred years (since 1852) and applied for film deposition. Because of the high pressure of gas used and high sensiti- vity to contamination in commonly used glow-discharge

sputtering, the technique was termed "dirty". However,
improved technology and new variants of sputtering arrange-
ments have now revived low-pressure sputtering deposition
as a versatile and powerful deposition technique for both
research and production purposes.

In 1965, an R.F. sputtering technique which sputter-
deposited even insulator target materials was developed
(37). Afterwards, sputtering sources other than the diode
gun such as the magnetron and the triode-guns were developed.
The development and improvement of sputtering deposition
techniques are remarkable so that the sputtering deposition
is one of the most excellent techniques for thin film fab-
rications.

The advantages of the sputtering deposition technique
(compared to the vapour deposition) are:

1)   strong adhesion between deposited film and
       substrate;

2)   possibility to deposit high melting point mater-
       ials;

3)   fabrication of wide homogeneous film;

4)   possibility of long deposition operation;

5)   good reproducibility of films.

Therefore, sputter deposited films are utilized for various
electronic devices such as surface acoustic wave (SAW)
devices. However, for the fabrication of piezoelectric
thin films for SAW devices, c-axis of the crystal must be
oriented perpendicular to the substrate surface. There

have been a number of attempts by different researchers to obtain c-axis orientation controlled films of ZnO (38)-(41), AlN (4,42), PZT (43,44) and PLZT (45) using sputtering deposition techniques. It was also reported (6) that even c-axis oriented complex compound crystalline ($K_3Li_2Nb_5O_{15}$ and $Pb_2KNb_5O_{15}$) films could be obtained by R.F. diode sputtering deposition. Fabrication conditions for these piezoelectric thin films are listed in Table A.1. In this work, the following experimental variables were controlled:

1) substrate temperature;

2) deposition rate;

3) choice of the substrate material, e.g., sapphire, platinum, NaCl, glass or fused quartz.

CHAPTER 3

EXPERIMENT (CERAMIC TARGET FABRICATION)

3.1 Introduction

Fresnoite is used as a target material in the present
research. The object   is to establish the fabrication
procedure of fresnoite target for sputtering deposition.
Fresnoite was originally found during a geological study of
Sanborinite deposits in eastern Fresno County, California
in 1965 (7).

3.1.1 Crystal Structure of Fresnoite (BST)

Fresnoite is a body-centred tetragonal (P4bm) with a
chemical formula, $Ba_2Si_2TiO_8$. (Fresnoite will be referred to
as BST hereafter.)   Lattice constants of BST
are a = 8.52Å and c = 5.21Å (9). Figure 11(a) shows the
structure of BST projected on the (001) plane. Silica
tetrahedra share one oxygen from independent pyrosilicate
groups. Barium atoms are surrounded by ten oxygen atoms,
six atoms of which are near neighbours, and four atoms are
more remote. The titanium is coordinated to five oxygen
atoms (8,9,46). Both the X-Y (8,9,46) and X-Z planes (47) of
BST structure are shown in Figures 11(a') and (b) by using
calculated interatomic distance relations which are given
in Table 1 (46). Figures 11(a)-(b) show that the BST
crystal structure is symmetrical in the X-Y plane, but not
in the X-Z plane or the Y-Z plane. In the X-Z plane, the
center of positively charged ions (Ba^{++}, Ti^{4+} and Si^{4+}) is

21

at the midpoint of this plane. However, the center of negatively charged ions (O^{--}) occurs slightly below the midpoint. This means that centers of positive and negative charges do not coincide in the X-Z plane and also in the Y-Z plane. Thus a net electric polarization appears along the Z-axis. Materials·such as BST which possess this property are known as piezoelectric materials. As mentioned in the previous chapter, mechanical energy can be converted to electrical energy and vice versa in such materials.

3.1.2 Physical and Chemical Properties of Fresnoite

Physical and chemical properties of BST are tabulated in Table 2. Piezoelectric materials are used as filtering devices for electrical circuits and for frequency control applications like surface-acoustic-wave (SAW) devices. Previous calculations (15) have indicated that a layered structure of BST c-axis oriented thin film deposited on fused quartz substrate should have excellent SAW characteristics.

3.2 Fabrication of Fresnoite Sputtering Target

BST consists of three oxides: barium oxide (BaO), silicon dioxide (SiO_2) and titanium dioxide (TiO_2). The follwing relation shows the reaction of the formation of BST:

$$2BaO + 2SiO_2 + TiO_2 \rightarrow Ba_2Si_2TiO_8 \qquad (1)$$
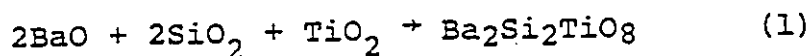
In the present research, barium carbonate ($BaCO_3$) was used in place of BaO in order to avoid the formation of $Ba(OH)_2$ agglomerates when water is added to the oxide

powder mixture. Thus, BaO due to its reaction with water results in poor mixing. The present experimental reaction, then, can be written as:

$$2BaCO_3 + 2SiO_2 + TiO_2 \rightarrow Ba_2Si_2TiO_8 + 2CO_2\uparrow \qquad (2)$$
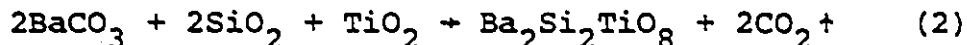
The fabrication procedure is shown in Figure 12, which is a modified version of the procedure originally developed by Hitachi Central Research Laboratory.

Step 1 $BaCO_3$*, SiO_2** and TiO_2*** powders were weighed in the stoichiometric proportions as required by the chemical formula $Ba_2Si_2TiO_8$ (see Table 3). The shape and the size of particles of each of these powders were observed by means of a scanning electron microscope, as shown in Figure 13. The particle sizes were 0.5–1.5μm for $BaCO_3$, 90–250μm for SiO_2 and 10–60μm for TiO_2 powder. In addition, specimens with three different off-stoichiometric compositions were prepared in order to compare with the stoichiometric speci- mens (see Table 4).

STEP 2 Weighed powders were thoroughly mixed with distilled water for 10 hours in a ball mill (JAR MILL, NORTON) (see Figure 14). The container jar and balls were made of "burundum", a sintered alumina commercially avail- able from NORTON U.S. Stoneware Inc.

---

* $BaCO_3$: Fisher Scientific Company, cat.no. B-30.

** SiO_2: Fisher Scientific Company, cat.no. S-662.

*** TiO_2: Fisher Scientific Company, cat.no. T-315.

STEP 3 After mixing the powders, the mixture was dried on a hot plate at about 100°C for 15 hours.

STEP 4 The dried powder mixture, which formed brittle cakes was hand-ground in a mortar to obtain fine powder of the mixture.

STEP 5 The powder was placed in an alumina crucible and hold in a furnace at 1000°C for 10 hours. This is the calcination or presintering process to get rid of CO_2 gas. This process is necessary in order to avoid porosity formation during sintering. Pre-sintered material was ground . to fine powder in the ball mill for 24 hours.

STEP 6 The same drying process was performed as STEP 3.

STEP 7 The powder was once again hand-ground using a mortar to a particle size in the range of 1 - 10μm .. The particle shape is shown in Figure 15. The powder was pressed into a disk of diameter 27.7mm and thickness 1.6mm at the pressure of 3.45 MPa.

STEP 8 Specimen disks were sintered at 1250°C for 5 hours in a high temperature furnace with molybdenum disilicide heating elements (KANTHAL SUPER N). The furnace temperature was increased at a rate of ~80°/hr. A thermocouple was placed just beside the specimen disks for precise temperature measurement. Another specimen with stoichiometric composition was sintered at 1280°C for comparison with the specimen sintered at 1250°C. Sintering conditions for other specimens prepared at different sintering tempera-

tures are listed in Table 4.

3.3 Analysis of Fresnoite Ceramics

Each specimen was analyzed by x-ray diffraction technique (XRD)*, energy dispersive spectrometry (EDS)** and scanning electron microscopy (SEM).***. The average composition of specimen T1 listed in Table 4 was determined using an x-ray fluorescence analyzer (XRF)****.

3.3.1 X-ray Diffraction Analysis

In order to determine coexisting phases and their crystal structures in the specimen, XRD method was employed. Monochromated CuK_α (λ = 0.15418 nm) radiation (from a Cu x-ray tube operated at 40kV and 20mA) was used. Diffracted x-rays were detected by a counter connected with a chart recorder with a scanning rate of 2°/min. Diffraction peaks was identified using the ASTM Diffraction File Cards.

3.3.2 Energy Dispersive Spectrometry Analysis

Quantitative analysis of sintered ceramics was performed using an EDS at an operating voltage of 15KeV (counting time: 60 seconds).   SEM was used in order to observe the effectiveness of sintering and microstructural feature of the ceramics. The specimens were coated with carbon to prevent electrical charge build up on the specimens.

---

*   XRD: Philips Model PW1011/60.

**   EDS: Kevex Model 5100 XR ES

***   SEM: Nanolab 7 SEMCO.

****   XRF: Philips 1410.

3.3.3 X-Ray Fluorescence Analysis

X-ray fluorescence analysis was conducted in order to obtain a more precise quantitative chemical analysis of Ba and Ti. CrK_α x-ray beam whose wavelength is 0.2291 nm (generated at the operation condition of 50kV and 40 mA) was utilized. The counting time was 100 seconds for the SiK_α peak $(2\theta = 32.12^{\circ})$ and 40 seconds for both the TiK_α peak $(2\theta = 86.26^{\circ})$ and the BaL_α peak $(2\theta = 87.29^{\circ})$.

3.4· Result and Discussion

3.4.1 X-Ray Diffraction

A diffraction pattern for each specimen was obtained using the same conditions.

The same peaks were observed in Specimens T1 and T2 of the stoichiometric composition (Figure 16(a)). Extra peaks were observed in addition to the peaks listed in the ASTM Card for BST (7), which are illustrated in Figure 16(e). Extra weak peaks at $2\theta = 31.0^{\circ}$ and 51.0° were found to correspond to those from barium titanate ($BaTiO_3$) whose diffraction peaks are shown in Figure 16(f).

Specimen T3 showed exactly the same diffraction pattern as pure BST, shown in Figures 16(b) and (e). For Specimen T4, the diffraction pattern indicated a mixing of BST and $BaTiO_3$ as shown in Figure 16(c). Specimen T5 did not sinter well at $1250^{\circ}C$. The diffraction pattern was almost the same as that of $BaTiO_3$, although there were extra peaks which corresponded to those of BST (Figure 16 (d)).

The actual diffraction patterns of Specimens T1, T3, T4 and T5 are shown in Figures 17 (a) to 17(d).

The above experimental observations .. indicate the following phase relations at $1250^{\circ}C$ at three different compositions, T3, T4 and T5 in the $BaO-SiO_2-TiO_2$ ternary system:

(1) At composition T3 (36.4 mol%BaO-45.4mol%SiO_2-18.2mol%TiO_2), no crystalline phases other than BST exist. However, it is most likely that amorphous SiO_2 phase does coexist with BST because the microscope observation (cf. sec. 3.4.3) shows an amorphous glassy coating of grain particles.

(2) At composition T4 (37.2mol%BaO-37.2mol%SiO_2-25.6mol%TiO_2), small amount of $BaTiO_3$ coexists with BST.

(3) At composition T5 (41.8mol%BaO-38.8mol%SiO_2-19.4mol%TiO_2), the dominant phase was $BaTiO_3$ but BST was also found to coexist.

3.4.2 Energy Dispersive Spectrometry

Energy dispersive spectra of Specimens T1-T5 were measured by EDS. Actual spectra are shown in Figures 18(a)-(e). Quantitative data of EDS are given in Table 5. A peak at 1.65 KeV was identified as a superposition of Si (K_{α}) and (K_{β}). Peaks located in the energy range 4.2-5.2 KeV are considered as superposed peaks of $Ba(L_{\alpha})$, (L_{β}), (L_{γ}) and Ti (K_{α}) and (K_{β}). Therefore, the ratio of integrated intensities of Si peak and (Ba+Ti) peaks was used as a relative index of the composition. Results are tabulated in Table 5.

3.4.3 Scanning Electron Microscopy

SEM micrographs of Specimens T1-T5 are shown in Figures 19-23. Grains of ~2µm diameter were formed in Specimen T1 after 5 hours sintering at 1250°C, as shown in Figure 19. Specimen T2 (sintered at 1280°C) contained a well crystallized structure as shown in Figure 20. The micrograph also showed an orientational crystal growth. It is important to mention that, in spite of a well crystallized structure in Specimen T2, the specimen was not able to be used as a target, because it was heavily warped. Specimen T3 contains grains coated with glassy material (Figure 21). This might be due to amorphous SiO_2 which was present in this specimen but could not be detected by x-ray diffraction. It is therefore not suitable for a sputtering target. SEM micrographs Specimen T4 (Figure 22) showed interconnected small grains with significantly large porosity. It seems that the sintering at 1250°C for 5 hours was not sufficient to have a disk with near zero porosity. Specimen T5 was hardly sintered as shown in Figure 23.

As previously found in the XRD study, Specimen T5 contained significantly large amounts of $BaTiO_3$. Thus, it seemed that, once the $BaTiO_3$ phase was formed, sintering at 1250°C for 5 hours was not sufficient to obtain a rigid solid body.

In Figure 24, Specimens T1, T3, T4 and T5 are colour-photographed. The difference in their colour corresponds to the

difference in composition.

3.4.4 X-ray Fluorescence Analysis

X-ray fluorescence analysis technique was used in order to overcome the difficulty of a quantitative estimation of Ba and Ti by means of EDS.

Specimen T1 was compared with a "standard" specimen A, whose composition (in wt%) was:

Specimen A - $BaO:SiO_2:TiO_2$ = 60.85:23.49:15.66

In order to increase reliability of the analysis, a test specimen, B, whose composition (in wt%) was slightly different from the standard A, was prepared.

Specimen B - $BaO:SiO_2:TiO_2$ = 59.94:25.22:14.84

Quantitative compositions of the standard specimen A, the test specimen B and Specimen T1 are shown in Table 6. The Analyzed composition of Specimen T1 disk was almost identical with the initial composition of the oxide powder mixture, of which the disk of Specimen T1 was made. Therefore, it was almost certain that Specimen T1 had the BST stoichiometric composition. Note that SiO_2 concentration in the disk of Specimen T1 was slightly lower than that in the powder mixture. The reason for this might be that SiO_2 powder had initially contained water molecules which evaporated out of the powder mixture while it was presintered and therefore the relative concentration of SiO_2 was shifted.

CHAPTER 4

EXPERIMENT (SPUTTERING DEPOSITION)

4.1 Sputtering Deposition System

The phenomenon of ejection of atoms from the surface of a target material by bombardment with energetic particles is called "Sputtering". The ejected or sputtered atoms can be condensed on a substrate to form a thin film. Sputtering has been known and exploited for deposition of films for many years. In recent years, the technology and new variants of sputtering arrangements have developed and improved, and almost all of materials can be sputtered. It is one of the most powerful deposition techniques for both research and production.

4.1.1 R.F. Triode Sputtering Deposition System (at University of Windsor)

A sputtering deposition system was assembled by High Vacuum Systems, Inc., (see Figure 25). The system consists of a vacuum chamber, a roughing pump, a high vacuum pump, sputtering sources and R.F. and D.C. power supplies for sputtering sources, as shown in Figure 26.

A) Vacuum Chamber

The vacuum chamber is a vertical cylinder type, fabricated by non-magnetic stainless steel (Type 304). There are two windows to observe the inside of the chamber and cooling coils are mounted on the chamber to keep it at or near ambient temperature.

30

B) <u>Pumping System</u>

a) <u>Roughing Pump</u> - The roughing pump has a rotary vane pump for roughing the chamber and backing the high vacuum pump. A vacuum of about 10^{-2} Torr from atmospheric pressure can be obtained in 5 minutes with this pump.

b) <u>High Vacuum Pump</u> - The high vacuum pump is an oil diffusion pump which has an integral water baffle, a liquid nitrogen trap and a high vacuum valve. A vacuum of 10^{-6} Torr from 10^{-2} Torr can be evacuated in about 30 minutes. The variable orifice valve is set above the diffusion pump assembly for precise control of gas throughput from the sputtering chamber.

C) <u>Sputtering System</u>

a) <u>General</u> - The sputtering system consists of two sputtering sources, one set of filaments, anode, R.F. power supplies and three variable leak gas control valves.

b) <u>Sputtering Sources</u> - L.M. Simard Inc. Tri-Mag. Model 3121 sputtering sources are utilized for this system. The sources accept targets of variable diameter up to 2.54 cm. The sources are mounted on the bottom of the chamber whose substrate holder is above the sources. Source configuration is shown in Figure 27. Thus, the sputter-up mode configuration is performed in order to eliminate sputter dust problems.

c) <u>Substrate Holder</u> - Substrate holder is a stainless steel plate with four substrate holder holes. The size of each hole is 75 x 75 mm. The holder plate can

be rotated from outside the chamber, so that the substrate
position may be adjusted. The distance between the substrate
and the target is also adjustable. Substitute holding
pieces were designed in order to mount various shapes of sub-
strates. The holder design is shown in Figure 28.

D) Substrate Heating Device

The substrate heating device was designed in order to
study the effect of substrate temperature on epitaxial growth
of thin films. A.C. power was not utilized because of its
interaction with R.F. power. Therefore, D.C. power supply
with a variac was connected to ceramic heater used for such
a purpose. Alumel-chromel thermocouple was placed on the sub-
strate for an accurate measurement of the substrate tempera-
ture. The substrate holder and the heater were covered with an
Aluminum foil to eliminate heat loss into the chamber. The
substrates were heated and cooled very slowly before and
after sputtering to avoid thermal shock. Gradual cooling
was also found beneficial in preventing film separation from
the substrate.

E) Argon and Oxygen Gas Supply

Three gas flow control valves are provided in the
system, one for varying the Argon gas flow to each source
and one for the oxygen gas flow to the substrate local
area.

4.2 Sputtering Methods

There are various sputtering methods in use which
offer a wide range of structure and configuration of elec-

trodes in sputtering sources.

4.2.1 Diode Sputtering

Figure 29(a) shows a schematic configuration of target and substrate for diode sputtering. This is a standard and simple sputtering deposition method. Since diode sputtering is operated at a relatively low vacuum with the gas pressure of $\sim 10^{-2}$ Torr, there is a possibility of contamination from the gas in the chamber. Another problem of this method is that the substrate temperature is difficult to be controlled because thermal radiation and high speed electron collisions to the substrate increase the substrate temperature to several hundreds of degree. It is also a problem that the deposition rate is relatively low with this method.

4.2.2 Triode Sputtering

In a triode sputtering system there is a third electrode to achieve a higher plasma density. Figure 29(b) shows a schematic diagram of a triode sputtering source. Because of enough electrons supplied from the third electrode, a higher plasma density can be obtained. This makes it possible to start and conduct sputtering deposition at a relatively low pressur ($\sim 10^{-3}$ Torr) with a larger deposition rate than that for diode sputtering.

Plasma current and voltage are changeable independently.

4:2.3 Magnetron Sputtering

Since a magnetic field is applied perpendicular to the electric field, electrons move along a cycloidal path formed

on top of the target (see Figure 30).Sputtering occurs through the action of ions, not electrons, and the purpose of the magnetic field is to keep the electron current away from the target surface. It is also highly unlikely that ions will be repelled out of the target surface during one half of the voltage cycle. The surface voltage is likely to approach the mean value of the A.C. waveform.

4.2.4 R.F. Sputtering

R.F. (radio-frequency) triode sputtering is commonly used for insulator targets such as oxides and other types of ceramics. In this method, high R.F. voltage is applied between the target and the substrate at a moment when the target is negatively charged, the positive ions in the plasma hit the surface with a high speed. When the phase shifts by 90°, that is the target is now positively charged, the positive ions will be repelled out from the target so that the target surface remains electrically neutral.

4.3 Tri-Mag Model 3121 Sputtering Source

A) Description

Two Tri-Mag Model 3121 Sputtering Sources which were assembled by L.M. Simard, Inc. in Santa Barbara, California, were installed in the sputtering deposition system in the Department of Engineering Materials. They are Magnetron supported triode R.F. sputtering guns. A schematic figure of this type of triode sputtering source is shown in Figure 31. Two magnets are placed on both sides of sources so that charged particles or the plasma may be confined in the magnetic field with a high density. Other basic elements

of this source are a thermal-electron emitting filament, an
anode, a plasma-confining enclosure and a sputtering target.
The filament is heated by a high A.C. current (supplied from
Filament Module) to a temperature sufficiently high for ther-
mionic electrons to be emitted from its surface. These
electrons then are attracted to an anode biased positively
by a high voltage D.C. power supply (Igniter Module). Argon
gas atoms are led into the enclosure where they collide with
the accelerated electrons. If sufficient filament-anode
voltage, numbers of gas atoms and electrons are present, the
gas atoms will be ionized in their collisions with the
electrons, and a self-sustaining arc-type plasma will be
initiated. Control of plasma current is maintained with a
constant-current D.C. supply (Plasma Discharge Module). Con-
trol of the plasma voltage is achieved by the adjustment of
both argon gas flow and filament electron emission.

B) Target Installation

Target (BST Ceramic target in the present research)
was sintered into a disk shape of 23.8 mm diameter and 1.5
mm thickness and placed on a target holder for the level
adjustment of the target surface (see Figure 32). The
holder was made of 25.4 mm diameter copper rod in order to
have sufficient conduction of both heat and electricity.
The target and the Cu disk holder were soldered by silver
epoxy resin to ensure thermal and electric conduction. The
ring-shaped target insert (see Figure 33) to the confinement
cover, which is used for the adjustment of the target-

electrode spacing, was modified according to the target diameter. The hole in the center of the insert was sized to be 1.0 mm larger in diameter than the target. This gives a clearance gap between target and insert of 0.5 mm. If the clearance gap is much larger than this value, plasma will leak down to the target edge and sputter the target holder, thus contaminating the deposited film. The set target is shown in Figure 34.

4.4 Operating Procedure of Sputtering Deposition System

Detailed description of the operation procedure of the sputtering deposition system installed in the Department of Engineering Materials is given in Appendix A.

4.5 Diode Magnetron Sputtering Deposition System

An initial part of the present research project was carried out using a diode magnetron sputtering deposition system in the Physics Department at Queen's University. (No sputtering deposition systems were available at the University of Windsor at that time). It would be useful to give a description of the diode magnetron sputtering deposition system for a comparison with the triode sputtering deposition system presently available in the Department of Engineering Materials. A picture of the system at Queen's is shown in Figure 35. There are two sputtering sources vertically placed on the chamber wall. Each source requires a diameter of 100.0 mm. The most difficult problem in using this system is the fabrication of target with such a large diameter. Since

it was impossible to fabricate ceramic disks of 100.0 mm diameter and 2.0 mm thick, powder made of sintered BST ceramics was pressed onto an aluminum mount piece which was readily installed to the magnetron for Specimen Q5. For Specimens Q1-Q4, three oxides, namely $BaCO_3$, SiO_2 and TiO_2, were pressed onto aluminum mount piece such as Specimen Q5 target (see Table 7). Since the pressed powder was not firmly stuck to the mount piece, it was often found that significant amounts of the powder fell down during sputtering deposition.

4.6 System Operation and Specimen Fabrication

Operating conditions of the sputtering deposition system at Queen's University and the fabrication condition of Specimens Q1-Q5 are tabulated in Table 7. The operating conditions of the triode sputtering system installed in the Department of Engineering Materials are given in Table 8. Fabrication conditions of Specimens W1-W15 are listed in Table 9. The fabrication condition of each specimen is summarized in the (R.F.-power)-vs.-(substrate temperature) plot given in Figure 36.

Window glass, NaCl (rock salt) single crystal and fused quartz were used as substrate materials. The following procedure was employed to clean the window glass:

1) Glass plates (25 mm x 75 mm) were cleaned in an ultrasonic cleaner, first with distilled water and then with acetone.

2) These plates were put in a container such that they did not touch each other. Liquid isopropanol was

then put in the container and evaporated so that the vapour might clean the surface of each plate.

An NaCl single crystal was cleaved along a (200) plane to make thin plates (of 2~4 mm thickness) for substrates. In order to avoid additional contamination on the NaCl substrate, the cleavage was performed only when the substrate set-up was immediately ready.

4.7 Methods for Characterizing Fresnoite Thin Films

4.7.1 Film Thickness Measurement

Multiple beam interferometer (A-Scope, Model 980-4000, Varian) was used for the film thickness measurement. The instrument uses a sodium vapour lamp with an effective wavelength of 5892Å. The light is directed to a Fizeau plate as shown in Figure 37. The Fizeau plate contacts the specimen and is tilted at a small angle to form an air wedge. The interference fringe pattern produced in the air wedge is transmitted with the eyepiece hairline. Spatial relationships between the specimen, the Fizeau plate and the fringe line pattern are shown in Figure 37. The vertical distance or "spacing" between fringe lines is one-half wavelength (2946Å). The actual height of the surface variation is determined by the ratio of the fringe line "offset" and "spacing".

4.7.2 X-ray Diffraction Analysis

The structure of each film was analysed by x-ray diffraction method. CuK_α x-ray was used at the operating condition of 40kV and 20 mA. The scanning rate of the counter was 2°/min. (in terms of 2θ). The relative intensity

was recorded with the full scale selected from 100 c.p.s. to 400 c.p.s.

4.7.3 Energy Dispersive Spectrometry and Scanning Electron Microscopy

The compositions of specimen films fabricated on glass and fused quartz substrate were quantitatively estimated by Kevex, EDS (Energy Dispersive Spectrometry), attached to scanning electron microscope (Nanolab 7) installed in the Department of Engineering Materials. The same data analysis technique as described in Sec. 3.4.2 was employed.

4.8 Characteristics of Fresnoite Thin Films

4.8.1 Films Fabricated by Diode Magnetron Sputtering Deposition

X-ray diffraction analysis showed that Specimens Q1-Q4 have non-crystalline or amorphous structures. Specimens Q1-Q4 were found to remain amorphous even after annealing at 600°C. On the other hand, Specimen Q5 which indicated an amorphous structure in the "as-deposited" condition, showed small peaks at 2θ in the x-ray diffraction pattern equal to 25.8°, 33.2° and 37.3°. These peaks corresponded to the peaks of BST crystals 201, $211 - 002$ and $311 - 112$. Thus the crystallization temperature of the amorphous film (Specimen Q5) might be located about 600°C. SEM photographs of the annealed film (Specimen Q5) at 700°C are shown in Figure 38. The film, as shown in the micrograph, was flaked off due to substantial difference in the expansion coefficients of BST film and glass substrate. ($\alpha = \sim 10.0 \times 10^{-6}$/K

for BST (c.f. Table 2) and 4.5 x 10^{-6}/K for glass substrate).

4.8.2 Film Thickness

Film thickness of sputtered specimens are listed in Table 9. Figure 39 shows film thickness as a function of sputtering time for different R.F. power. Film thickness, in general, increased with sputtering time for a constant R.F. power as well as with R.F. power for a constant sputtering time. Although a thickness of about 10μm is most suitable for the measurement of piezoelectricity, films of such a large thickness were not possibly fabricated throughout the present research because of various kinds of limitations inherent in our triode sputtering system.

4.8.3 Diffraction Data

Diffraction patterns of all the specimens (in Table 9 except Specimen W12s) with glass and fused quartz substrates showed a single broad peak at around $2\theta = 25.0^{\circ}$ which indicated that they had amorphous structure in as-deposited condition. However, Specimen W12s which was sputtered on NaCl substrate heated at 170°C (see Table 9) had a 001 peak of BST at $2\theta = 15.8^{\circ}$ as shown in Figure 40. (Note that all of specimens W12g, W12q and W12s were fabricated in a single sputtering deposition as indicated in Table 9). It also had a large peak at $2\theta = 31.5^{\circ}$ which seemed to have come from an overlap of 002 peak from BST ($2\theta = 34.4^{\circ}$) and 200 peak from NaCl substrate ($2\theta = 31.5^{\circ}$).

Structural change from amorphous to crystalline state was studied as a function of annealing temperature using specimens sputtered on fused quartz substrates. Specimen

W12q fabricated on fused quartz substrate was used for this investigation. Eight annealing temperatures were chosen from $300^{\circ}C$ to $950^{\circ}C$ (see Table 10). Annealing at each temperature was done for 10 hours. Each annealed state was named W12x (where x = A,B,...,H or I), as shown in Table 10 and was analysed using the x-ray diffraction technique. Depending on the annealing temperature, three kinds of diffraction patterns were obtained, which are illustrated in Figure 41. For annealing temperatures lower than $700^{\circ}C$, only a broad diffraction peak or halo having its maximum intensity at $2\theta \cong 28.0^{\circ}$ is present (see the raw diffraction pattern in Figure 42(a)). Its full width of roughly 20° in 2θ is typical of an amorphous phase. Therefore, it may be concluded that no crystalline domains are present in BST films annealed below $700^{\circ}C$. Similar results were obtained for films sputtered on glass substrate. For specimens annealed at temperatures higher than $800^{\circ}C$, sharp Bragg peaks same as diffraction peaks of the target (see Figure 17 (a)) were observed superimposed on an amorphous broad peak as can be seen in Figures 42(b) and (c). This indicates the presence of microcrystals in the amorphous phase. The diffraction pattern of Specimen W12I which had been annealed at $950^{\circ}C$ (see Figure 42(d)) seemed to indicate the completion of crystallization. In the following sections, in order to put the above observation on a more quantitative basis, the degree of crystallinity and the average grain size of the microcrystals in annealed specimens will be

determined.

4.8.4 Degree of Crystallinity

It is assumed that the total sum of the integrated intensities of the narrow Bragg peaks is proportional to the number of atoms in the crystalline grains and that the area of the broad peak is similarly related to the atoms in the amorphous phase.

4.8.4.1 Separation of Superimposed Diffraction Peaks

In order to separate the two conditions, the narrow and broad peaks have been fitted with Lorentzian and Gaussian curves, respectively.

a) Lorentzian Distribution Function:

$$\frac{A_L}{B_L + (\eta - \eta_o)^2}$$

where A_L and B_L are constants to indicate height (A_L/B_L) and width at half-maximum intensity $(2\sqrt{B_L})$ of the peak, η is the angle variable and η_o is the location of the center of the peak.

b) Gaussian Distribution Function:

$$A_G \exp\{-B_G(\eta - \eta_o)^2\}$$

where A_G and B_G are constants to indicate height (A_G) and width at e^{-1}-maximum intensity $(2/\sqrt{B_G})$ of the peak, η is the angle variable and η_o is the location of the center of the peak.

Generally, this method is based on comparing the sum of integrated intensities of crystalline narrow peaks with

the integrated intensity of amorphous broad peak, at each annealing temperature. Since the specimen film thickness was thin ($\sim 3900 \overset{\text{o}}{\text{A}}$) there was a possibility of interference from the spectra of fused quartz substrate. The scattering efficiency or absorption factor, a, from fused quartz substrate was calculated by means of following equation:

$$I_t = I_f + aI_s \tag{1}$$

where I_t is the total intensity from BST film and substrate, I_f is the intensity from BST film and I_s is the intensity from fused quartz substrate.

If the x-ray with intensity I_o passes through the distance x, its intensity I_x becomes as follows:

$$I_x = I_o e^{-\mu x} \tag{2}$$

where μ is linear absorption coefficient. If the x can be taken as constant for a uniform thickness the above expression can be written, using the absorption factor a, as:

$$I_x = aI_o \tag{3}$$

It should be noted that a depends on the diffraction angle. But in the present analysis, a is assumed to be constant because the angles of peaks utilized in the analysis were not too low ($2\theta = 20^\circ - 80^\circ$) (See discussion in Appendix B).

The intensity from BST film, I_f, is as follows:

$$I_f = I_t - aI_s \tag{4}$$

It is assumed that the ratio of peak intensities from the BST film at two different diffraction angles 2θ and $2\theta'$ is identical with that of corresponding peaks from BST ceramic disk as long as 2θ and $2\theta'$ are larger than $\sim 60^\circ$ where the contribution from amorphous diffraction is negligible.

$$\left(\frac{I_T(2\theta)}{I_T(2\theta')}\right)_{\substack{BST \\ Ceramic}} = \left(\frac{I_f(2\theta)}{I_f(2\theta')}\right)_{\substack{BST \\ Film}} = \frac{I_t(2\theta) - aI_s(2\theta)}{I_t(2\theta') - aI_s(2\theta')} \quad (5)$$

For various combinations of peaks at high diffraction angles, the absorption factor was determined. The averaged absorption factor $\bar{a}$ (defined in Eq. (2)), at $800^\circ C$ was found to be 0.62 (See Table C-5 in Appendix C). Following the same procedure, $\bar{a}$ at $900^\circ C$ was found to be 0.67 (See Table C.6 in Appendix C). Therefore, it was decided to use 0.65 as the average absorption factor for specimens W12q. In order to evaluate the integrated intensities of diffraction peaks, the background intensity was subtracted from each peak intensity, recorded in the chart. As seen in Figures 42(b) and (c), the broad amorphous peak located in the 2θ angle region from 15.0° to 30.0° is superimposed with 200, 111 and 210 peaks from the crystalline region. These four peaks are to be separated by employing the Lorentzian and the Gaussian function as previously mentioned.

The theoretical intensity at diffraction angle $2\theta = \eta$, $I_{th}(\eta)$, may be given by:

$$I_{th} = \frac{A_1}{B_1 + (\eta - \eta_1)} + \frac{A_2}{B_2 + (\eta - \eta_2)} + \frac{A_3}{B_3 + (\eta - \eta_3)}$$

$$+ A_G \exp{-B_G(\eta - \eta_G)} \quad (6)$$

Here, the first three terms on the right

hand side stand for Lorentzian curves for the crystalline

diffraction peaks 200, 111 and 210. The last term is a

Gaussian curve for the amorphous peak. Quantities (A_1/B_1),

(A_2/B_2) and (A_3/B_3) are the maximum intensities of the

three sharp peaks, and A_G is the maximum intensity of the

broad amorphous peak. Quantity B_i (i = 1,2,3) is related to

the width of the Lorentzian peak and B_G with the Gaussian

peak. (See previous definitions of the distribution func-

tions). Quantities η_1, η_2 and η_3 are the central angles of

peaks 200, 111 and 210 and η_G is the angle of the maximum

intensity of the broad amorphous peak.

Twelve unknown parameters, i.e., A_i, B_i, η_i (i=1,2,3),

A_G, B_G and η_G, can be determined comparing I_{th} given in Fig-

ures 43 and 44 if an extended least-square method is utilized

to find a point in a twelve-dimensional space where the

square sum of errors, ΣE^2, is minimum. In the following,

the actual procedure employed for determining the twelve

parameters are described.

1) Approximate values or the initial values for all

of the twelve parameters were estimated from the experimen-

tal intensities. This was performed using the fact that

η_i (i=1,2,3) and η_G represented the angles at maximum inten-

sities of the corresponding peaks, and A_i, B_i (i=1,2,3), A_G

and B_G are related with peak heights and widths, as pre-

viously mentioned. Moreover it was assumed that the ratios

of heights of the three sharp peaks were identical with

those obtained from a pure BST ceramic specimen (specimen T1).

2) Values for η_i (i=1,2,3) obtained by eye-observation were assumed to be given constants because each of three peaks was sharp.

3) Since ambiguity in η_G was much greater than η_i (i=1,2,3), η_G was determined so that ΣE^2 becomes minimum when values of other parameters than η_G were kept at their initial values. Thus determined values were 21.55° for Specimen W12G and 21.54° for Specimen W12H.

4) An initial value for A_G was determined by using the value for η_G obtained above so that ΣE^2 might be at its minimum. The values obtained for A_G were 19.6 and 14.0 (in arbitrary units) for Specimens W12G and W12H. Similarly, using these values for B_G's for Specimens W12G and W12H were tentatively obtained at 0.189 and 0.262, respectively.

5) It was assumed that the ratio between the height (A_G) and the width $(2/\sqrt{B_G})$ was kept constant in the following refinement:

$$b = A_G/(1/\sqrt{B_G}) = A_G B_G^{\frac{1}{2}} = \text{const.}$$

That is, b = 8.521 and 7.166 for Specimens W12G and W12H, respectively. Similar shape relation was also assumed for each of the Lorentzian peaks:

$$c = (A_L/B_L)/\sqrt{B_L} = A_L B_L^{-3/2} = \text{const.}$$

To obtain c for each peak, the initial values for A_L's and B_L's were utilized.

6)   In order to reduce the number of independent variables, it was assumed that the ratio of the three Lorentzian peak heights was the same as that of corresponding peaks in the diffraction pattern from the BST ceramic. Thus:

$$\frac{A_1}{B_1} \Big/ \frac{A_2}{B_2} = \text{const.},$$

$$\frac{A_2}{B_2} \Big/ \frac{A_3}{B_3} = \text{const.},$$

and

$$\frac{A_3}{B_3} \Big/ \frac{A_1}{B_1} = \text{const.}.$$

7)   Now that only two independent variables, say A_1 and A_G, were left, it was straightforward to find the minimum of ΣE^2 by means of numerical calculations. · Computer programs used for these calculations are given in Appendix D.

Thus determined parameters were substituted back into I_{th} given by Eq. (6). Theoretical intensities, I_{th}'s are plotted vs. $\eta(=2\theta)$ in Figures 45 and 46 for Specimens W12G and W12H, respectively. Comparing these theoretical intensities given in Figures 45 and 46 with experimental ones given in Figures 43 and 44, it may be concluded that the values of the twelve parameters were quite reasonable.

4.8.4.2   Definition of Degree of Crystallinity

The degree of crystallinity is defined by the following equations:

D.C. (Degree of Crystallinity) $= \dfrac{L}{L+pG}$ (7)

in which,

$$G = \int_{-\infty}^{\infty} A_G \exp\{-B_G(\eta-\eta_G)^2\} d\eta = \sqrt{\pi}A_G/\sqrt{B_G} \qquad (8)$$

and,

$$L = \sum_{i=1}^{J} \int_{-\infty}^{\infty} \frac{A_i}{B_i + (\eta-\eta_i)^2} d\eta = \pi \sum_{i=1}^{J} A_i/\sqrt{B_i} \qquad (9)$$

where J is a number of Lorentzian peaks. Note that Lorentzian peaks are not limited to the three peaks considered above but there are many other peaks at high angle region of $\eta(=2\theta)$. It also stands for the number of Bragg peaks from crystalline BST. In the present case, J=17. In Eq. (7), p is the scattering efficiency ratio of Bragg peaks over amorphous peak.

4.8.4.3 Scattering Efficiency Ratio, p

Generally, total intensity I_o of Bragg peaks in polycrystalline materials consists of intensities from atomic arrangement I_{AA}, thermal vibration I_{TV} and atomic size difference I_{AS}.

$$I_o = I_{AA} + I_{TV} + I_{AS} \qquad (10)$$

In the case of amorphous state, background noise intensity, I_{ABG}, consists of diffuse scattering due to local atomic arrangement I_{DS}, thermal vibration I_{TV} and other noise I_{ON}:

$$I_{ABG} = I_{DS} + I_{TV} + I_{ON} \qquad (11)$$

In the case of crystalline materials, however, background noise, I_{CBG} consists of the following:

$$I_{CBG} = I_{TV} + I_{ON} \qquad (12)$$

Thus, the background intensity is higher for an amorphous state than a crystalline state. Since it is conventional to measure the integrated intensity with the background intensity subtracted, one may take the omitted background contribution into account by introducing different scattering efficiencies, P_C and P_A, for peaks from the crystalline portion and for those from the amorphous portion, respectively.

$$I_T^i = P_C I_C^i + P_A I_A^i \qquad (13)$$

where I_T^i stands for the total integrated intensity, and I_C^i and I_A^i are the integrated intensities (with the background subtracted) from the crystalline and amorphous region. In order to obtain the scattering efficiency ratio defined by:

$$p \equiv \frac{P_A}{P_C} \qquad (14)$$

data for I_C^i and I_A^i at two different temperatures, T_1 and T_2 may be utilized:

$$P_C I_C^{i(T_1)} + P_A I_A^{i(T_1)} = P_C I_C^{i(T_2)} + P_A I_A^{i(T_2)}$$

Thus:

$$p = P_A/P_C = \frac{I_C^{i(T_2)} - I_C^{i(T_2)}}{I_A^{i(T_1)} - I_A^{i(T_2)}} \qquad (15)$$

Using Equation (15), the scattering efficiency, p was calculated for each possible combination of T_1 and T_2 (Actually I_C^i's and corresponding I_A^i's were available for T=500,800,900 and 950°C, See Tables 11 and 12). The average of p's was obtained at 1.17.

4.8.4.4 Temperature Dependence of Degree of Crystallinity

The calculated degrees of crystallinity (D.C.) for specimens annealed at 700, 800, 900 and 950°C are listed in Table 13 and plotted vs. annealing temperature T_a (see Figure 47). This result apparently indicates that the crystallization temperature of BST thin film (of ~3900 Å thickness) is located between 700°C and 800°C.

4.8.5 Average Size of Crystallites

The second quantitative characterization derived from the x-ray data is the average size of crystallites. The Scherrer formula (48) was used for this analysis:

$$d_{(hk\ell)} = \frac{k}{\beta_{\frac{1}{2}} \cos\theta} \qquad (16)$$

where the crystalline dimension d, normal to the reflecting planes (hkℓ), is related to the width $\beta_{\frac{1}{2}}$ of the diffraction peak at half-maximum intensity, shape factor, k, is a constant related to the grain shape and θ is the diffraction angle. The quantity k assumes various numerical values ranging from 0.70 to 1.70, depending upon a number of factors. In the present analysis, k is assumed to be a constant. Therefore,

$$(d/k)_{hk\ell} = \frac{\lambda}{\beta_{\frac{1}{2}} \cos\theta} , \qquad (17)$$

where λ is the wavelength of CuK_{α} line equal to 1.5418Å.

Quantity (d/k) was calculated using 201 and 002 peaks.

Results are given in Table 14. In Figure 48, $(d/k)_{201}$ and

$(d/k)_{002}$ are plotted with respect to T_a.

4.8.6 Energy-Dispersive-Spectrometry Analysis and Scanning Electron Microscopy Observation

Energy dispersive spectrum for specimens W12g,s is

shown in Figure 49. The spectrum patterns are almost iden-

tical with that for target ceramics (Specimen T1, shown in

Figure 18(a)). This indicates that the composition of the

thin films (Specimen W12g,s) is close to the stoichiometric

composition of BST. Scanning electron micrographs were

taken for various specimens. As-deposited films on glass

and fused quartz specimens were smooth, continuous and trans-

parent. Films on NaCl single crystal substrate showed flat

but were cracked and some fragments were flaked off, as

shown in Figure 50. Figures 51 and 52 show films on fused

quartz substrate (Specimens W12H annealed at $900^{\circ}C$ and W12I

annealed at $950^{\circ}C$). Electron micrographs of the thin film

on glass substrate (Specimen 6g, c.f., Table 9) annealed

at temperatures 500, 550 and $700^{\circ}C$ are shown in Figure 53.

Wrinkles were observed in each micrograph. Their size

became larger as annealing temperature increased.

4.9 Discussion

4.9.1 Sputtering Deposition Systems

Since the target size required for the sputtering source (Simard Tri-Mag model 3121) installed in the sputtering deposition system (available at Department of Engineering Materials) can be flexible (up to 25.4mm diameter), this system is most suitable for sputter depositing new or "exotic" materials of relatively small amounts.

On the other hand, most of the commercially available magnetron sputtering sources which usually have much higher deposition rate than the Simard Tri-Mag 3121 sputtering source require targets of a large size (~100 mm diameter). Recently, a type of magnetron sputtering source, called S-gun has widely been utilized because of its high deposition rate even compared with the conventional magnetron sputtering sources. However, it requires a target of a special shape, and the fabrication of such a target with new material of relatively small amount is difficult.

A relatively large R.F. power (up to ~400W) can be supplied to the Tri-Mag 3121 sputtering source. However, since a BST target is an electrical insulator, and therefore, the accumulated electric charges on the target surface (even in the R.F. mode) caused a breakage of the target as shown in Figure 56 when a R.F. power higher than 120W was applied. Moreover, a long operation caused a burning-out of the filament (see Figure 31). Thus the maximum thickness, $t_{max} < 4000$ Å. There are possibilities for obtaining thicker films by using

the same Tri-Mag sputtering source. In order to prolong
the lifetime of a filament, it is essential to avoid a
sputtering of the filament by positively charged ions. This
may be realized by reducing the applied voltage between the
filament and the anode (see Figure 31). At the same time,
filament current must be increased to produce more electrons
so that the plasma generating efficiency may not be reduced.
It is known that the sputtering rate is much larger when a
metallic target is used than when an insulator ceramic is
used. It may be possible to perform a reactive sputtering
deposition of BST thin films using a metal target consisting
of Ba, Si and Ti metals or alloys and introducing oxygen
gas into the chamber.

4.9.2 Film Thickness

BST films sputter-deposited on both a window glass
and a fused quartz substrate were transparent and had a smooth
surface. However, since there were some fluctuations in the
measured film thickness, the thickness of each specimen was
measured at five different positions and the average of the
five values was taken. The fact that films fabricated on a
glass substrate were amorphous, would indicate that little
thermal diffusion of adatoms (which are atoms being adsorbed
on the substrate surface by losing kinetic energy) was taking
place on the substrate surface during the sputtering deposi-
tion. Therefore, the inhomogeniety in the film thickness
stemmed from the fact that the distance from the sputtering
source was not constant at each point on the substrate surface.

Actually, the sputtered film had the largest thickness at the centre and the thickness gradually decreased as one moved away from the centre. In the present work, it was not possible to fabricate films with thickness larger than 2.0µm as mentioned earlier. The fabrication of thick films (~10µm) is desired in order to study electronic properties of the BST thin film, such as dielectric constant, piezoelectric reson- ance and surface-acoustic-wave characteristics. This would be possible when either the lifetime of the filament inside the sputtering source or the sputtering rate is increased, as mentioned in the previous discussion.

4.9.3   c-axis Oriented BST Thin Films

In order to obtain a piezoelectric BST thin film, the c-axis (piezoelectric axis) of each grain in the thin film should be controlled so that it is oriented perpendicular to the substrate surface. The unit cell structure of a single crystal BST belongs to the point group of 4mm (see Figure 11) and therefore, has a tetragonal structure in which lengths of a- and b-axes are equal, but that of c-axis is shorter than the others, i.e., (a=b>c). As long as the c-axis of each grain in a BST thin film is aligned perpendicular to the substrate surface, the point group symmetry of the thin film becomes 6mm even if a- and b-axes are randomly distributed on the plane parallel to the substrate surface, a schematic demonstration of such a structure is given in Figure 55. As shown in Figure 56, a crystal which has the point group of either 4mm or 6mm has non-zero elements in the piezoelec- tric tensor, that is, the crystal is piezoelectric. Therefore,

the c-axis oriented BST thin film has a piezoelectricity.

4.9.4 BST Thin Films Fabricated by Sputtering Deposition

At temperatures below 240°C, c-axis oriented BST films were not able to form on amorphous substrates such as window glass and fused quartz. However, BST thin films fabricated on single crystal NaCl (200) cleavage surface at 170°C showed 001 peak of BST in the x-ray diffraction pattern. This may well be due to an epitaxial growth. The 001 diffraction peak was located at $2\theta = 15.8°$. Thus [001] or c-axis oriented BST thin film was epitaxially grown on the (200) plane of NaCl single crystal substrate. This mechanism may be explained as follows. The first nuclei, which already have the [001] orientation, grow into a three-dimensional island structure. These oriented and randomly distributed islands then grow along the [001] direction and increase their sizes by further deposition and come together. By repeating the coalescence of each island, it becomes a network structure. The network grows and gives rise to a continuous epitaxial film. According to the nucleation theory of thin film (49), epitaxy will occur for an orientation which gives a lower interfacial energy, a lower free energy of formation for the critical nucleus and a much higher nucleation rate than any other orientation.

There would be steps and ledges even on a cleaved NaCl surface. These defects might help such nuclei form on them.

This may well explain the experimental fact that single crystal substrate has a dominant influence on the oriented growth of the films at the same sputtering conditions.

4.9.5 Annealing of BST Thin Films

As mentioned earlier, c-axis oriented BST films were not able to form on glass and fused quartz substrates. However Halliyal et al.(50) reported that the bulk of amorphous BST glass could be piezoelectric when a temperature gradient was applied to the bulk to be crystallized with the c-axis aligned along the temperature gradient. Therefore, it may be worthwhile to study the crystallization process of amorphous BST films by means of a subsequent annealing.

4.9.5.1 Degree of Crystallinity

An x-ray diffraction method, i.e., the diffractometer method, was utilized for the investigation of amorphous-to-crystalline transition mechanism in the BST thin film. Although the absolute intensity of the diffracted x-rays must be measured in order to make a precise quantitative determination of the degree of crystallinity, it was not performed because necessary equipment was not available. Therefore, a method which was proposed by Evangelisti et al (51) was modified and utilized for the present case. This procedure was not entirely rigorous. However, Evangelisti et al showed that the degree of crystallinity calculated by their method (using the integrated intensities of

diffraction peaks) was in good agreement with those obtained from Raman scattering and EXAFS (Extended X-ray Absorption Fine Structure) measurements. Both Raman scattering and EXAFS methods are widely utilized for the investigation of non-crystalline materials. Degrees of crystallinity in a BST thin film annealed at temperatures between 700 and $950^\circ C$ were calculated using the modified method (cf. Section 4.8.4).

4.9.5.2 Average Size of Crystallites in BST Film

In general, crystallite grain size measurements can be performed by means of the scanning or the transmission electron microscopy. It is impossible to observe the grain size of the order of $50-300\text{Å}$ by SEM. In the present study, since it was not possible to peel BST thin films off from the substrate, it was not possible to use TEM either. Therefore, the Scherrer formula was employed to measure the crystallite size using the x-ray diffraction pattern. The value for the shape factor K (see Eq. (16)) is uncertain in the present case. It is, however, known that it lies in the range of 0.70-1.70 (48). Thus, quantity (d/k) in Figure 48 indicates an approximate grain size. Values for $(d/k)_{201}$ and $(d/k)_{002}$ were found to be almost identical. This indicates that c-axis or [001]-direction oriented crystal growth was not evident at this stage of the crystallization.

4.9.5.3 <u>Separation of Crystalline Peaks and</u>
<u>Amorphous Halo</u>

The separation of crystalline peaks and amorphous halo in the x-ray diffraction pattern (Section 4.8.4) was performed by means of computer calculations. The parameters finally employed may not correspond to the exact minimum of the square sum of errors. It should, however, be possible to find the real minimum in the 12-dimensional space and to obtain corresponding values for the 12 parameters, if an improved computer program is developed.

4.9.6 <u>BST Thin Films Deposited on Glass Substrate</u>
<u>Using Diode Magnetron Sputtering Method</u>

Specimen Q5 fabricated on glass substrate (see Table 7) was annealed in the temperature range from $490^{\circ}C$ to $700^{\circ}C$. Since the glass substrate started to warp at $700^{\circ}C$, annealing at higher temperatures was not performed. However, the crystallization of the sputtered BST thin films was found to begin between $490^{\circ}C$ and $600^{\circ}C$. Since, in this experiment, the BST powder was pressed to form a target for the diode magnetron sputtering-deposition system at Queen's University, there was a possibility to obtain sputter-deposited films consisting of larger sized clusters of BST molecules than in the sputtering deposition using a solid sintered ceramic target of BST. It should also be noted that the substrate temperature ($=370^{\circ}C$) in this case was higher than that ($=170^{\circ}C$) for other specimens, such as Specimen

W12q. These two factors may explain why the amorphous-to-crystalline transition temperature of Specimen Q5 was lower than that of Specimen W12q.

4.9.7 Energy Dispersive Analysis and Scanning Electron Microscopy

Energy dispersive analyses indicated that the chemical compositions of the BST thin films fabricated on both a glass (Figure 49 (a)) and single crystal NaCl (Figure 49 (b)) substrate were almost the same as that of the stoichiometric BST ceramic target. (Figure 18(a)) (Note that, in EDS pattern for the film on NaCl, strong Cl^- and Na^+ peaks must be subtracted in the comparison). For more precise quantitative chemical analysis of Ba and Ti, the x-ray fluorescence analysis method is recommended. Spectral interference of elements Ba, Si and Ti contained in the BST thin film with elements of the substrate can be avoided by selecting a proper substrate material.

Scanning electron micrographs showed smooth and continuous film surface of as-deposited BST films on glass substrates. The film deposited on single crystal NaCl (200) cleaved surface was also smooth. However such a film contained a number of cracks as shown in Figure 50 . This may be caused mainly by lattice parameter difference between BST (a=8.52Å) and NaCl (a=5.64Å) and by the difference in thermal expansion during the cooling process after sputtering deposition.

At an annealing temperature of 950°C, BST films fabricated on fused quartz substrates started to crack.

Since this film was perfectly crystallized homogeneously distributed cracks would be attributed to the densification of the film due to crystallization. The silica tetrahedra (SiO_2) were randomly distributed on the film, forming long chains of $(SiO_4)^{4-}$ before crystallization. During annealing, $(SiO_4)^{4-}$ chains were rearranged to form BST crystallites whose unit cell is shown in Figure 11(a).

BST thin films deposited on window glass substrate were also examined using SEM. At annealing temperatures below $500^{O}C$, films were smooth and continuous. However, above $500^{O}C$, wrinkles of the film were observed, as shown in Figure 53. Such wrinkles of the film have been observed by Sloope and Tiller (52) for Ge thin film on single crystal NaCl, CaF_2 and NaF substrates. These authors observed wrinkles at temperatures even below the amorphous-to-crystalline transition temperature. Such wrinkles disappeared after the crystallization completed. Sloope and Tiller also indicated that the wrinkles were related to the degree of crystallinity of the thin film. In the case of BST thin films, wrinkles observed at $550^{O}C$ and $700^{O}C$ seemed to be an indication of the tendency towards crystallization. Such wrinkles could also be caused by the difference in thermal expansion coefficients, α, of BST thin film ($\alpha_{BST} = 10.0 \times 10^{-6}$/k) (12) and of glass substrate ($\alpha_g = ~4.5 \times 10^{-6}$/k).

CHAPTER 5

SUMMARY

5.1 $Ba_2Si_2TiO_8$ Ceramic Disks

Fresnoite ($Ba_2Si_2TiO_8$) ceramic disks were successfully fabricated for the sputtering target. (The fabrication process developed is shown in Figure 12).

a) .The best sintering was obtained for the mixture of $BaCO_3$, SiO_2 and TiO_2 powder for the stoichiometric composition and a temperature of $1250^{\circ}C$ for 5 hours.

b) Composition analyses by means of the energy dispersive and the x-ray fluorescence analysers indicated that compositions of sintered $Ba_2Si_2TiO_8$ ceramic disks were almost identical with those of initial powder mixtures. Thus, in order to fabricate a stoichiometric $Ba_2Si_2TiO_8$ ceramic disk for the sputtering target, initially weighed powder mixture should have the stoichiometric composition.

c) When compositions of powder mixtures were off-stoichiometric by 5% in the composition of any one of $BaCO_3$, SiO_2 and TiO_2, co-existence of the second phase such as $BaTiO_3$ or SiO_2 with the $Ba_2Si_2TiO_8$ phase was experimentally confirmed.

5.2 $Ba_2Si_2TiO_8$ Thin Films

$Ba_2Si_2TiO_8$ thin films were fabricated by means of R.F. sputtering deposition on various substrate materials such as window glass, fused quartz and NaCl single crystal. Two different R.F. sputtering deposition systems were used:

1) R.F. diode-magnetron sputtering deposition system at the Physics Department of Queen's University and 2) R.F. magnetic-field supported triode sputtering deposition system installed at the Department of Engineering Materials of the University of Windsor.

a) At substrate temperatures below 240°C, thin films deposited on window glass and fused quartz substrates had amorphous structures.

b) A $Ba_2Si_2TiO_8$ thin film with the c-axis or [001]-direction oriented perpendicular to the substrate surface was obtained on an NaCl (200) cleaved surface when the substrate temperature was at 170°C and the sputtering R.F. power was 100W, using the magnetic-field supported triode sputtering deposition system for 10 hours.

c) The amorphous-to-crystalline transition temperature in the $Ba_2Si_2TiO_8$ thin film sputter-deposited on the fused quartz substrate was in the temperature range between 700°C and 800°C.

d) A novel method for evaluating the degree of crystallinity of an originally amorphous $Ba_2Si_2TiO_8$ thin film was developed .   The degree of crystallinity was 0% for specimens annealed at temperatures below 700°C. Degrees of crystallinity were 67, 81 and 100% for specimens annealed at temperatures at 800, 900 and 950°C, respectively.

e) The average sizes of crystalline particles in partially crystallized specimens annealed at 800°C and 950°C

were found to be ~ 180 and ~250 $\overset{\circ}{A}$, respectively, using the Scherrer formula (the shape factor, k, was assumed to be unity).

f) Comparing the energy dispersion spectra (Figures 51 and 18(a)), compositions of both amorphous $Ba_2Si_2TiO_8$ thin film (deposited on window glass) and c-axis oriented poly-crystalline $Ba_2Si_2TiO_8$ thin film (deposited on NaCl single crystal) were concluded to be quite close to the stoichio-metric composition.

g) Thus, a $Ba_2Si_2TiO_8$ crystalline thin film with the c-axis perpendicular to the substrate surface was successfully fabricated on the (200) plane of single crystal NaCl.

CHAPTER 6

FUTURE RESEARCH

Further research is required on $Ba_2Si_2TiO_8$ thin film fabrication. This research should be concentrated on such processes as: the amorphous-to-crystalline transition mechanism and the c-axis control of thin film. Also electronic properties which are characteristic of the BST thin film such as dielectric constant, piezoelectric resonance and surface-acoustic-wave characteristics should be examined. This research should include the following:

1) Annealing temperatures should be selected between 700 and $800^\circ C$ as many as possible in order to study amorphous-to-crystalline transition mechanism;

2) The scanning rate of the x-ray diffractometer should be slowed. This enables more precise x-ray data analysis. Lattice constants should be calculated at each annealing stage in order to take into account the strain energy for the transition mechanism;

3) In order to deposit a c-axis oriented BST thin film, the substrate temperature may be increased up to about $650^\circ C$.

4) For the fabrication of a thick (~10 μm) BST film, a long sputtering operation is required, during which the filament must be stable (See Figure 31). In order to prolong the lifetime of the filament, it is essential that positively charged ions do not sputter it. This may be realized by reducing the applied voltage

between the filament and anode (See Figure 31). At the
same time, the filament current must be increased to pro-
duce more electrons so that the plasma generating efficiency
is not reduced. It is known that the sputtering rate is
much larger for a metallic target than for a ceramic (which
is an insulator) one. It may be possible to sputter BST
films by a reactive deposition of a metallic target. It
would consist of Ba, Si and Ti metals or alloys and then
oxygen gas would be introduced into the chamber;

5) For average grain size measurements, transmission
electron microscopy (TEM) is recommended. In order to pre-
pare samples for TEM, a continuous film should be deposi-
ted on a single crystal NaCl. The NaCl substrate can then
be dissolved by water.

6) The effect of altering the sputtering conditions
on the thin film characteristics should be studied. This
should include the effect of changing the distance between
the target and substrate, oblique sputtering and the effect
of changing the substrate temperature and deposition rate.

REFERENCES

1. N.F. Foster, IEEE, Trans. Sonics and Ultrason., SU-11, 63-68 (1964).

2. N.F. Foster and G.A. Rozgonyi, J. Appl. Phys. Lett., 8, 221-223 (1966).

3. M.T. Wauk and D.K. Winslow, J. Appl. Phys. Lett., 13, 286-288 (1968).

4. T. Shiosaki, T. Yamamoto, T. Oda and A. Kawabata, J. Appl. Phys. Lett., 36, 643-645 (1980).

5. N.F. Foster, J. Appl. Phys., 40, 420-421 (1969).

6. M. Adachi, K. Kumagawa, T. Shiosaki and A. Kawabata, Japanese J. Appl. Phys., Suppl. 20-4, 17-22 (1981).

7. J.T. Alfors, M.C. Stinton and R.A. Matthews, Am. Mineral, 50, 314-340 (1965).

8. P.B. Moore and J. Louisnathan, Science, 156, 1361-1362 (1967).

9. R. Masse, J.C. Grenier and A. Durif, Bull. Soc. Fr. Mineral Crystallogr. XC, 20-23 (1967).

10. M. Kimura, Y. Fujino and T. Kawamura, J. Appl. Phys. Lett., 29, 227-228 (1976).

11. J. Eckstein, K. Recker and F. Wallrafem, Naturwissen-schaften, 63, 435 (1976).

12. M. Kimura, J. Appl. Phys., 48, 2850-2856 (1977).

13. S. Haussuhl, J. Eckstein, K. Recker and F. Wallrafen, J. Cryst. Growth, 40, 200 (1977).

14. H. Yamauchi, J. Appl. Phys., 49, 6162-6164 (1978).

15. H. Yamauchi, K. Yamashita and H. Takeuchi, J. Appl. Phys., 50, 3160-3167 (1979).

16. J.F. Nye, "Physical Properties of Crystals," 8th Ed., Oxford University Press, Oxford, p. 118 (1979).

17. M. Kimura, K. Doi, S. Nanamatsu and T. Kawamura, J. Appl. Phys. Lett., 23, 531- (1973).

18. S. Roberts, Phys. Rev., 71, 890 (1947).

19. B. Jaffe, R.S. Roth and S. Marzullo, J. Appl. Phys., 25, 809-810 (1954).

20. A.J. Slobodnik, Jr., IEEE Proc., 64, 581-595 (1976).

21. R.M. White and F.W. Voltmer, J. Appl. Phys. Lett., 7 314-316 (1965).

22. J.J. Campbell and W.R. Jones, IEEE Trans. Sonics and Ultrason., SU-15, 209-217 (1968).

23. H.F. Tierstein, J. Acoust. Soc. Amer., 35, 53-58 (1968).

24. K.A. Ingebrigtsen, J. Appl. Phys., 40, 2681-2686 (1969).

25. M.B. Schulz and J.H. Matsinger, J. Appl. Phys. Lett., 20 367-369 (1972).

26. J.H. Collins, H.M. Gerard and H.J. Shaw, J. Appl. Phys. Lett., 13, 312-313 (1968).

27. P.H. Carr, IEEE Ultrasonic Symposium Proceedings, New York, p. 286 (1974).

28. K. Shibayama, Ferroelectrics (G.B.), 42, 153-159 (1982).

29. M.B. Schulz and H.G. Holland, IEEE Proc., 58, 1361-1362 (1970).

30. Y. Shimizu and Y. Yamamoto, 1980 Ultrasonics Symposium Proc. IEEE, 420 (1980).

31. K. Shibayama, K. Yamanouchi, H. Sato and T. Meguro, IEEE Proc., 64, 595-597 (1976).

32. K. Yamanouchi and K. Shibayama, J. Appl. Phys., 43, 856-862 (1972).

33. S. Takahashi, H. Hirano, T. Kodama, F. Miyashiro, B. Suzuki, A. Onoe, T. Adachi and K. Fujinuma, IEEE Trans., on Consumer Electronics, Ce-24, 337 (1978).

34. H. Takeuchi, Private Communication (1980).

35. T. Tanaka, S. Okasaki and N. Ichinose, "Piezoelectric Ceramic Materials, ('Atsuden Ceramics Zairyo' in Japanese)," Gakkensya Inc., Tokyo, 90-132 (1973).

36. Y. Ito, H. Takeuchi, S. Jyomura, K. Nagatsuma and S. Ashida, J. Appl. Phys. Lett., $\underline{35}$,595-   (1979).

37. P.D. Davide and L.I. Maison, J. Appl. Phys., $\underline{37}$, 574 (1966).

38. F.J. Hickernell, IEEE Proc., $\underline{64}$, 631-635 (1976).

39. B.T. Khuri-Yakub, G.S. Kino and P. Galle, J. Appl. Phys., $\underline{46}$, 3266-3272 (1975).

40. T. Yamamoto, T. Shiosaki and A. Kawabata, J. Appl. Phys., $\underline{51}$, 3113-3120 (1980).

41. S. Maniv, W.D. Westwood and E. Colombini, J. Vac. Sci. Technol., $\underline{20}$, 162-170 (1982).

42. A.J. Shuskus, T.M. Reeder and E.L. Paradis, J. Appl. Phys. Lett., $\underline{24}$, 155-159 (1979).

43. A. Okada, J. Appl. Phys., $\underline{48}$, 2905-2909 (1977).

44. A. Okada, J. Appl. Phys., $\underline{49}$ 4495-4499 (1978).

45. M. Ishida, H. Matsunami and T. Tanaka, J. Appl. Phys., $\underline{48}$, 951-953 (1977).

46. L.D. Calvert and J. Trotter, "Fresnoite," Structure Reports, $\underline{32A}$, 442-443 (1967).

47. R. White, 4th year project, Dept. of Engineering Materials, University of Windsor, Windsor (1983).

48. H.P. Klug, "X-ray Diffraction Procedure," 2nd Ed., John Wiley & Sons, Inc., New York, 511 (1959).

49. K.L. Chopra, "Thin Film Pheonmena," McGraw-Hill, Inc., New York, 224-253 (1969).

50. A. Halliyal, A.S. Bhalla, R.E. Newnham, L.E. Cross, T.R. Gururaja, J. Mats. Sci., $\underline{17}$, 295-300 (1982).

51. F. Evangelisti, M. Garozzo and G. Conte, J. Appl. Phys., $\underline{53}$, 7390-7396 (1982).

52. B.W. Sloope and C.O. Tiller, J. Appl. Phys., $\underline{33}$, 3458-3463 (1962).

53. B.D. Cullity, "Elements of X-ray Diffraction," 2nd Ed.
    Addison-Wesly Publishing Company, Inc., p. 512-513 (1978).

54. J.F. Nye, "Physical Properties of Crystals," 8th Ed.,
    Oxford University Press, Oxford, p. 295-301 (1979).

TABLES AND FIGURES

72

Table A.1

Sputtering Deposition Conditions for Piezoelectric-Axis Controlled Thin Films

Film	Sputtering Deposition Method	Substrate Material	Substrate Temperature (°C)	Deposition Rate (µm/h)	Reference
ZnO	R.F. Diode	Fused Quartz	350		
		Sapphire	350	0.60-0.78	(39)
		Gold	200-275		
	R.F. Planarmagnetron	Glass	320-370	0.3 -1.5	(40)
	R.F. Planarmagnetron (Reactive)	Glass	---	7.2	(41)
AlN	R.F. Reactive	Sapphire	1200	0.5	(42)
	R.F. Planarmagnetron	Sapphire	160	0.2 -0.8	(4)
		Glass	200		
PZT	R.F. Diode	Platinum	500	0.30-0.42	(43)
		Fused Quartz	500	0.30-0.42	(43)
PLZT	R.F. Diode	Platinum	480		
		Fused Quartz	550	0.36	(45)
$K_3LiNb_5O_{15}$	R.F. Diode	Sapphire	520	0.08-0.10	(6)
		$K_2B\ Nb_5O_{15}$	500-600	0.08-0.10	(6)

Table 1

Position of Composition Atoms in Fresnoite Unit Cell
Ref. (46)

Atom	Position		
	x	y	z
Ba	0.173	0.673	0.000
Ti	0.000	0.000	0.540
Si	0.630	0.130	0.520
O(1)	0.090	0.206	0.655
O(2)	0.618	0.118	0.210
O(3)	0.500	0.000	0.620
O(4)	0.000	0.000	0.160

Table 2

Physical and Chemical Properties of Fresnoite

		References
Chemical Formula	$Ba_2TiSi_2O_8$	(7)
Crystal Structure	Tetragonal	(7)
Space Group	P4/mbm, P4bm, or $P\bar{4}b2$	(7)
Lattice Constants: a c a/c	 0.852 ± 0.001 nm 0.5210 ± 0.0005 nm 0.6115	 (7) (7) (7)
Density	4.43×10^{-3} kg/m^3	(7)
Melting Point	$\sim 1400^{\circ}C$ $1445\pm5^{\circ}C$	(7) (11)
Solvents	hot 1:1 HCl Cold glacial acetic acid	(7) (7)
Linear Thermal Expansion Coefficients α_a α_c	 9.8×10^{-6}/k 10.3×10^{-6}/k	 (12) (12)

Table 3(a)

Molecular Weights of Fresnoite and Raw Materials

Material	Molecular Weight
$Ba_2Si_2TiO_8$	506.79
$BaCO_3$	197.35
SiO_2	60.08
TiO_2	79.90

Table 3(b)

Raw Materials in Weight for Obtaining 100g Stoichiometric Fresnoite Compound

Raw Material	Weight (g)
$BaCO_3$	66.35
SiO_2	20.20
TiO_2	13.45

Table 4

Composition of Fresnoite Target Disks

Specimen Number	Weight Percentage				Sintering Temperature (^{o}C)
	$BaCO_3$	SiO_2	TiO_2		
T1	66.35	20.20	13.45	stoichiometric	1250
T2	66.35	20.20	13.45	stoichiometric	1280
T3	63.19	24.00	12.81	stoichiometric + 5wt%SiO_2	1250
T4	63.19	19.24	17.57	stoichiometric + 5wt%TiO_2	1250
T5	67.95	19.24	12.81	stoichiometric + 5wt%$BaCO_3$	1250

Table 5

Energy Dispersive Spectrometry Analysis of Fresnoite Target Ceramics

Specimen Number	Count Number		Count No. (Si) / Count No. (Ba+Ti)
	Si*	Ba+Ti**	
T1	697	1085	0.642
	960	1475	0.650
T2	614	1308	0.469
	712	1324	0.538
T3	1018	1364	0.746
	965	1385	0.697
T4	837	1383	0.605
	960	1475	0.650
T5	843	1421	0.593
	892	1481	0.601

* Energy Range: 1.60~1.80KeV for $Si(K_\alpha)$ and $Si(K_\beta)$

** $Ba(L_\alpha)$, $Ba(L_\beta)$, $Ti(K_\alpha)$ and $Ti(K_\beta)$ are located in Energy Range 4.2~5.2KeV.

Operating Conditions: accelerating voltage 1.5kV
                      counting time -   60 sec.

Table 6

X-Ray Fluorescence Analyses of Fresnoite Target Ceramics

Specimen Number	Initial Weight Percentage			X-Ray Fluorescence Analyses Count No.			X-Ray Fluorescence Analyses Weight Percentage		
	BaO	SiO$_2$	TiO$_2$	BaO	SiO$_2$	TiO$_2$	BaO	SiO$_2$	TiO$_2$
A	60.85	23.49	15.66	7424541	402363	4977190	60.52	23.71	15.77
B	59.94	25.22	14.84	7555434	384681	5185953	61.17	22.51	16.32
T1	60.57	23.65	15.77	7056951	331258	4646572	62.69	21.27	16.04
Theoretical Stoichiometric Weight %	60.52	23.71	15.77						

Operating Conditions: 50kV, 40 mA; Cr tube

Analized Peaks:

Material	X-ray Line	2θ(°)	Counting Time (sec.)
SiO$_2$	Si K$_\alpha$	32.12	100
TiO$_2$	Ti K$_\alpha$	86.26	40
BaO	Ba L$_\alpha$	87.29	40

Table 7(a)

Operating Conditions of Diode Magnetron Sputtering System at Queen's University

Sputtering Gas	100% Oxygen
Sputtering Pressure	12~30 mTorr
Target - Substrate Distance	100 mm
Target - Diameter	100 mm
Substrate Temperature	R.T.~370°C
R.F. Power	220~260 W
Substrate Materials	Normal Glass Conducting Glass (In_2O_3 Coated)
Sputtering Time	75~240 min.

Table 7(b)

Sputtering Deposition Using Diode Magnetron Sputtering System at Queen's University

Specimen Number	R.F. Power (W)	Substrate Temperature ($^{\circ}$C)	Sputtering Time (min.)	Gas Pressure (mTorr)
Q1	260	R.T.	75	12
Q2	260	R.T.	80	20
Q3	240	220 $\pm$20	180	12
Q4	300	300 $\pm$20	240	16
Q5	220	370 $\pm$20	240	30

Table 8

Operating Conditions of New Triode R.F.-Sputtering Deposition System

R.F. Power	50~190 W
Plasma Current	1.5~2.0 A
Plasma Voltage	45~55 V
Electron Emitter Current	18~36 A
Sputtering Gas	Argon gas + Oxygen gas
Sputtering Gas Pressure	1.5~50 mTorr
Target - Substrate Distance	70.0 mm
Target Diameter	23.8 mm
Target Thickness	1.5 mm
Substrate Temperature	Room temperature ~240°C
Substrate Materials	Window glass, Fused Quartz, NaCl (Rock Salt)
Sputtering Rate	2.5~52.9 Å/min.

Table 9

Thin Film Deposition Using New Triode R.F.-Sputtering Deposition System

Specimen Number	R.F. Power (w)	Substrate Temperature (°C)	Sputtering Time (min.)	Gas Pressure (m Torr)	Film Thickness (Å)
W1g	50	R.T.*	60	10	1000 ± 90
W2g,q,s+	50	R.T.	240	1.5	1500 ± 200
W3g,q,s	50	R.T.	260	1.5	1000 ± 100
W4g,q,s	50	R.T.	300	1.5 -10	760 ± 70
W5g,q,s	50	130	300	1.5	1700 ± 150
W6g,q,s	50	R.T.	600	50	1800 ± 300
W7g	75	R.T.	60	1.5-10	800 ± 80
W8g	75	R.T.	240	1.5	1700 ± 200
W9q,q,s	75	R.T.	300	1.5	2700 ± 150
W10g,q,s	75	240	540	35	----
W11g,q,s	100	230	140	1.5	----
W12g,q,s	100	170	600	1.5	3900 ± 350
W13g,q,s	100	200	100	1.5	----
W14q,q,s	120	R.T.	180	50	2000 ± 400
W15q	190	R.T.	70	1.5	3700 ± 400

* R.T.: Room Temperature
+ g: Sputtered on window glass substrate;
  q: Sputtered on fused quartz substrate;
  s: Sputtered on NaCl (100) cleavage surface.

Table 10

Annealing Temperature for Amorphous BST
Thin Film Specimen

Specimen Number	Annealing Temperature * (^{O}C)
W12A	As-deposited
W12B	300
W12C	400
W12D	500
W12E	600
W12F	700
W12G	800
W12H	900
W12I	950

Sputtering Conditions:

R.F. power   – 100W
Sputtering time – 600 min.
Gas pressure   – 1.5 mTorr
Substrate temp. – 170°C
Film thickness   – 3900 Å
Annealing Time – 10 hrs.
* Error: $\pm 5^{O}$C

Table 11

Integrated X-Ray Diffraction Peaks From Thin
Film Specimens

Specimen Number	Annealing Temperature ($^{\circ}$C)	I_A *	I_C *
W12D	500	203.8	0.0
W12G	800	79.9	191.0
W12H	900	46.3	228.1
W12I	950	0.0	262.0

I_A: Amorphous Peak $\left.\begin{array}{c} \\ \\ \end{array}\right\}$(Arbitrary Units)

I_C: Crystalline Peaks

* Error: $\pm$ 10.0

Table 12

Scattering Efficiency of Amorphous Region in Thin Film Specimen

Scattering Efficiency	Compared Specimens		Annealing Temperature (°C)		p*
	1	2	T_1	T_2	
p1	W12D	W12G	500	800	1.285
p2	W12D	W12H	500	900	0.890
p3	W12D	W12I	500	950	0.731
p4	W12G	W12H	800	900	1.448
p5	W12G	W12I	800	950	1.105
p6	W12H	W12I	900	950	1.541
$p_{Average}$	----	----	---	---	1.17 ±0.45

$$*: \quad p(\text{Scattering efficiency}) = \frac{I_C^i(T_2) - I_C^i(T_1)}{I_A^i(T_1) - I_A^i(T_2)}$$

where, I_A^i = Amorphous Peak Intensity;
I_C^i = Crystalline Peak Intensity. $\Big\}$ (Arbitrary Units)

Subscript (T_1) or (T_2) refers to the Annealing Temp.

Table 13

Degree of Crystallinity in Annealed Thin Films

Specimen Number	Annealing Temperature (^{O}C)	(D.C.)*(%)
W12A—F	700	0.0 †
W12G	800	67.1 †
W12H	900	80.8 †
W12I	950	100.0 †

(D.C.)*:

D.C. (Degree of Crystallinity) $= \dfrac{K_C}{K_C + P \cdot K_A}$

where,

$K_C = \sum\limits_{i} \int\limits_{-\infty}^{\infty} I_C d(2\theta)$: Total integrated intensity for crystalline peaks

$K_A = \int\limits_{-\infty}^{\infty} I_A d(2\theta)$: Integrated intensity for amorphous peaks

P = 1.17: Scattering Efficiency (Refer to Table 12).

† Error: ± 15.0%

Table 14

Average Size of Crystalline Determined by Use of the Scherrer Formula

Specimen Number	Annealing Temperature (^{O}C)	Grain Size ($\overset{O}{A}$)*	
		$(d/k)_{002}$	$(d/k)_{201}$
W12A~F	700	---	---
W12G	800	185	180
W12H	900	220	230
W12I	950	230	250

* d: Grain Size;
  k: Shape Factor;
  Subscript: Peak Index.

  Error: $\pm$ 10 $\overset{O}{A}$

Electromagnetic
Input

Delayed
Electromagnetic
Output

Piezoelectric Material

Surface Acoustic Wave

Interdigital
Transducer
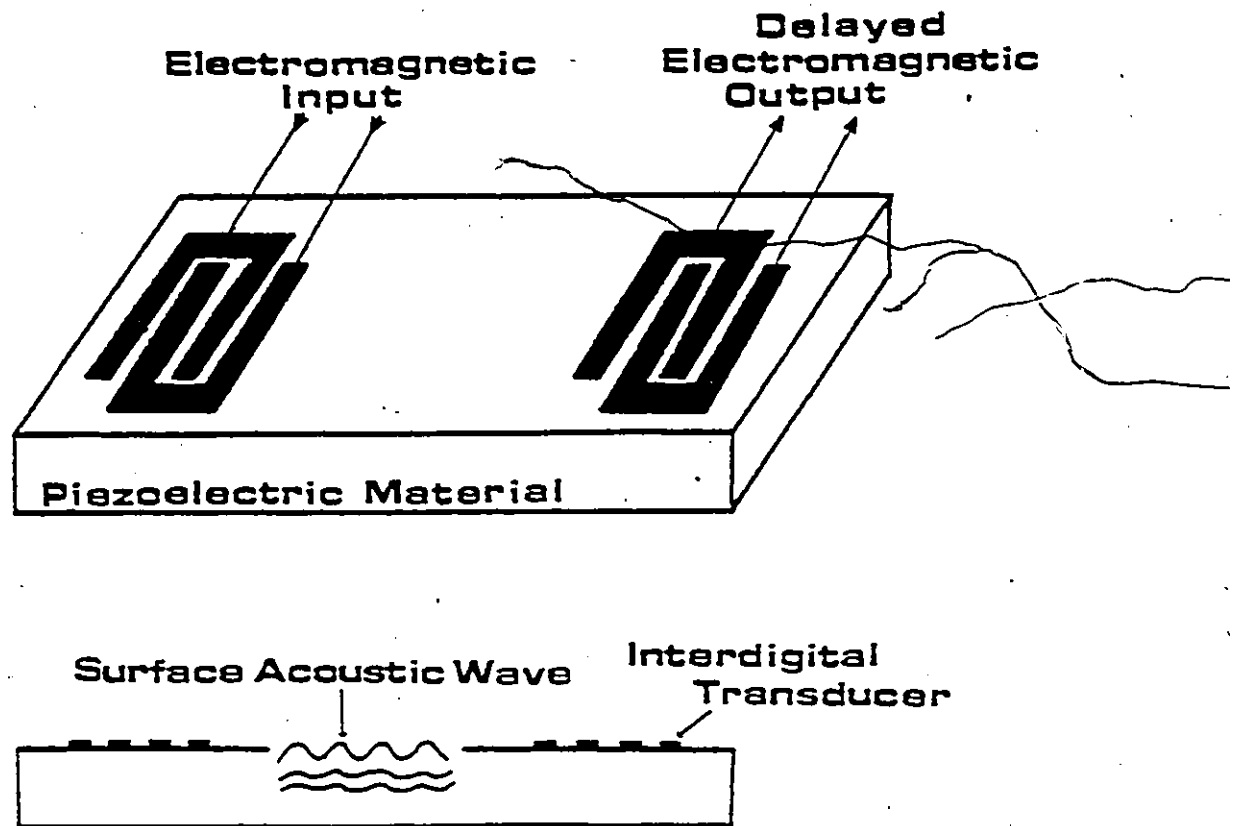
Figure 1   Schematic representation of the launching, propagation
and detection of a surface acoustic wave (SAW).

Free Surface

Infinitesimally Thin Perfect Conductor

X_2

h

X_1

X_3

Piezoelectric Crystalline
Substrate
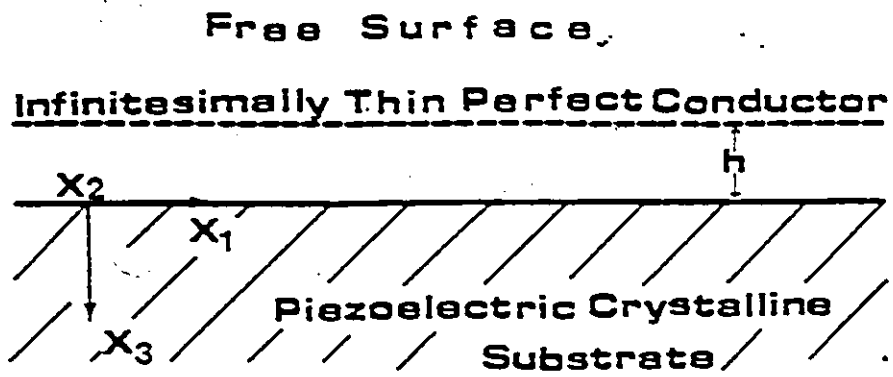
Figure 2 · Illustration of the coordinate system used to define
SAW propagation. The shorting plane is·necessary when
calculating the value of $\Delta v/v$.
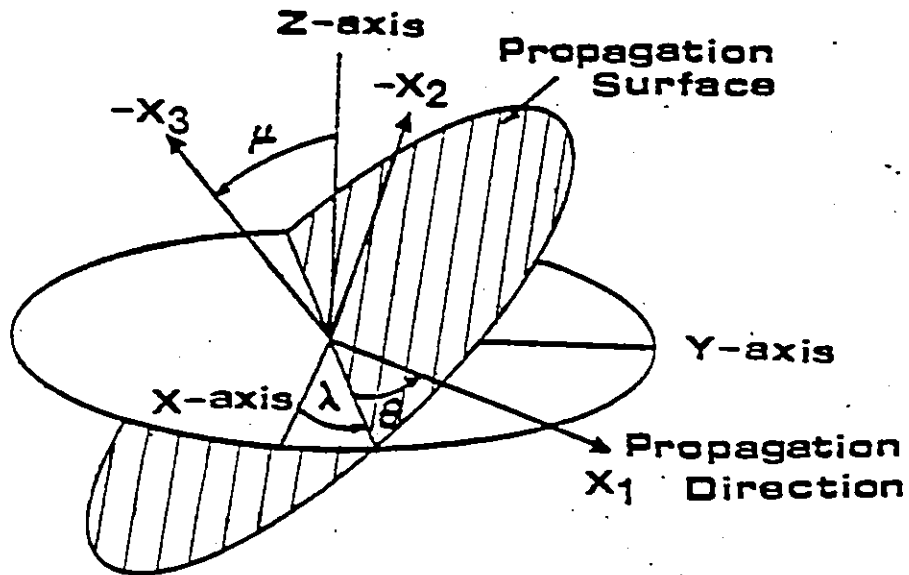
Figure 3   Eulerian angles (λ,μ,θ) between crystal-axis coordinates (x_1,x_2,x_3), in which the x_1 axis is along the SAW propagation direction, and the x_3 axis is inward normal to surface of the material.
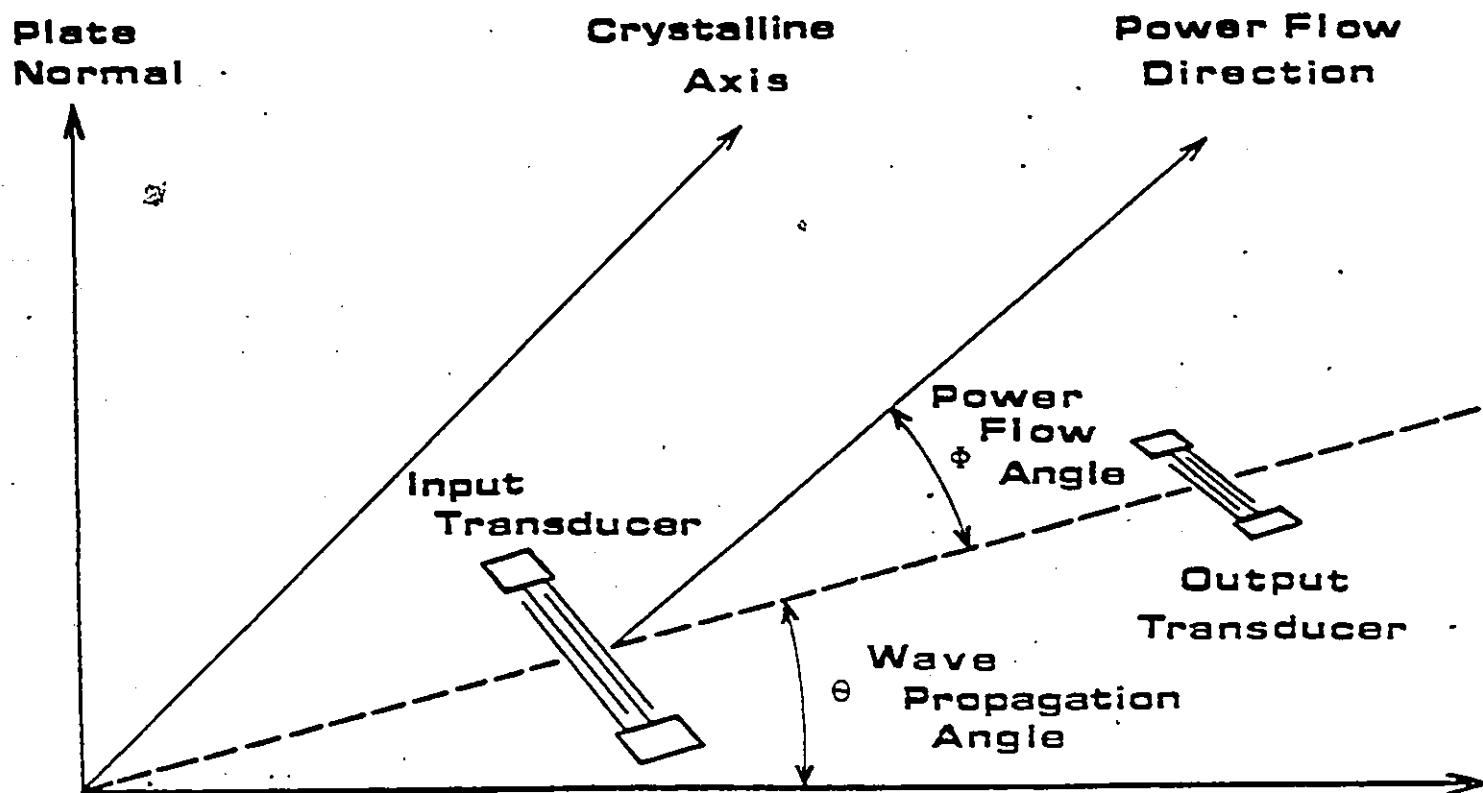
Figure 4 - Schematic representation of the direction of a propagating SAW on a crystalline substrate. Angle, θ, defines direction of propagation with respect to reference crystalline axis, and angle ,Φ, defines deviation of power flow from phase velocity direction.
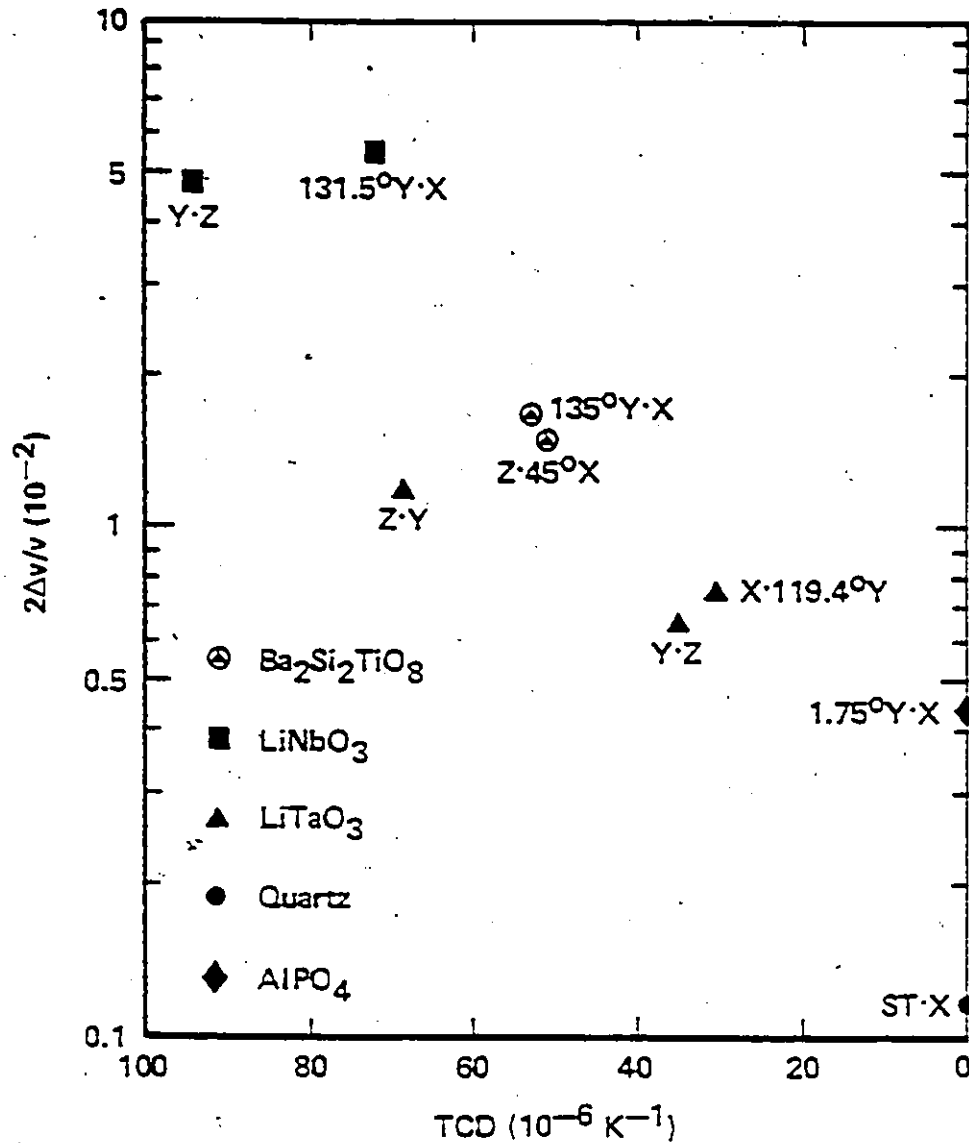
Figure 5   Electromechanical coupling 2Δv/v vs temperature co-
efficient of delay TCD for sets of SAW propagation
plane and direction in piezoelectric single crystals.
Ref.(14).
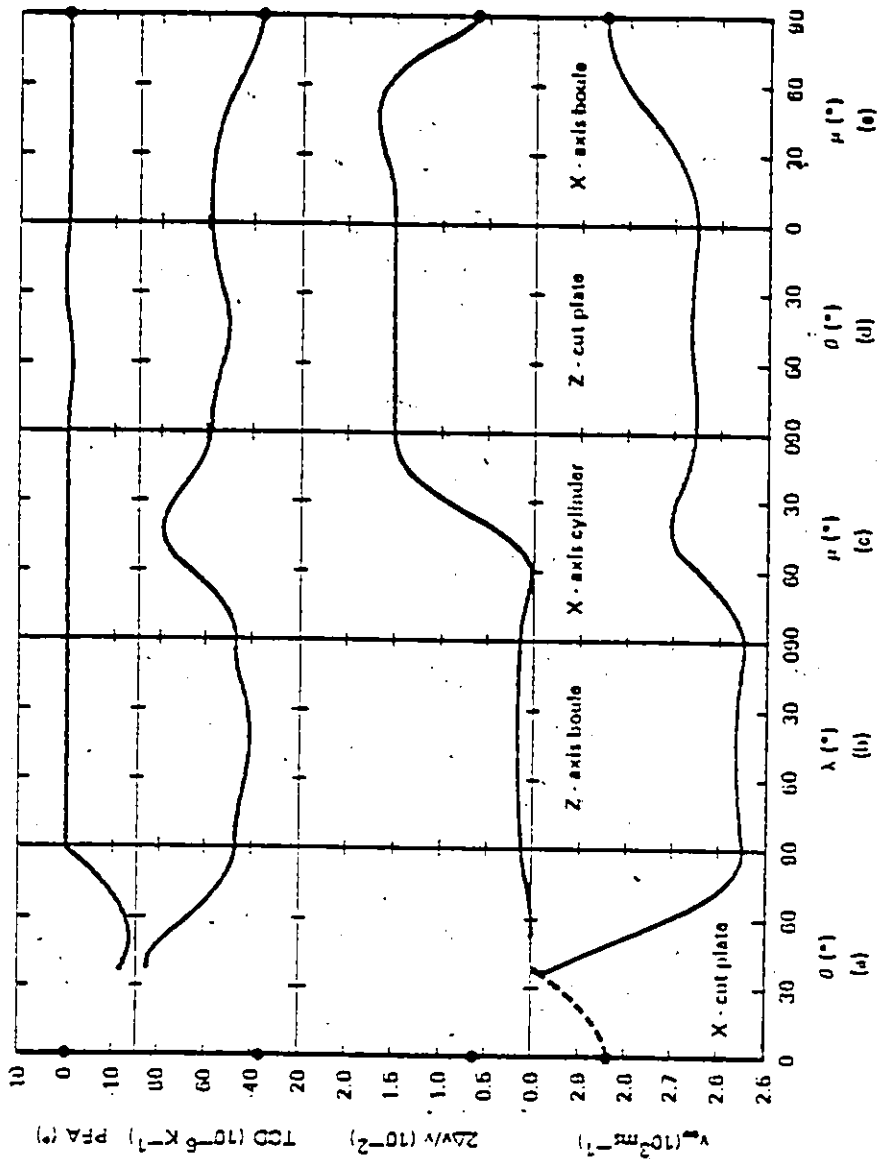
Figure 6   SAW characteristics of $Ba_2Si_2TiO_8$:velocity v_∞, electromechanical coupling $2\Delta v/v$, temperature coefficient of delay TCD,and power flow angle PFA. For Eulerian angles (λ, μ, θ), (a) $(90°,90°,\theta)$;(b) $(\lambda,90°,90°)$;(c) $(0,\mu,90°)$;(d) $(0°,0°,\theta,)$;and(e) $(0°,\mu,0°)$. Ref.(15).
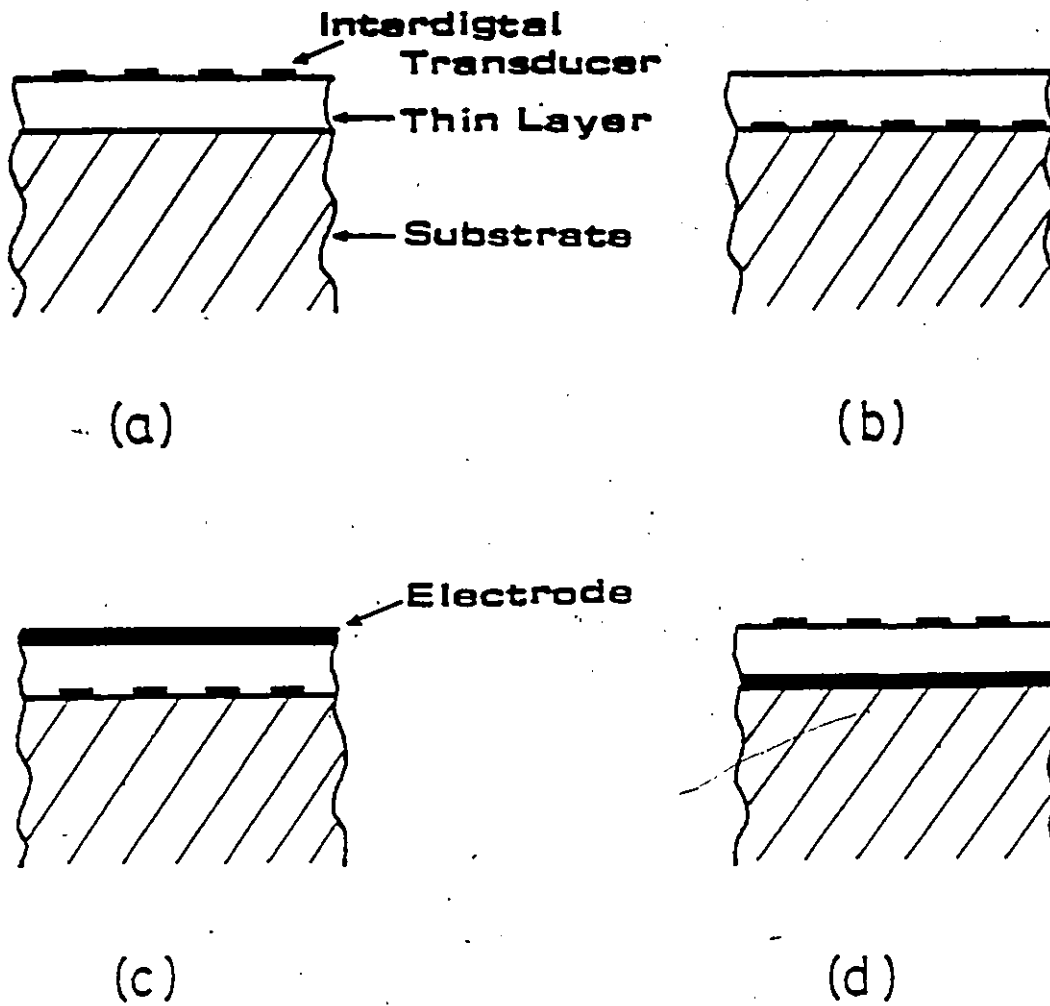
Figure 7   Arrangements of the interdigital transducer and the short electrode for layered structure.
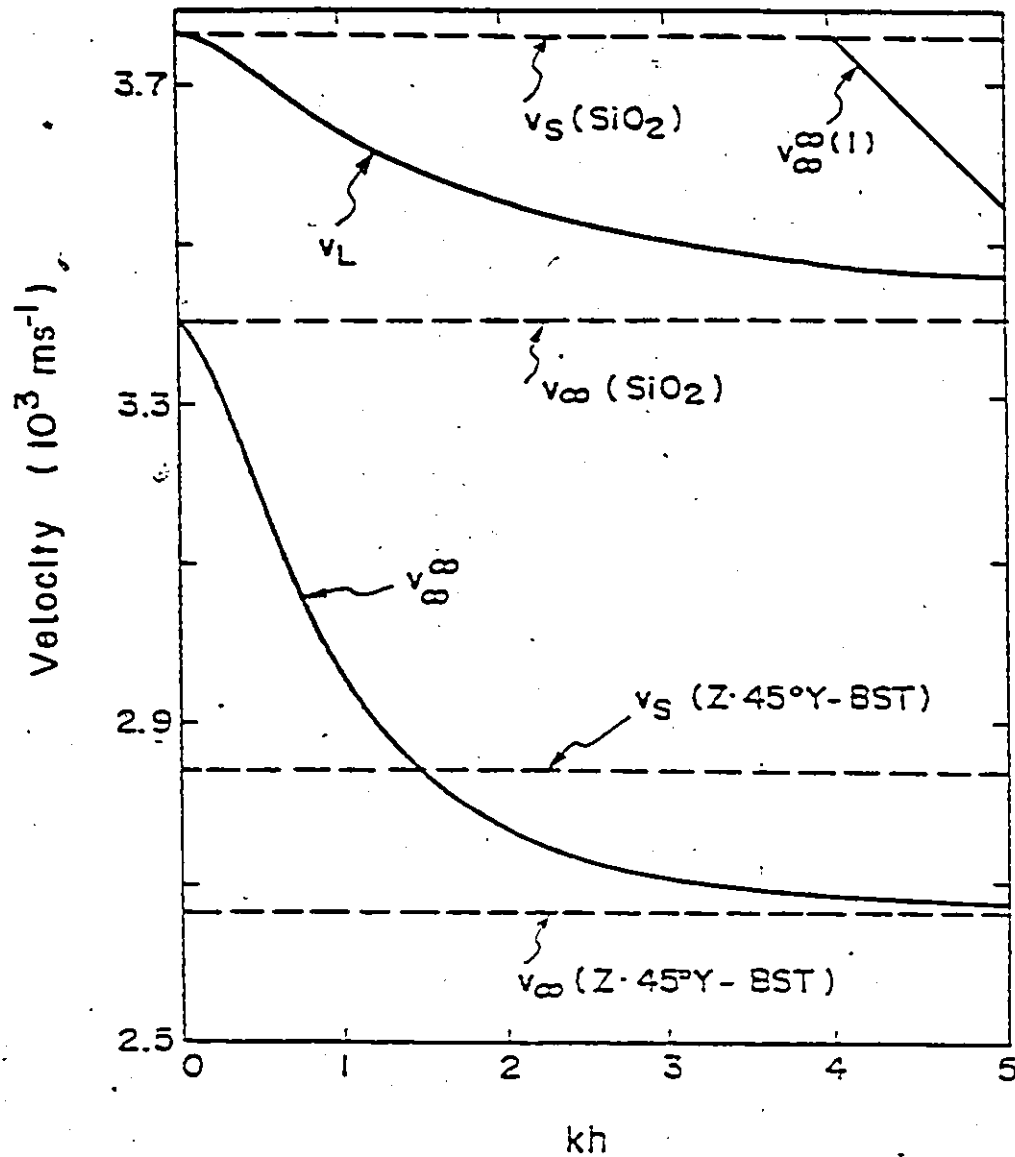
Figure 3   Phase velocities of SAW's on $(Z-45°Y-Ba_2Si_2TiO_8)/$(fused quartz). v_∞^∞ is for the fundamental modified Rayleigh wave, and $v_\infty^{(1)}$ is for the first-order harmonic of the modified Rayleigh wave when the surface and interface are electriclly open. v_L is for Love wave. The abcissa kh represents the wave number k normalized by the inverse of the layer thickness h. v_S is the bulk shear-wave velocities, and v_L is the velocity of stiffened Rayleigh wave. Ref. (15).
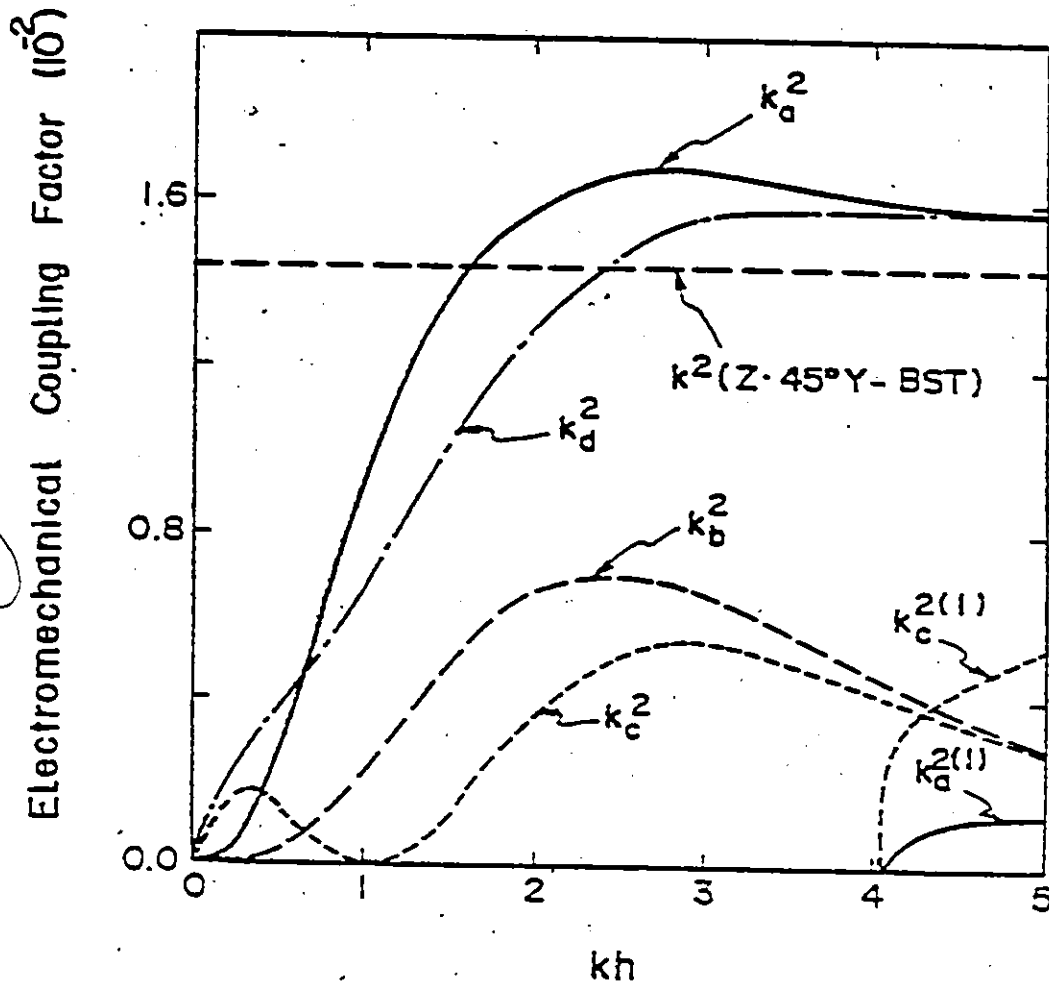
Figure 9　Electromechanical coupling factors k_a^2, k_b^2, k_c^2 and k_d^2 for the fundamental modified Rayleigh wave, and $k_a^{2(1)}$ and $k_c^{2(1)}$ for the first-order harmonics of the modified Rayleigh wave on $(Z45°Y-Ba_2Si_2TiO_8)/($fused quartz$)$. The abcissa kh represents the wave number k normalized by the inverse of the layer thickness h. Subscripts a-d represent the four cases of the electrode arrangements shown in Fig.7. Ref.(15).
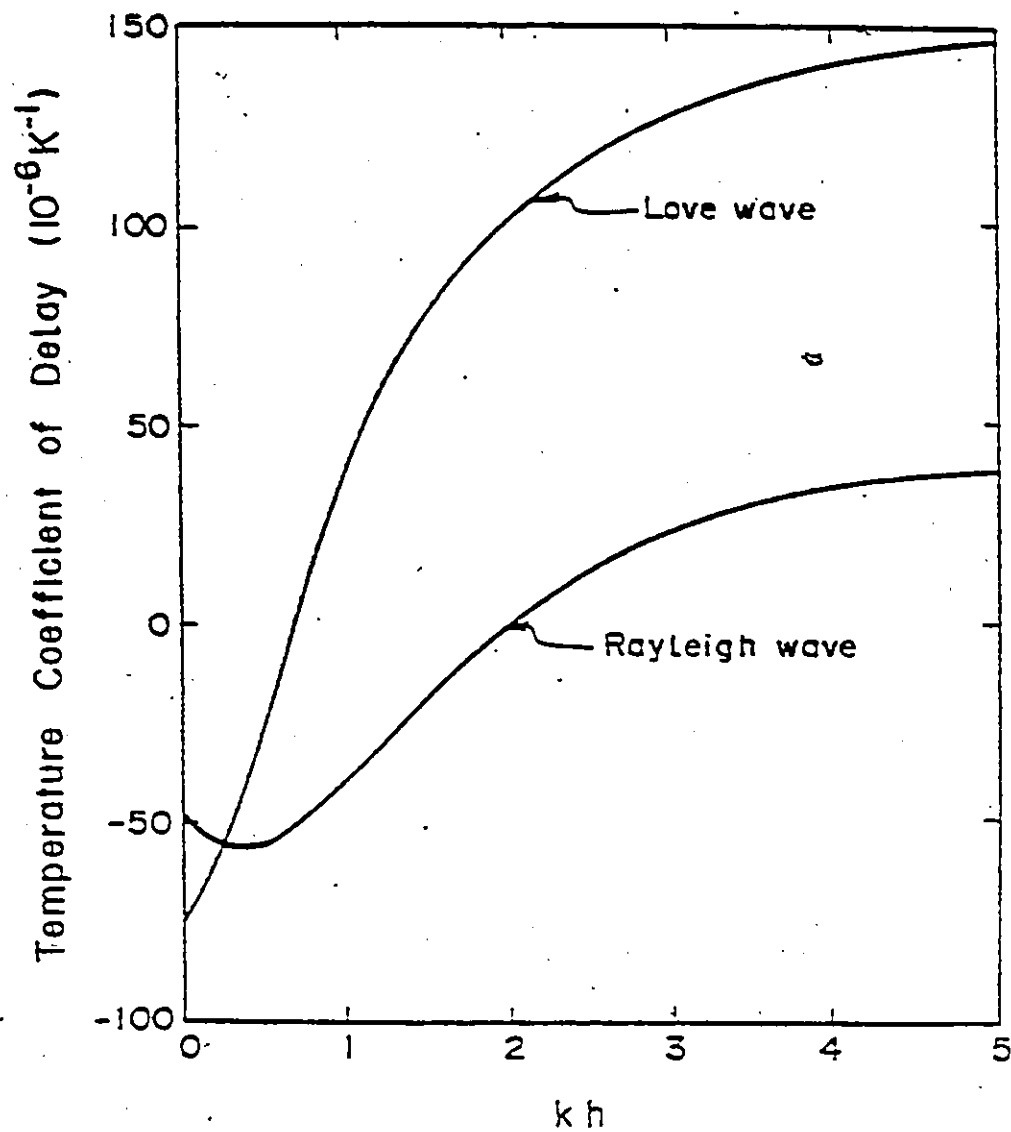
Figure 10   Temperature coefficients of delay for the fundamental
modified Rayleigh wave and for the Love wave on
$(Z-45°\ Y-Ba_2Si_2TiO_8)/$(fused quartz). The abcissa kh
is the wave number k normalized by the inverse of the
layer of thickness h. Ref.(15).

Si   Ti   Ba   O
4+   4+   2−   2−
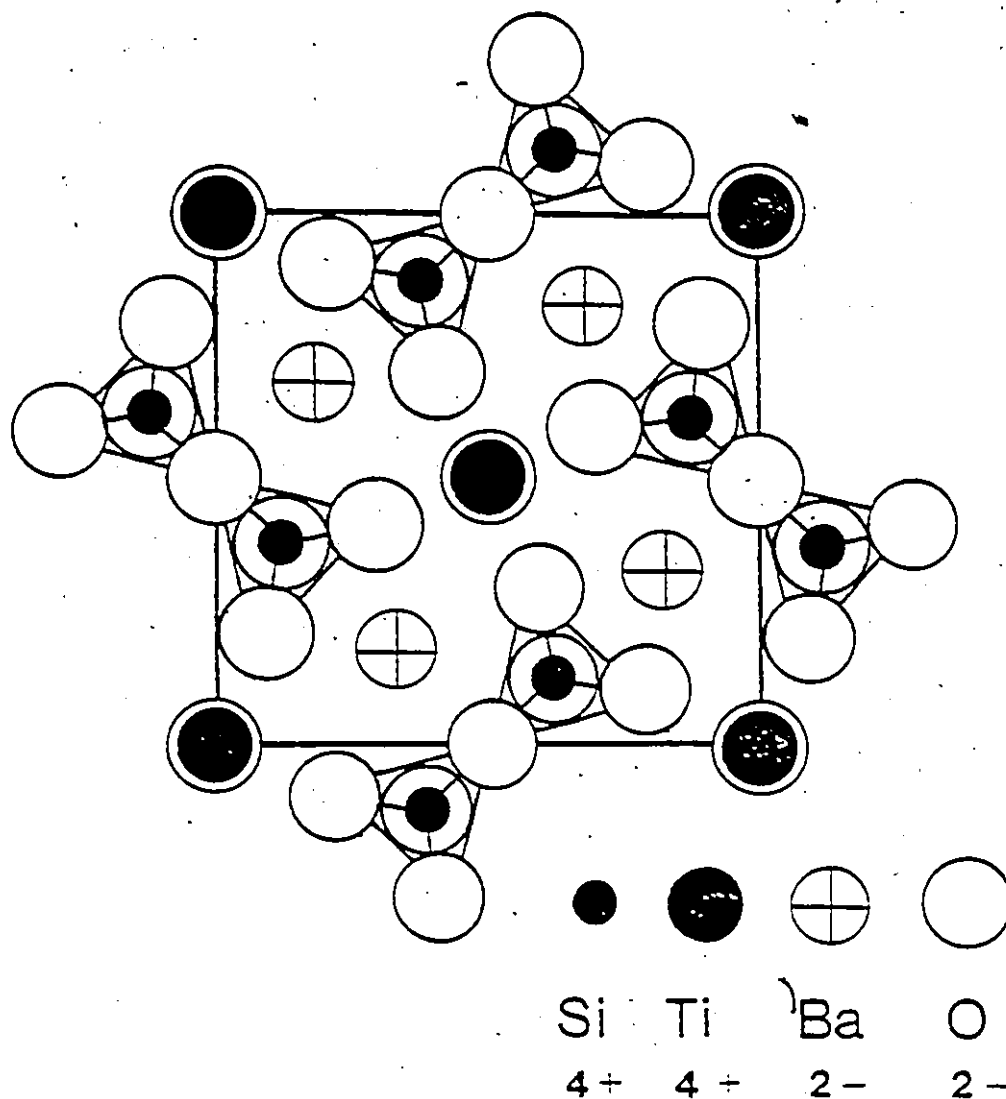
(a)

Figure 11 (a) Projection of $Ba_2Si_2TiO_8$ structure on (001) or X-Y plane. Ref.(9).
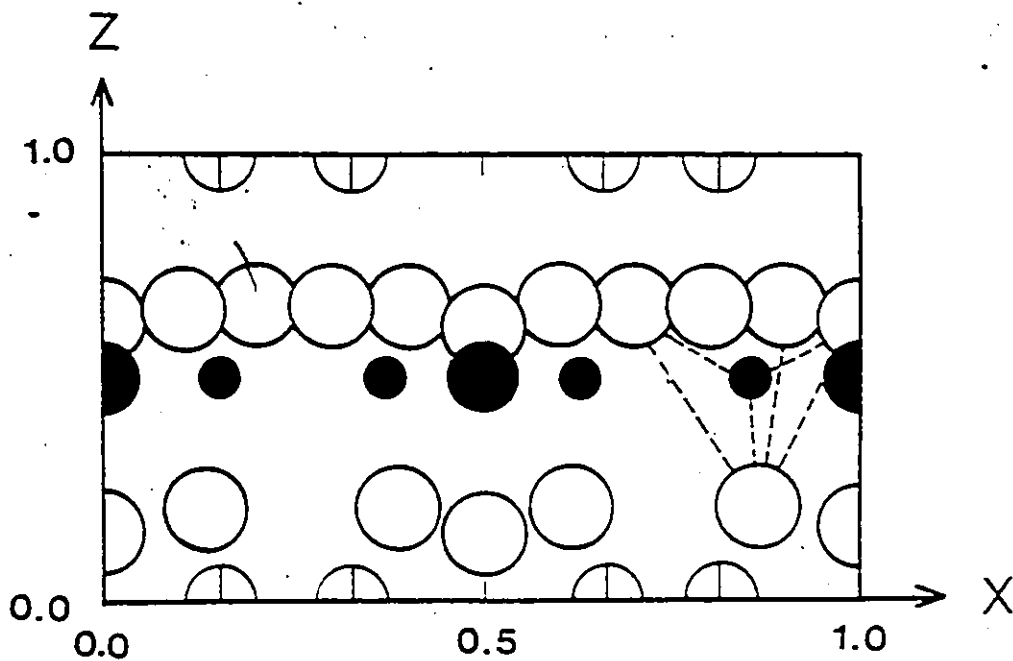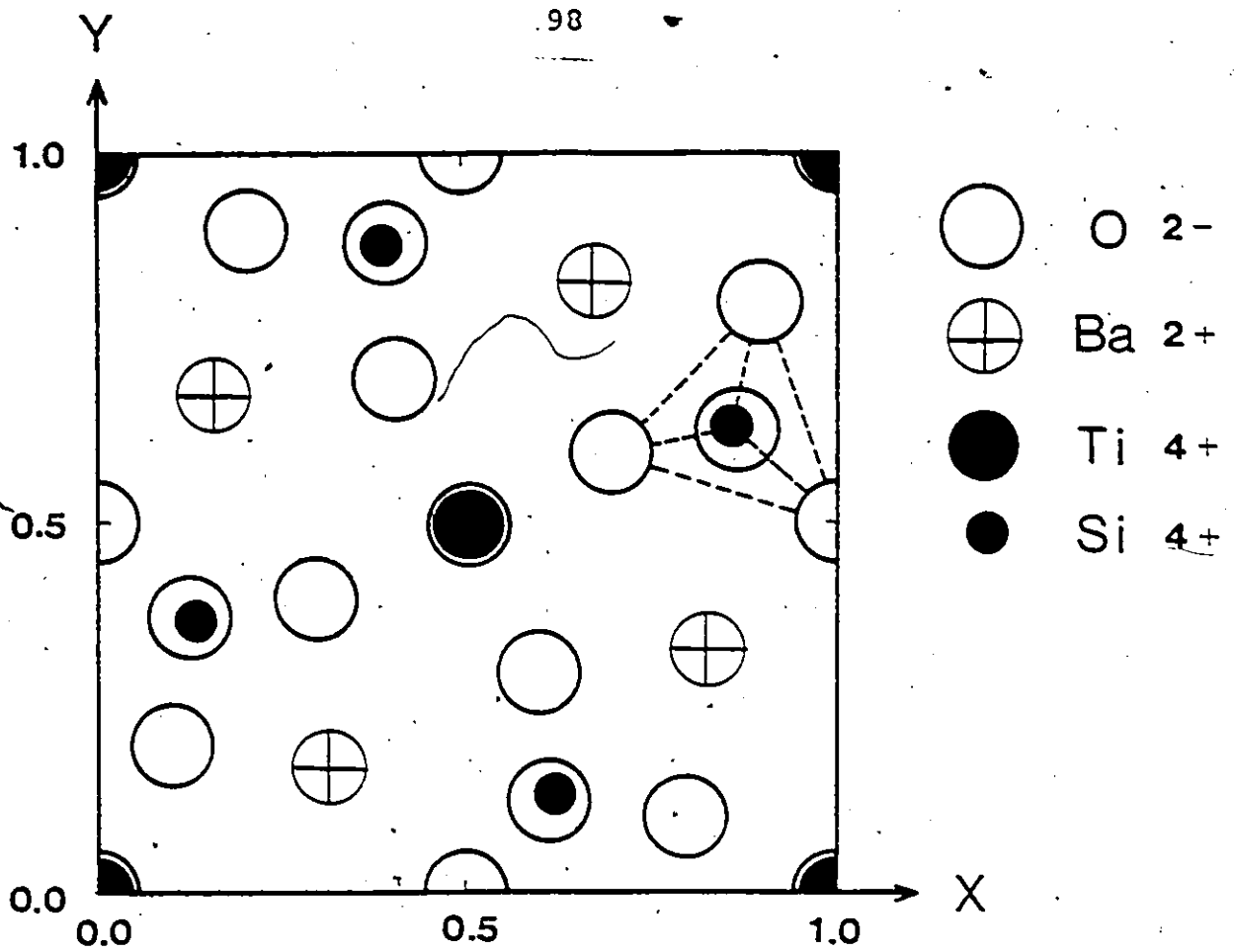
Figure 11 (a')(b) Structure of $Ba_2Si_2TiO_8$

(a') projection on X-Y plane

(b) projection on X-Z plane   Ref. (46).(47).

STEP 1	Weighing		
STEP 2	Powder Mixing	in ball mill with distilled water	~10 hrs.
STEP 3	Drying (I)		100°C, ~15 hrs.
STEP 4	Grinding	in ball mill or mortar with distilled water	~ 1 hr.
STEP 5	Presintering (Calcination)		~1000°C, ~10 hrs.
STEP 6	Crushing	in ball mill with acetone	~24 hrs.
STEP 7	Drying (II)		~ 100°C, ~15 hrs.
STEP 8	Pressing		~3.45 MPa
STEP 9	Sintering		~1250°C, ~ 5 hrs.

Figure 12   Fabrication Procedure of Fresnoite Ceramic Disk for Sputtering Target
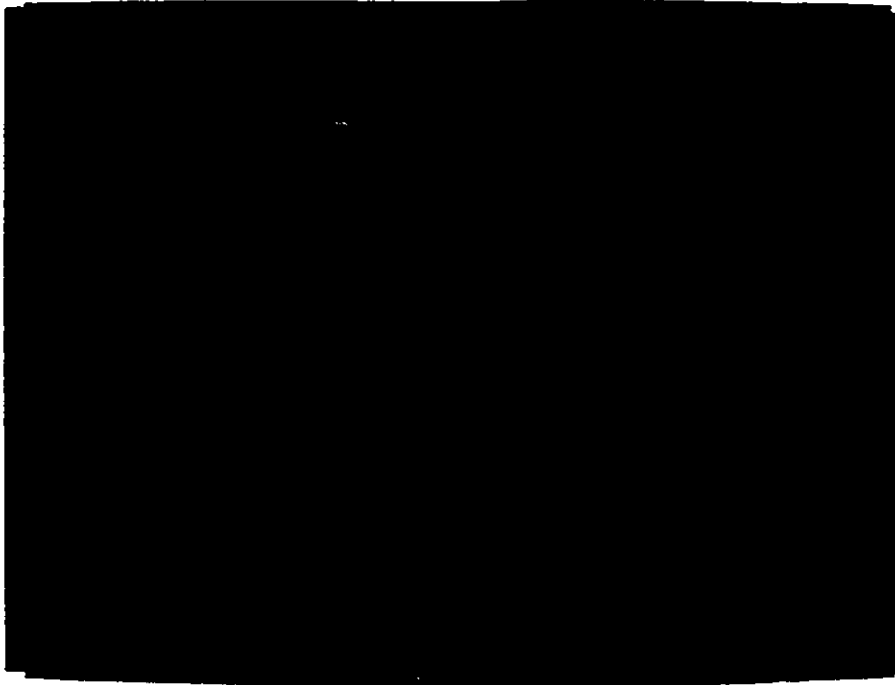
(a)
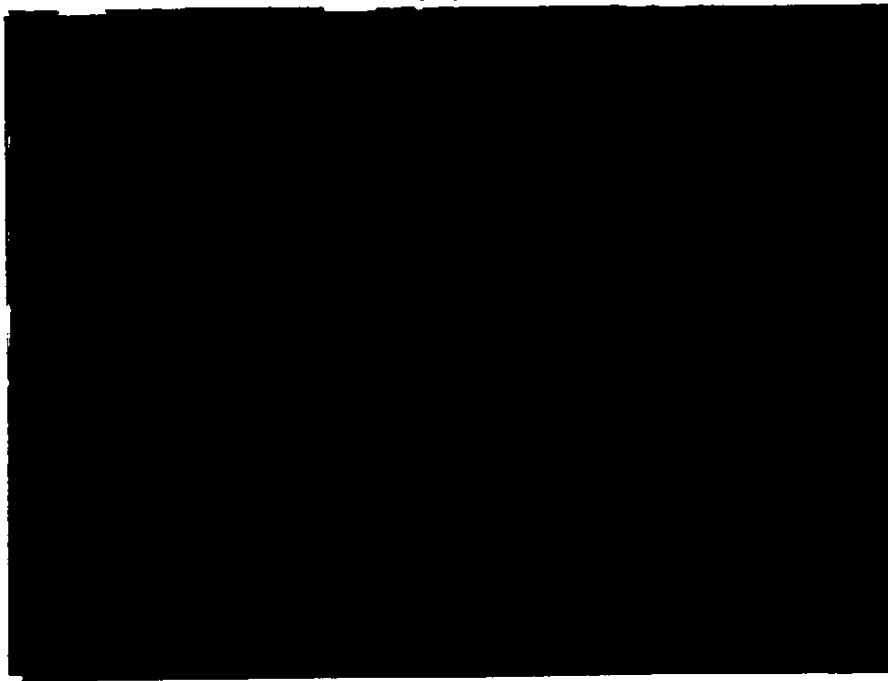
(b)

Figure 13 (a),(b)   Scanning electron micrographs of
$BaCO_3$ raw powder.

(c)
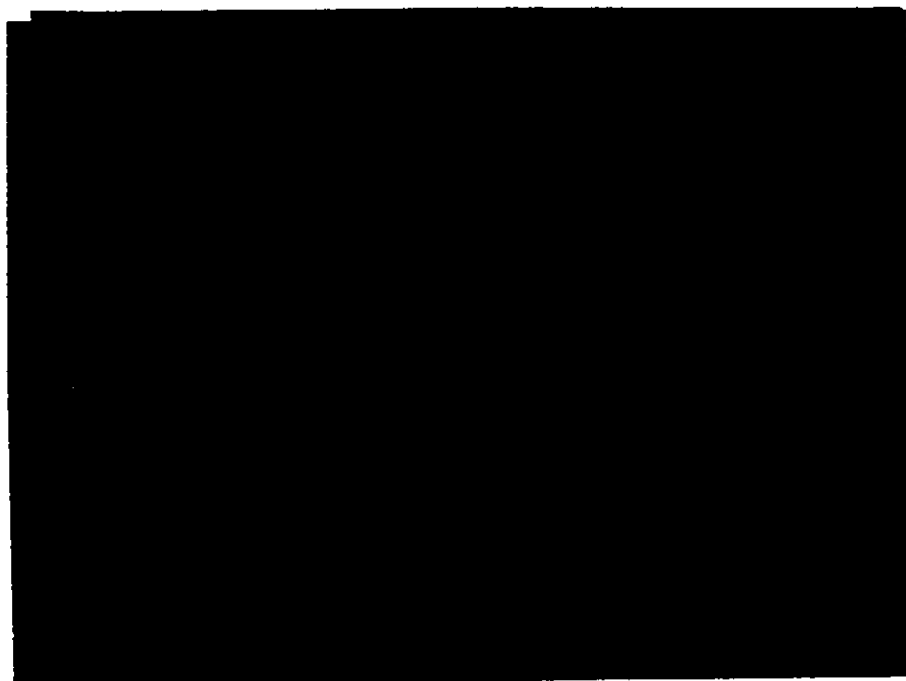
(d)

Figure 13 (c),(d). Scanning electron micrographs of
SiO$_2$ raw powder.

(e)
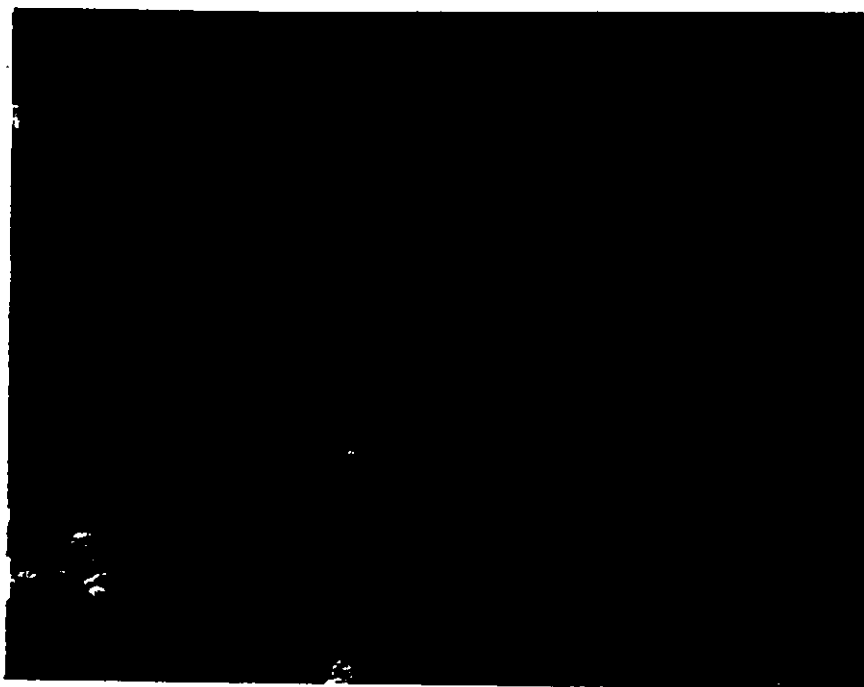
(f)

Figure 13 (e),(f)   Scanning electron micrographs of
TiO_2 raw powder.
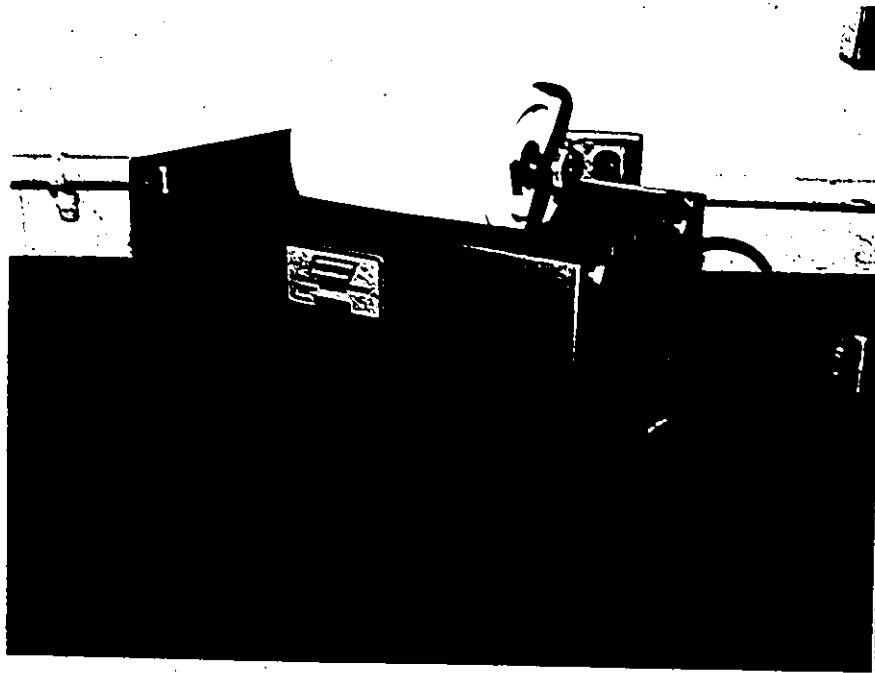
Figure 14   Ball mill (JAR MILL NORTON)

container jar and roter
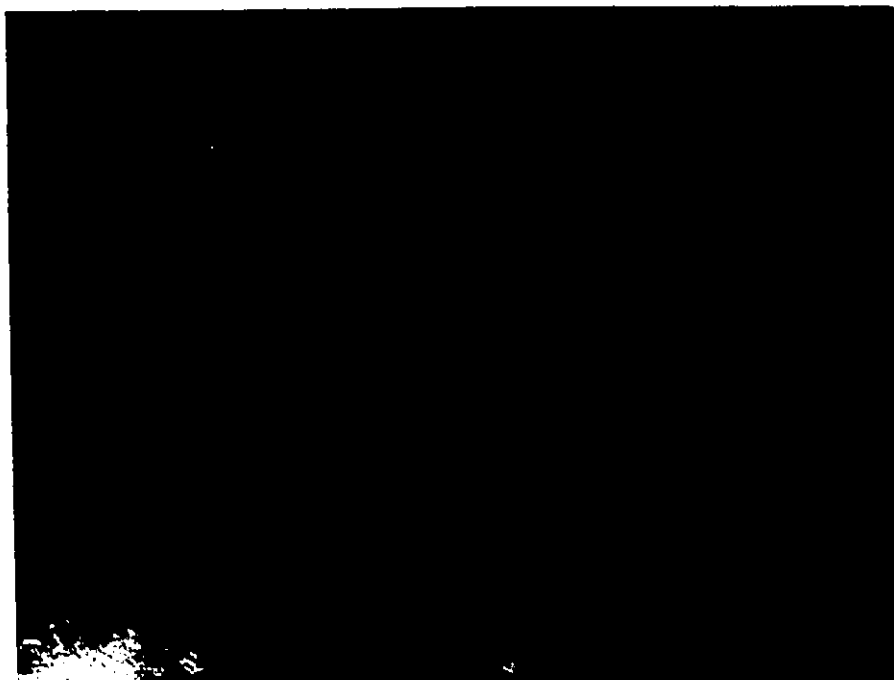
(a)
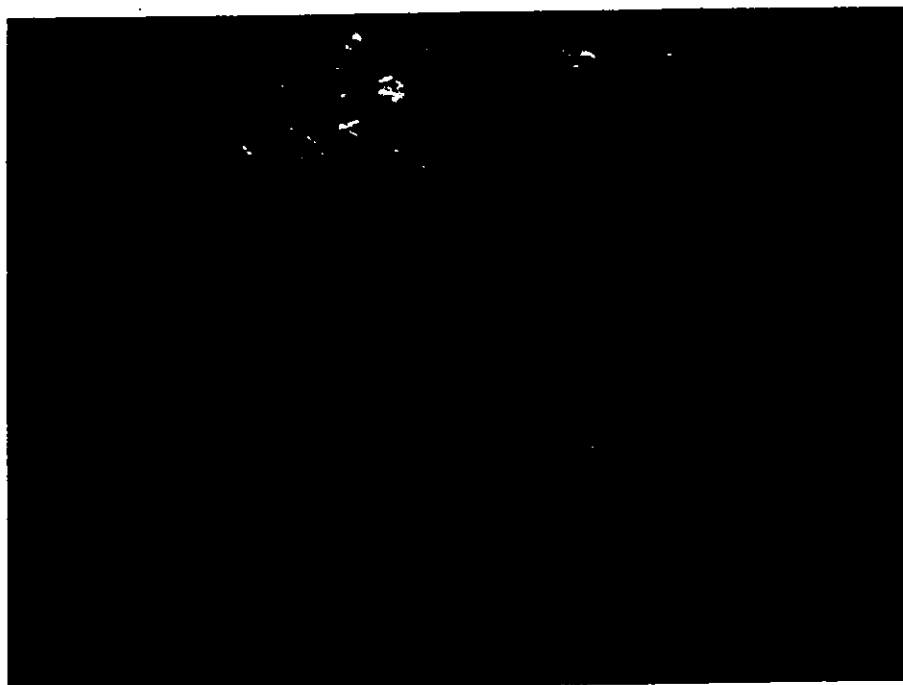
(b)

Figure 15 Scanning electron micrographs of powder
mixture of $BaCO_3$, SiO_2 and TiO_2 after 24
hours mixing in ball mill.
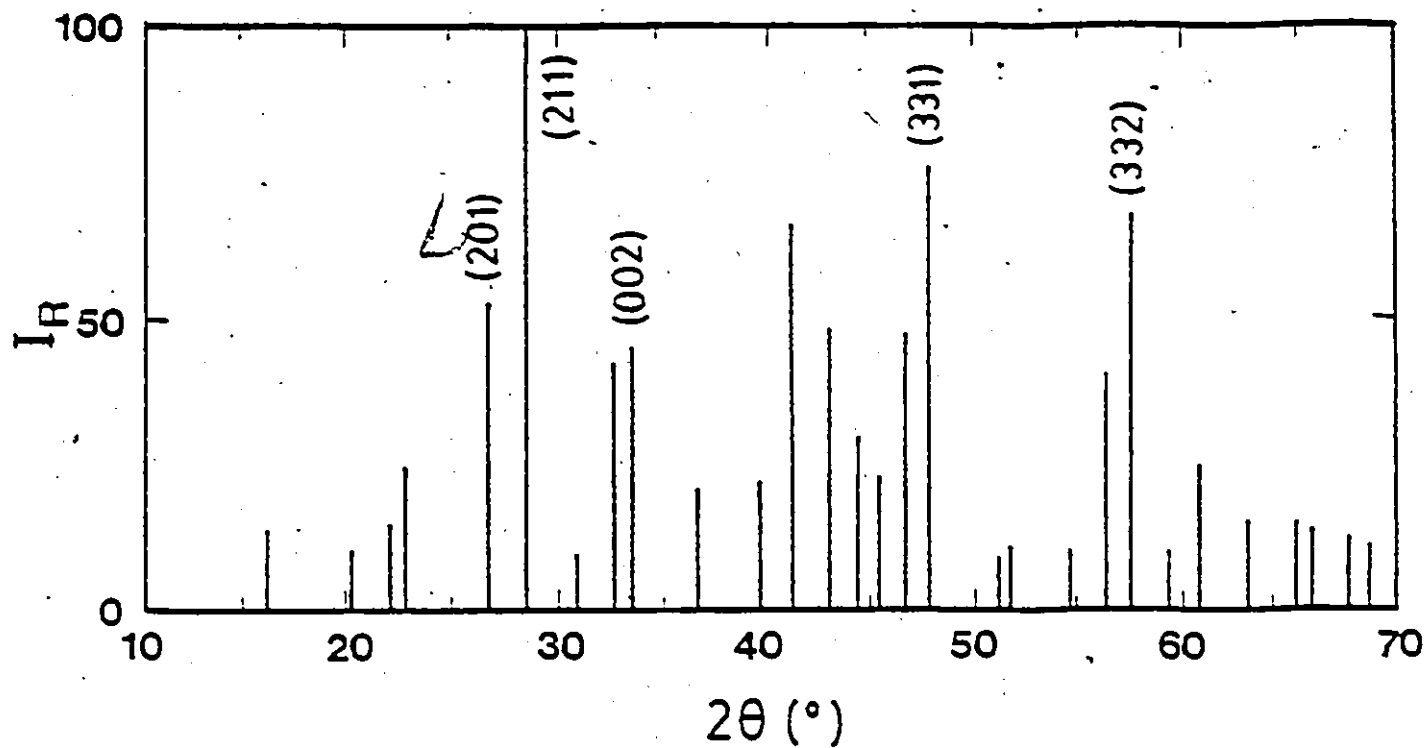
(a)
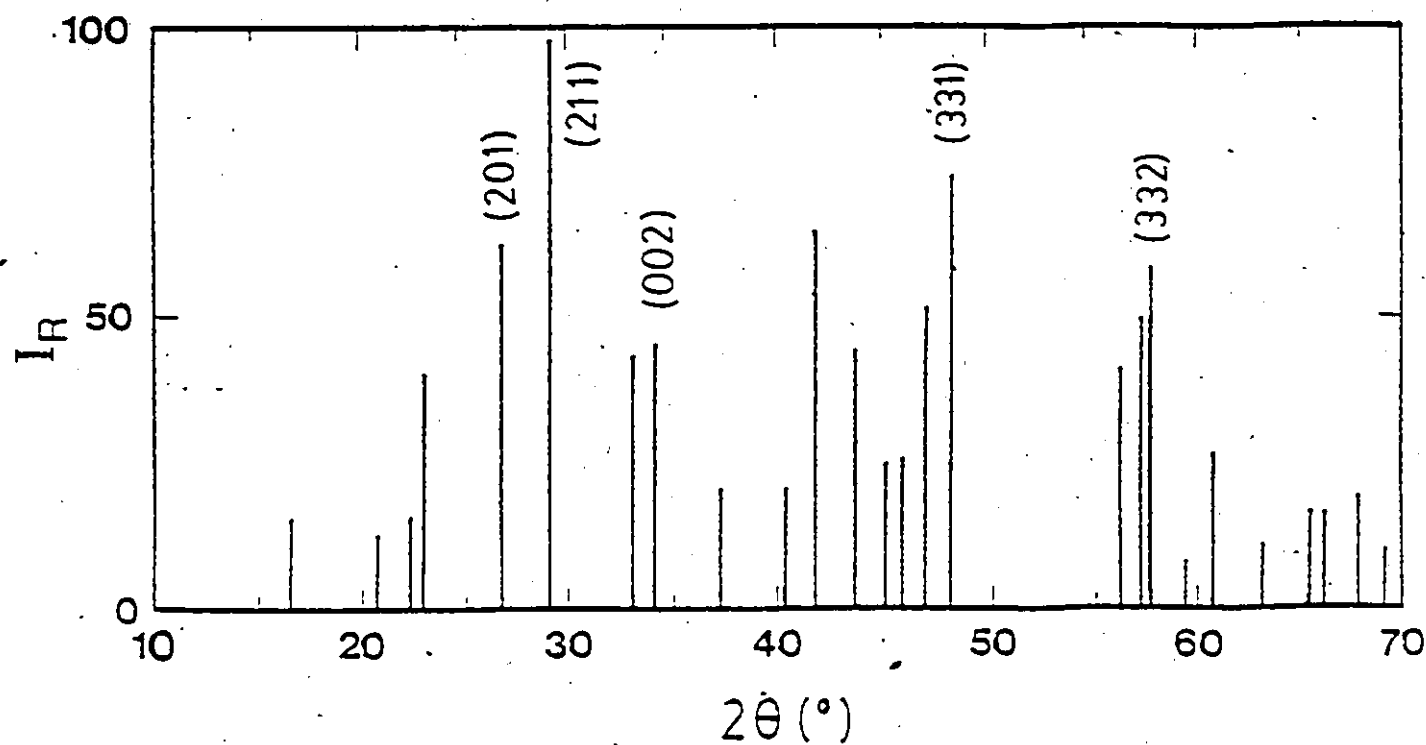
(b)

Figure 16   Schematic x-ray diffraction patterns,I_R(in arbitrary
unit) vs 2θ (diffraction angle),(a) for Specimens
T1 and T2(stoichiometric BST composition) and (b)
for Specimen T3(stoichiometric BST composition +5w.t.
%SiO$_2$).
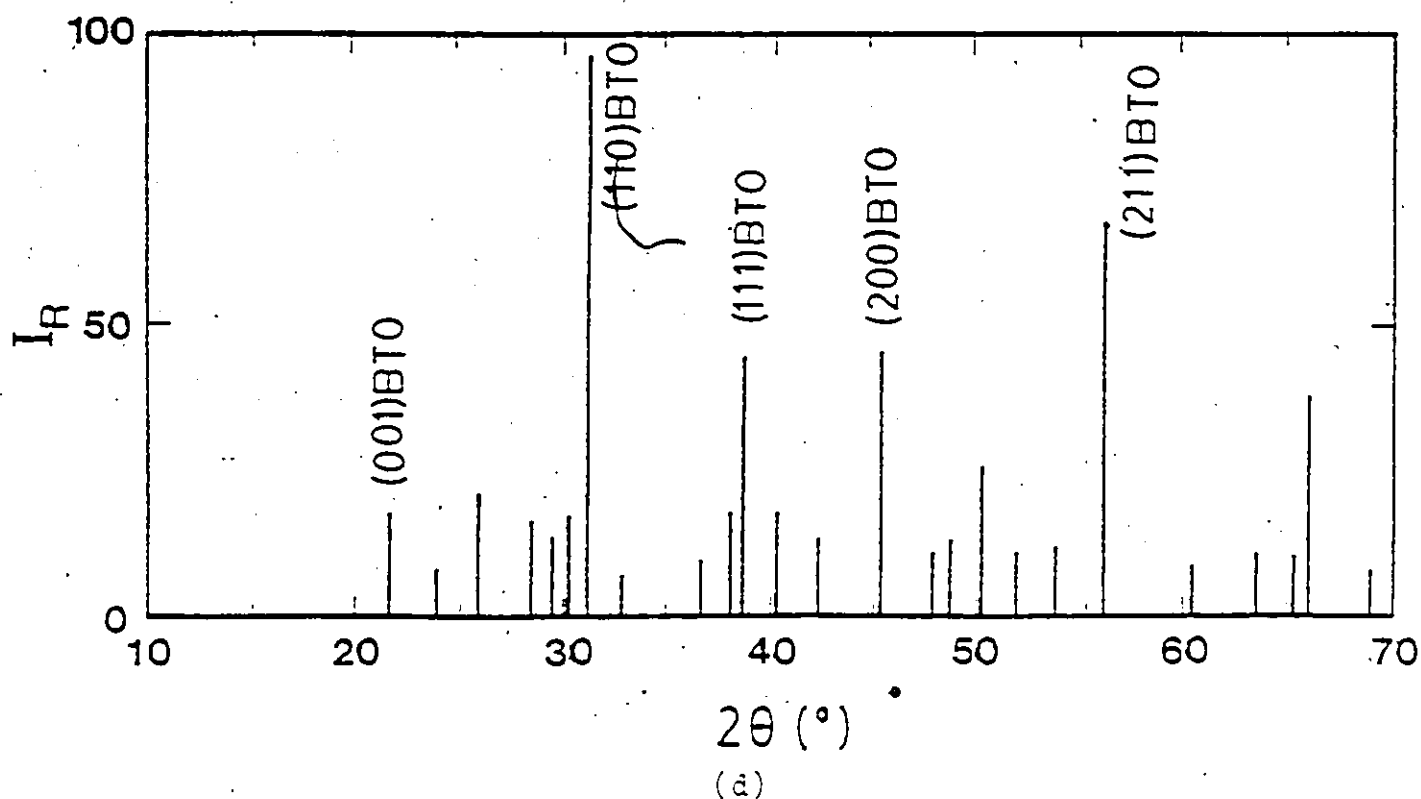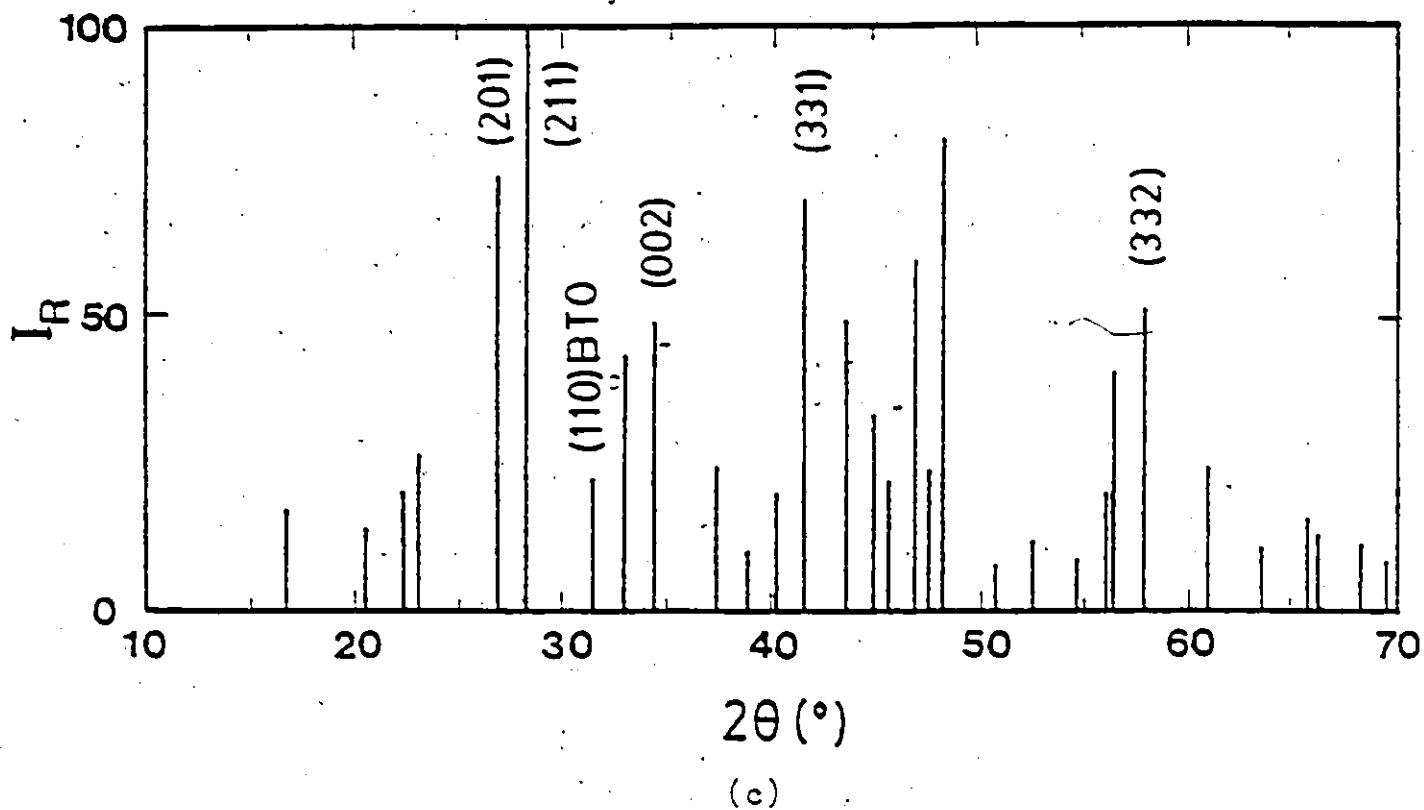
(c)

(d)

Figure 16   Schematic x-ray diffraction patterns, I_R(in arbitrary
unit) vs 2θ(diffraction angle),(c) for Specimen T4
(stoichiometric BST composition +5w.t.%TiO_2) and (d)
for Specimen T5(stoichiometric BST composition +5w.t.
%$BaCO_3$).   BTO indicates $BaTiO_3$.
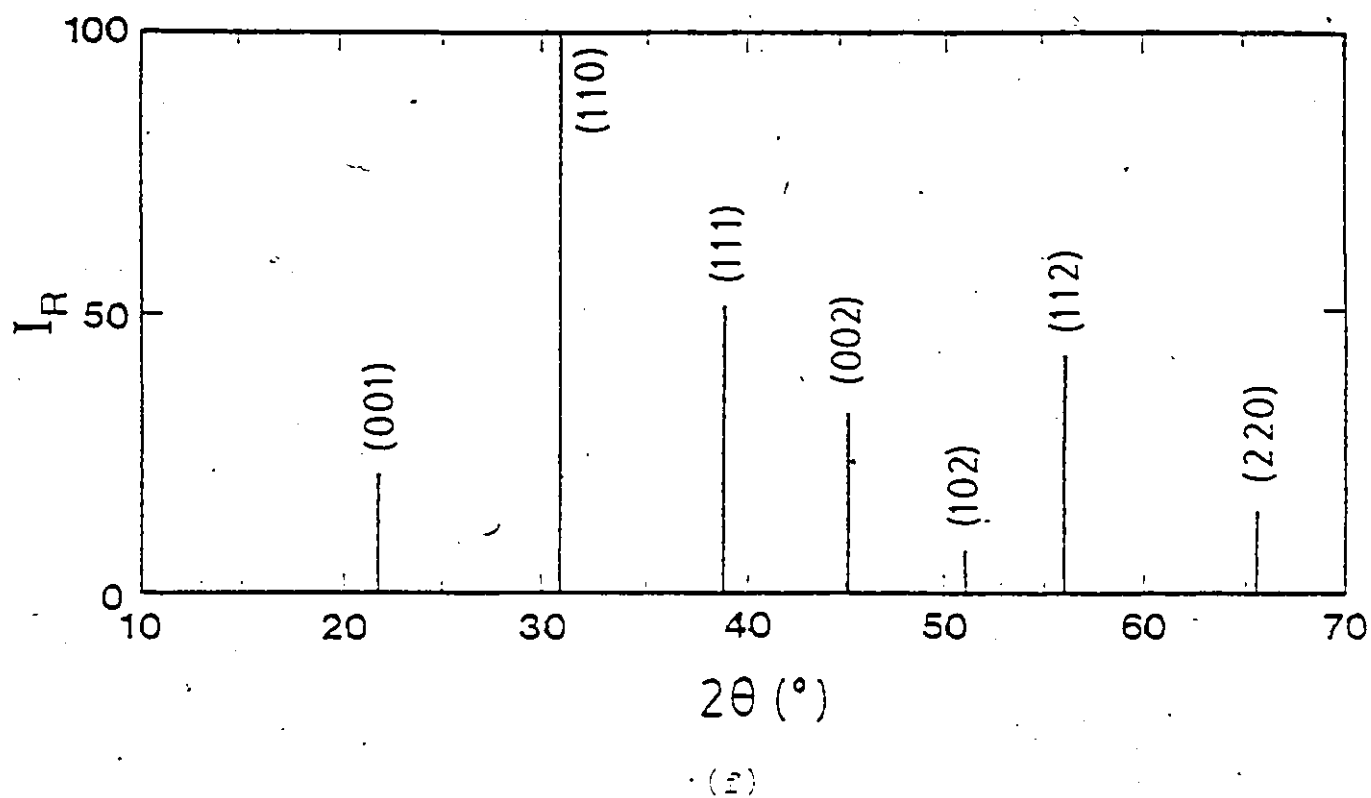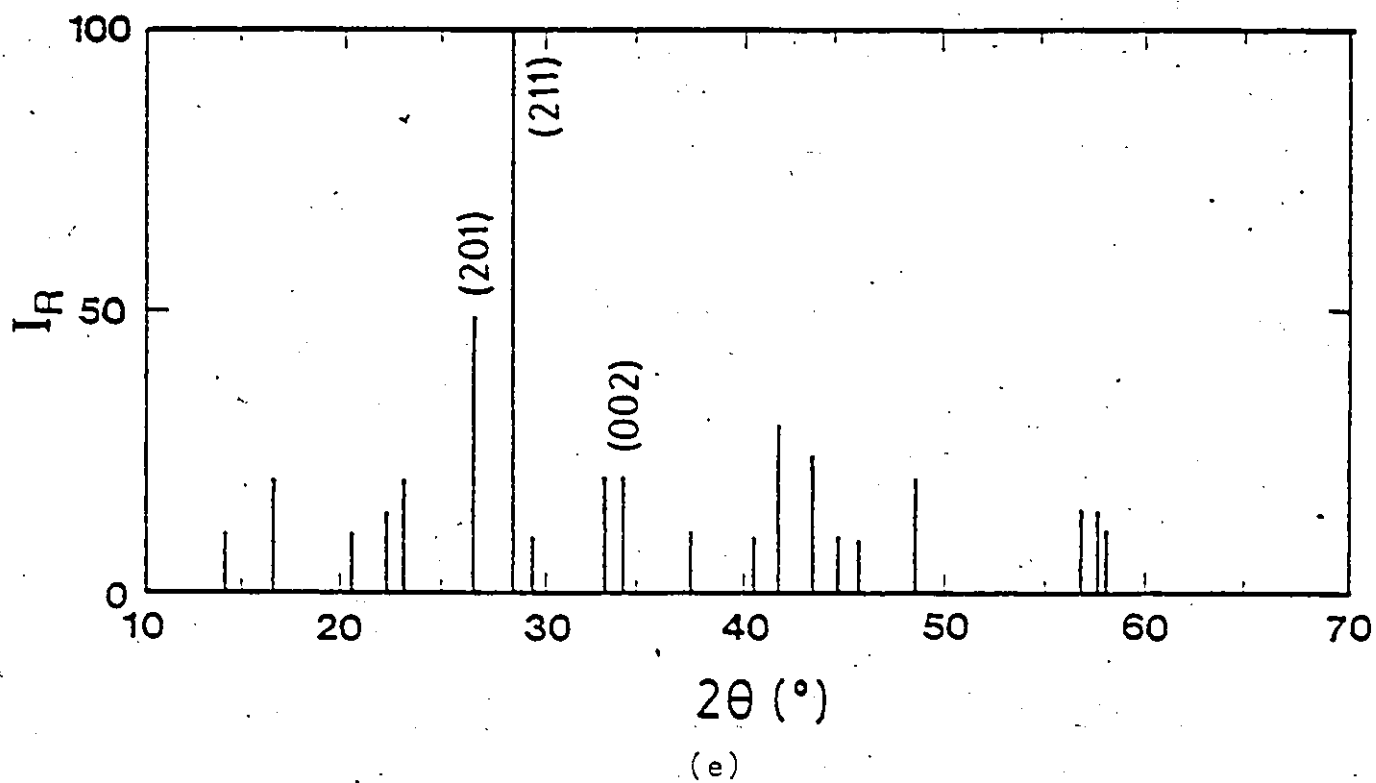
(e)

(f)

Figure 16   Schematic x-ray diffraction patterns, I_R(in arbitrary unit) vs 2θ(diffraction angle), (e) for $Ba_2Si_2TiO_3$ (ASTM FILE 18-197) and (f) for $BaTiO_3$ (ASTM FILE 5-626).
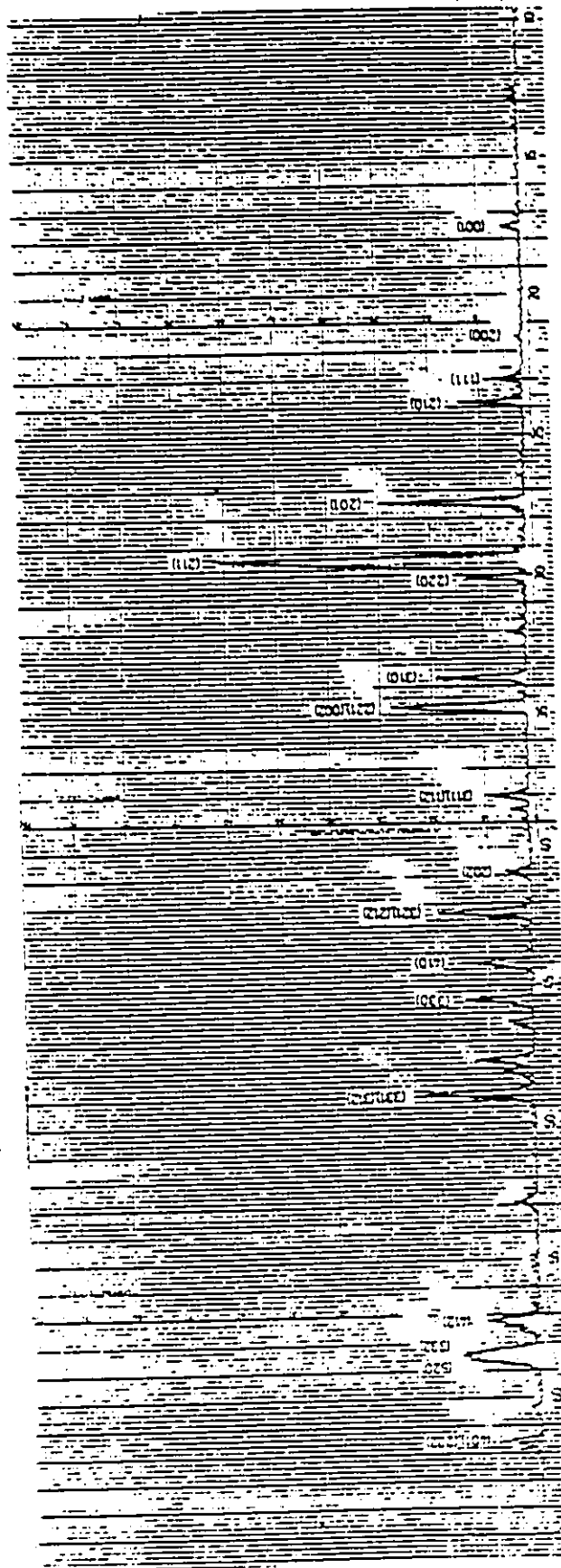
26 (diffraction angle)

Figure 17 (a). Experimental x-ray diffraction pattern, I (arbitrary unit), vs 2θ (diffraction angle) for Specimen T1. See Table 4 for preparation conditions of T1.

I (arbitrary unit)
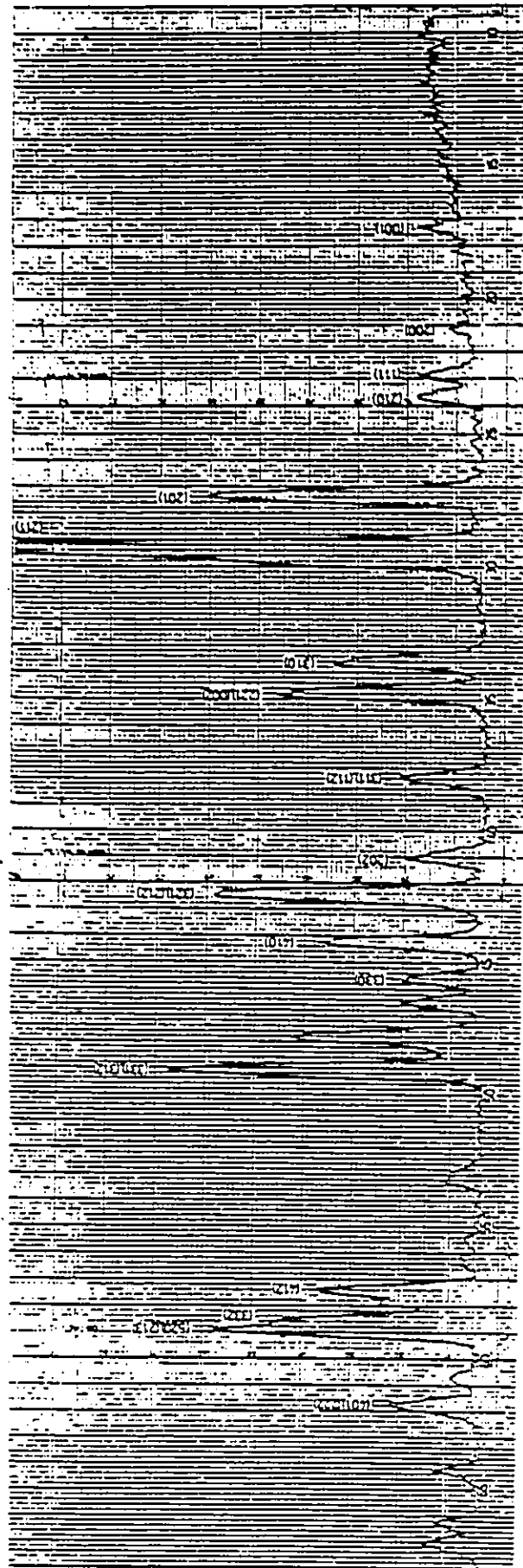
20 (diffraction angle)

Figure 17 (b) Experimental x-ray diffraction pattern, I (arbitrary unit) vs 2θ (diffraction angle) for Specimen T3. See Table 4 for the preparation conditions of T3.
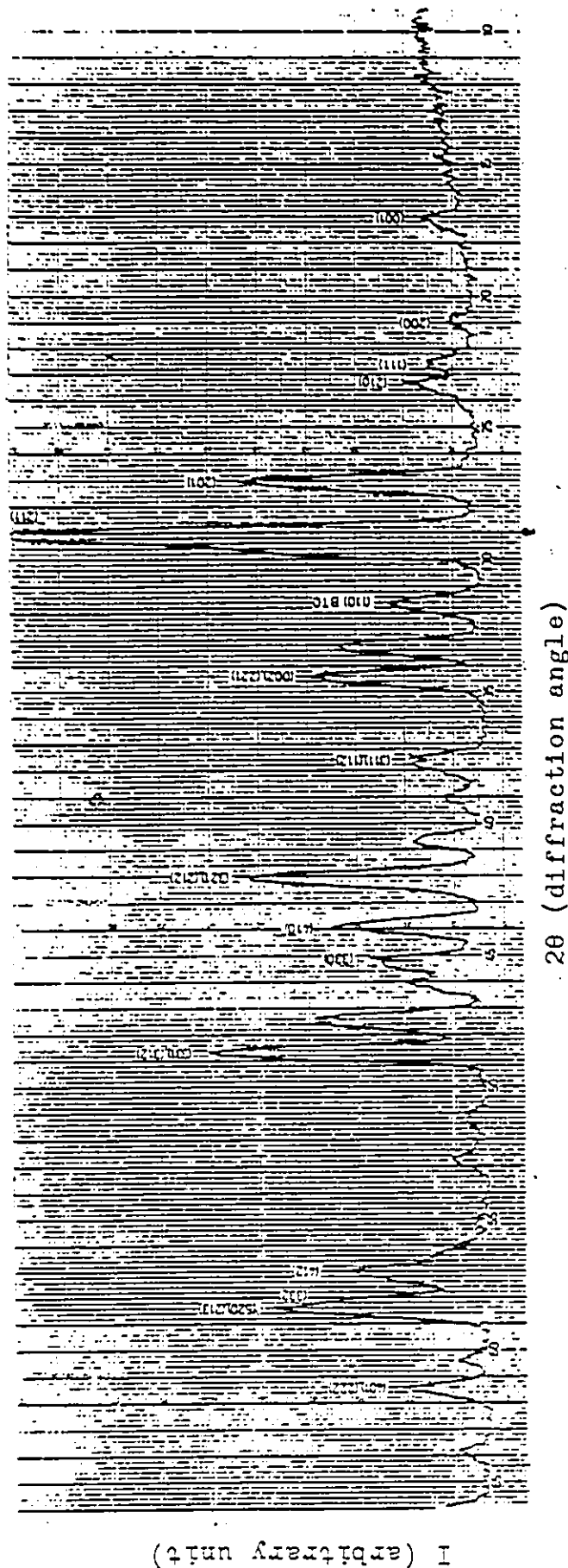
Figure 17 (c) Experimental x-ray diffraction pattern, I (arbitrary unit) vs 2θ (diffraction angle) for Specimen T4. See Table 4 for the preparation conditions of T4.
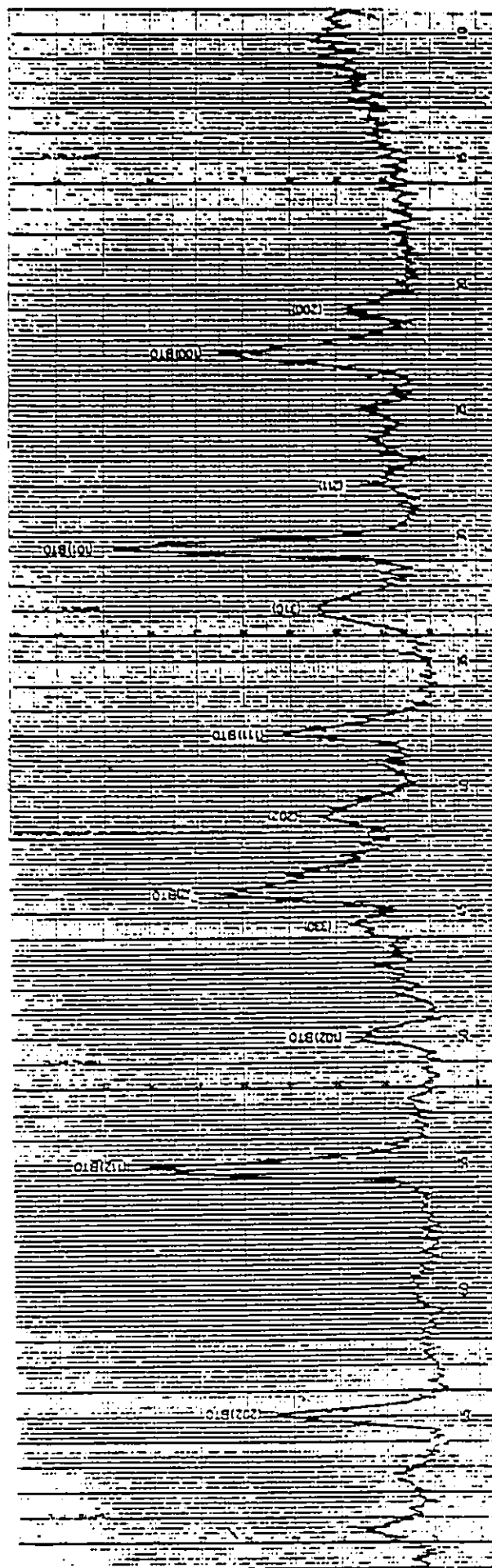
2θ (diffraction angle)

Figure 17 (d) Experimental x-ray diffraction pattern, I (arbitrary unit) vs 2θ (diffracton angle) for Specimen T5. See Table 4 for the preparation conditions of T5.
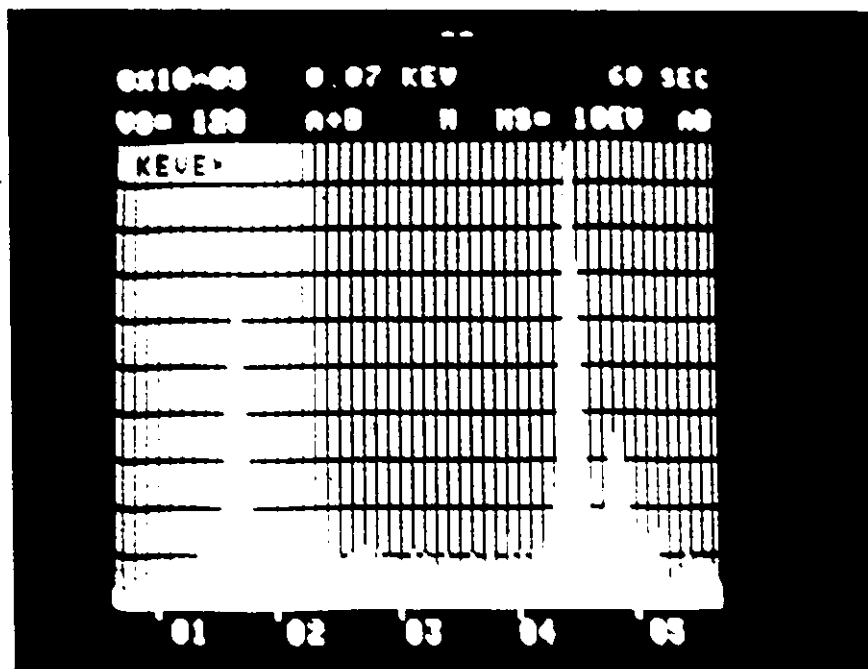
(a)
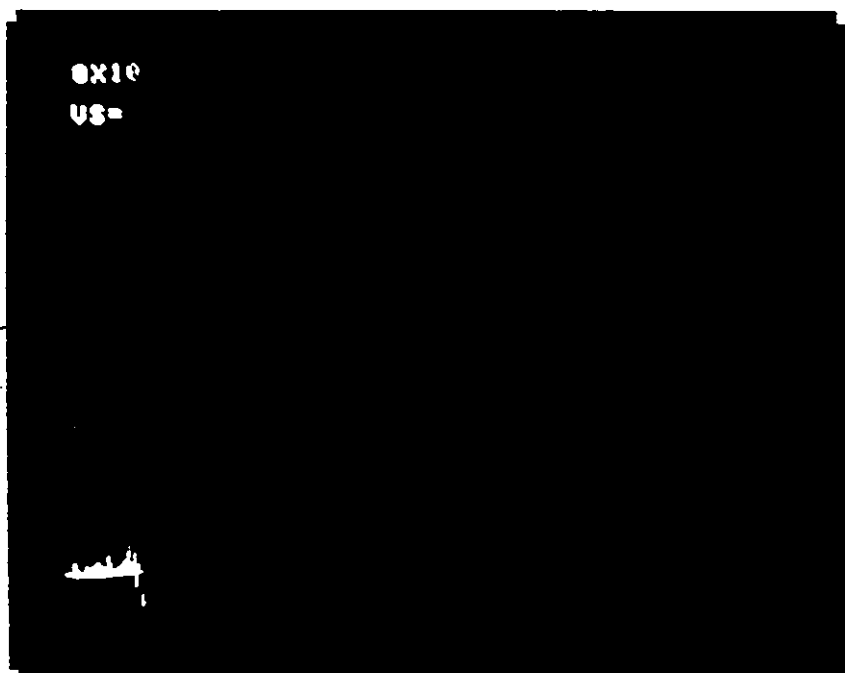
(b)

Figure 18   Energy dispersion spectra using kevex for (a) Specimen
             T1 and (b) T2. See Table 10 for the preparation condi-
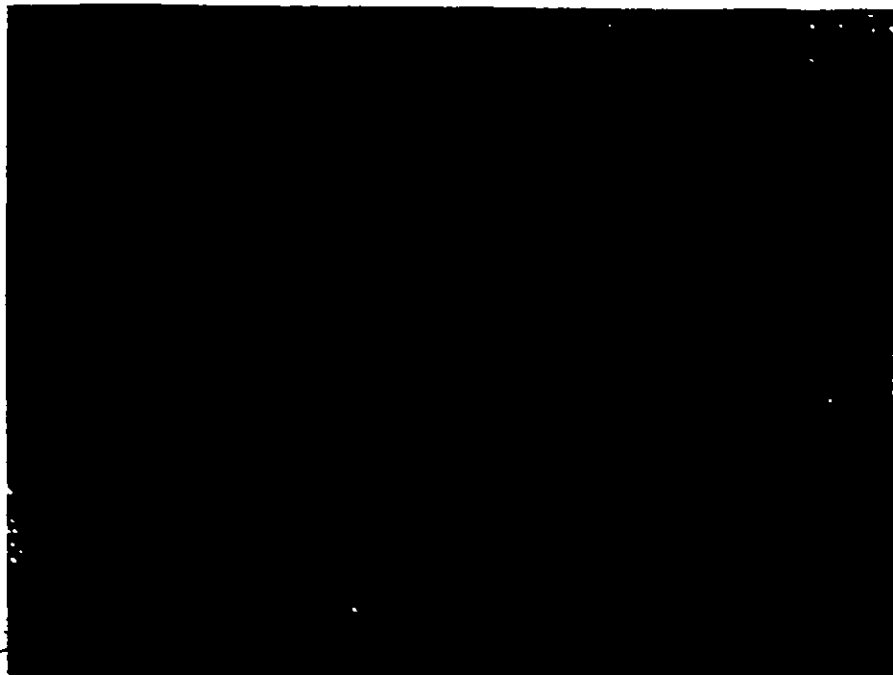   tions of T1 and T2.
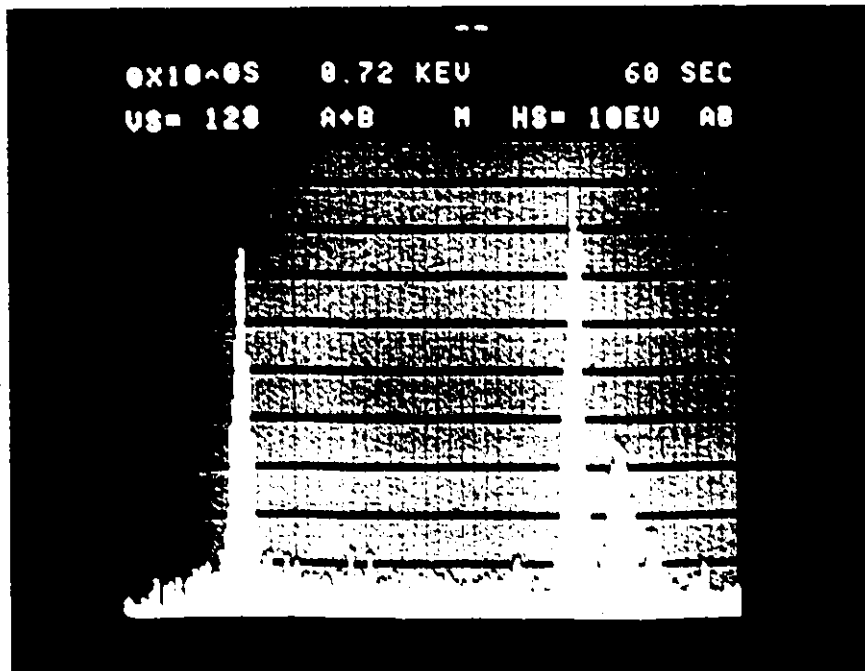
(c)
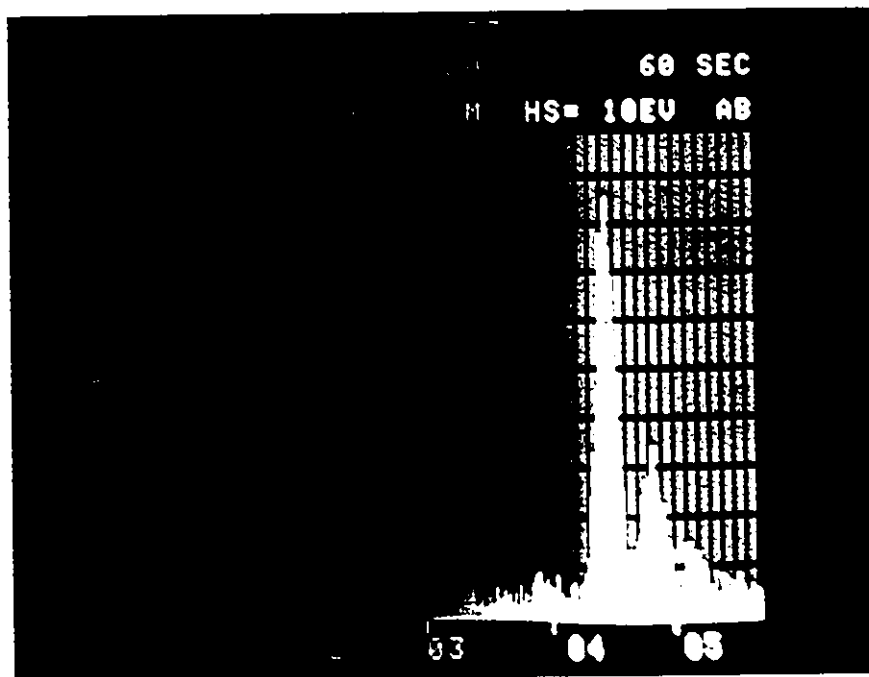
(d)

Figure 18   Energy dispersion spectra using kevex for (c) Specimen T3 and (d) T4. See Table 10 for the preparation conditions of T3 and T4.
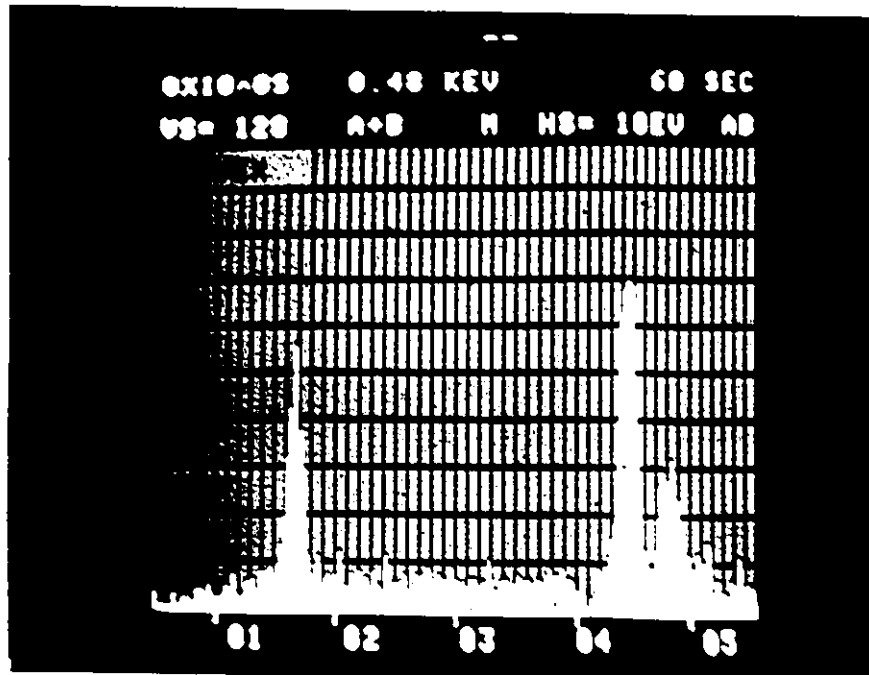
(e)

Figure 18   Energy dispersion spectra using kevex for (e) Specimen
T5. See Table 10 for the preparation conditions of T5.
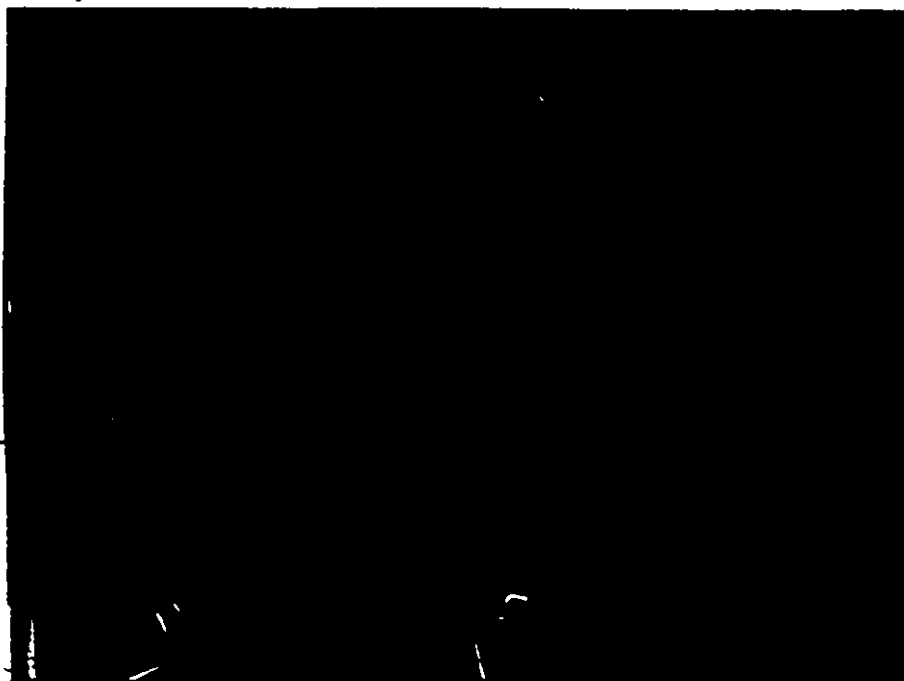
(a)   Mag. ×2,500

(b)   Mag. ×3,500

Figure 19   Scanning electron micrographs of sintered
            ceramic target for Specimen T1. See Table
            4 for the preparation conditions of T1.

Mag. ×1,200

Figure 20   Scanning electron micrograph of sintered
ceramic target for Specimen T2. See Table
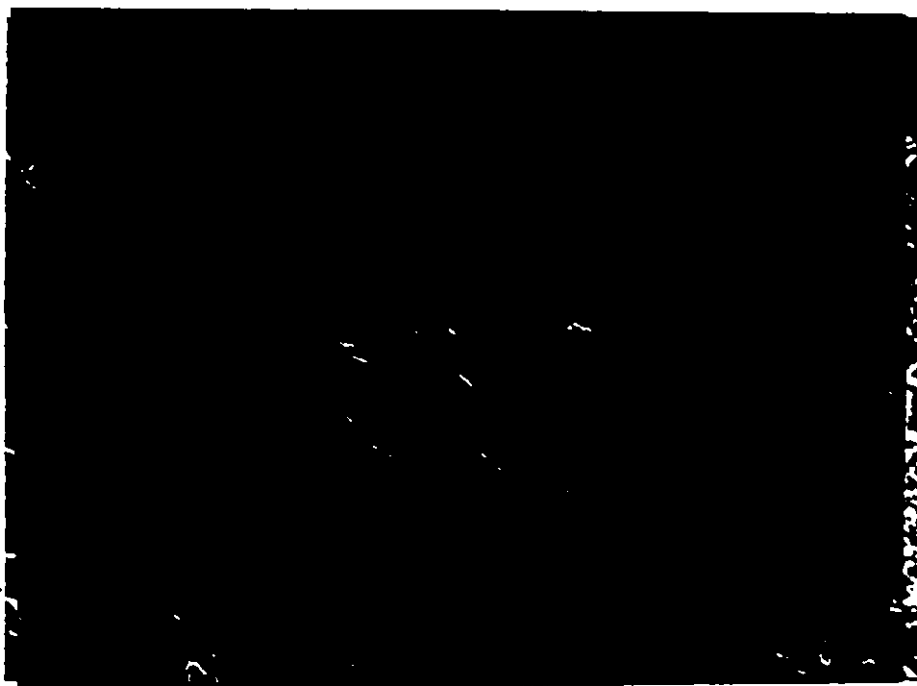4 for the preparation conditions of T2.

(a)   Mag. ×1,200
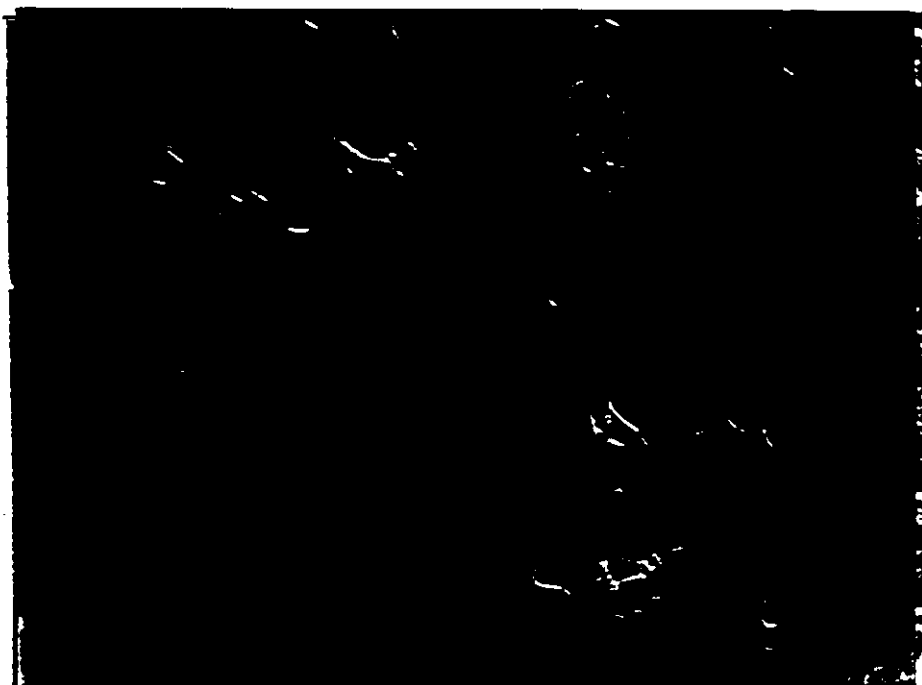
(b)   Mag. ×2,500

Figure 21   Scanning electron micrographs of sintered
ceramic target for Specimen T3. See Table
4 for the preparation conditions of T3.

(a)   Mag. ×1,200

(b)   Mag. ×2,500

Figure 22   Scanning electron micrographs of sintered
            ceramic target for Specimen T4.   See Table
            4 for the preparation conditions of T4.
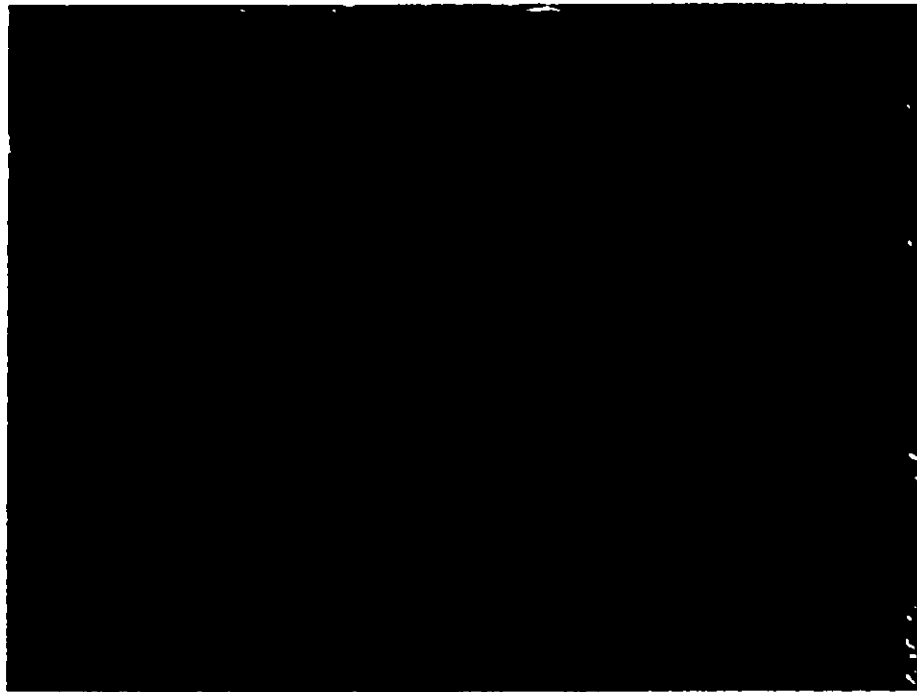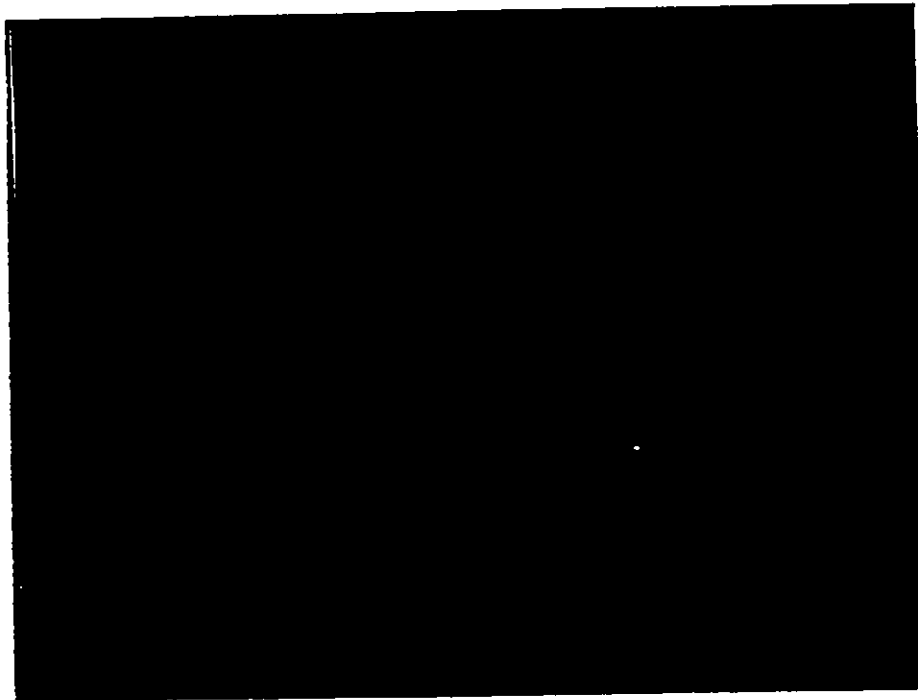
(a)

(b)

Figure 23   Scanning electron micrographs of sintered
ceramic target for Specimen T5.   See Table
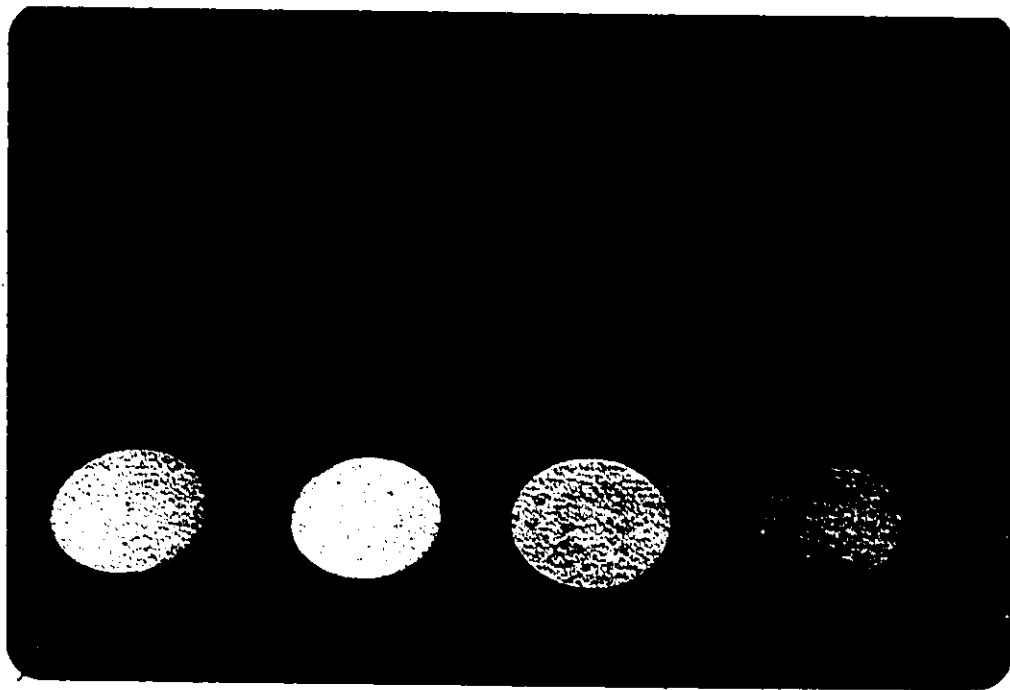4 for the preparation conditions of T5.

Figure 24 Sintered ceramic target disks. From the left
          Specimen T1,T3,T4 and T5.   See Table 4 for
          the specimens preparation conditions.

Figure 25   R.F. sputtering deposition system.
Triode sputtering source (Sinard Tri-Mag Model3121)
is installed. Details are explained in Fig.26.
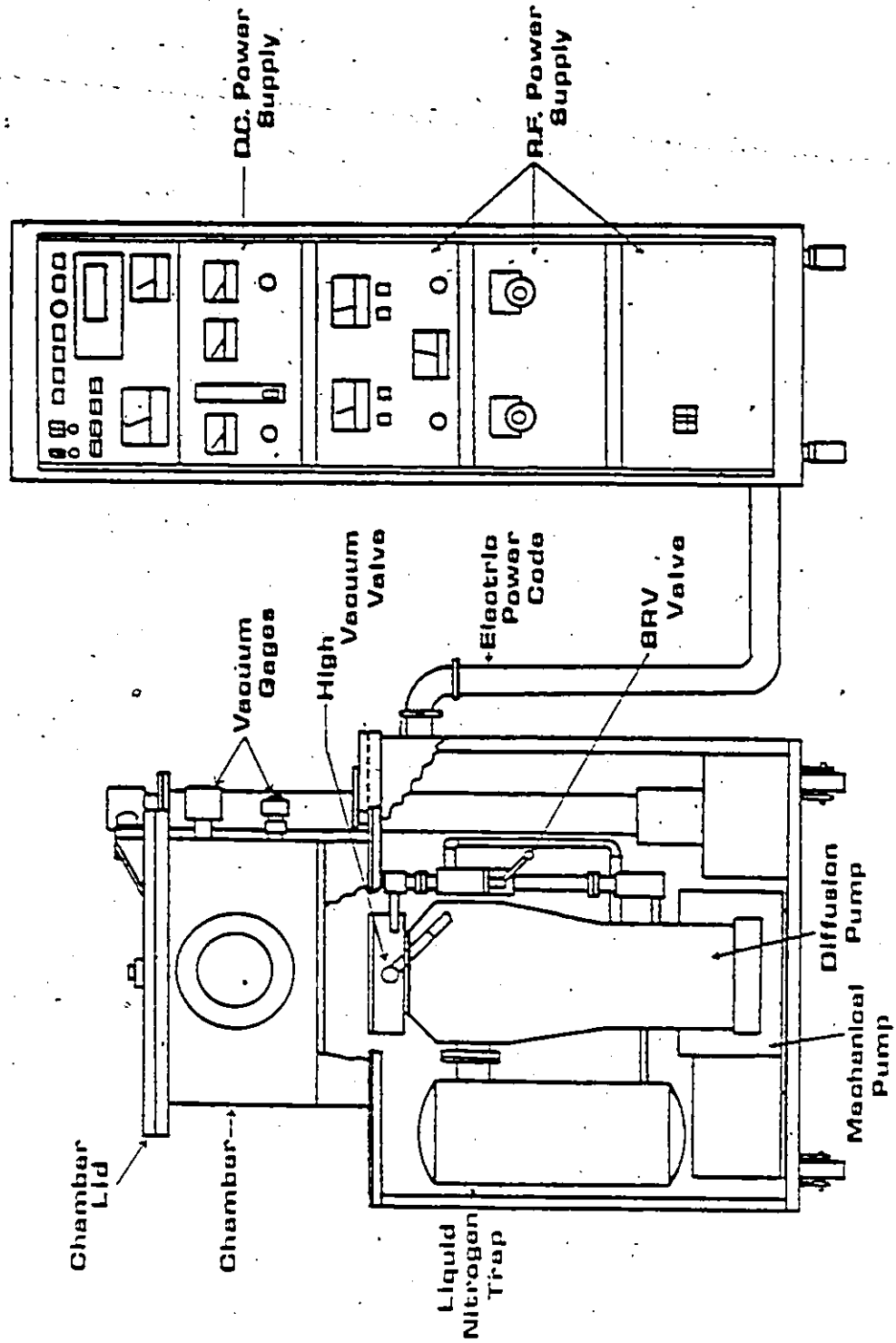
Figure 26   Schematic illustration of triode R.F. sputtering deposition system
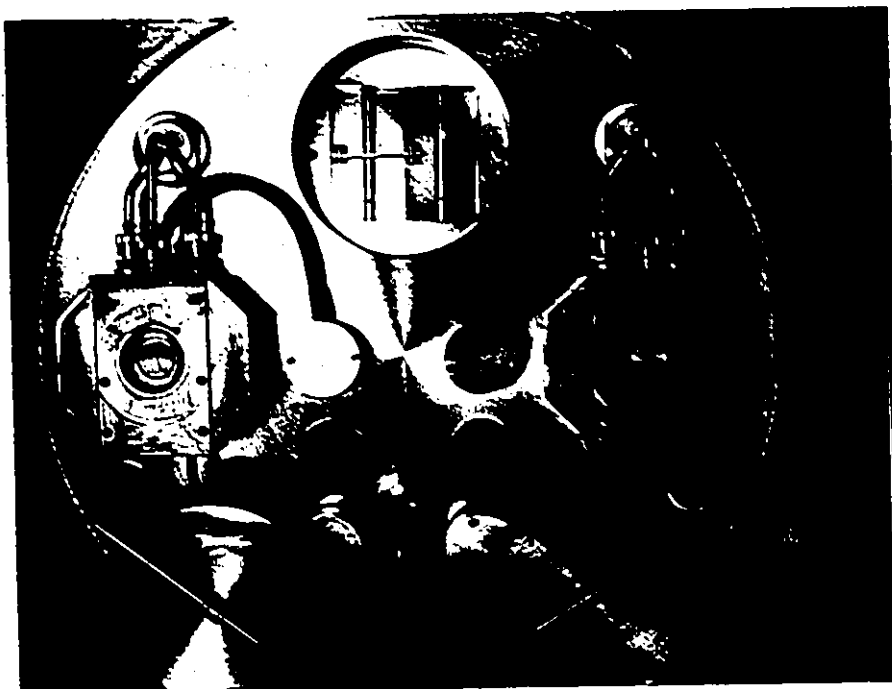
Figure 27   Sputtering sources (Simard Tri-Mag Model 3121) inside
             the vacuum chamber.

124
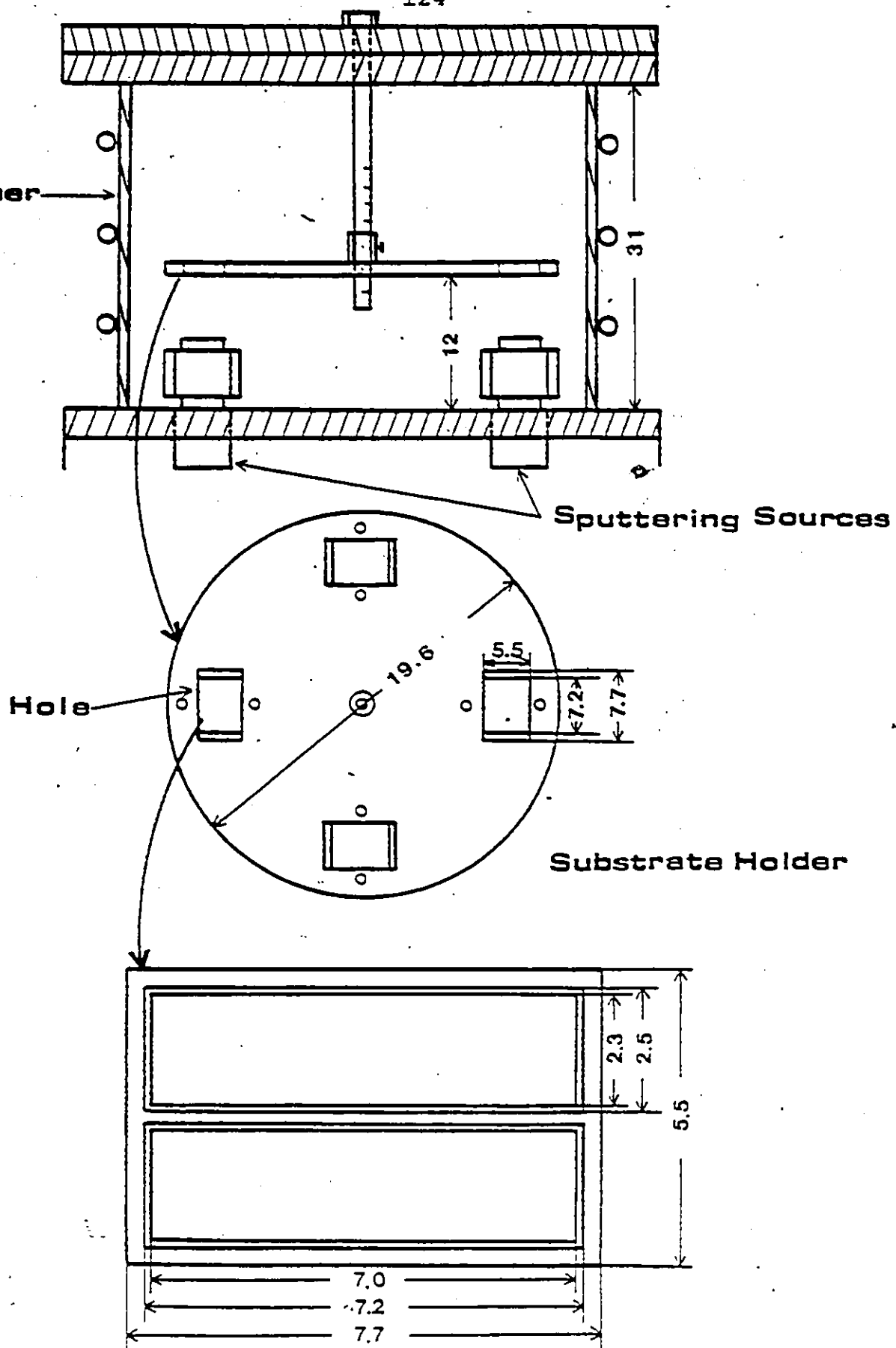
Figure 28 Substrate holder and mask design.

S : Substrate
T : Target

(a) Diode Sputtering

(b) Triode Sputtering

Filament   Anode

S

T
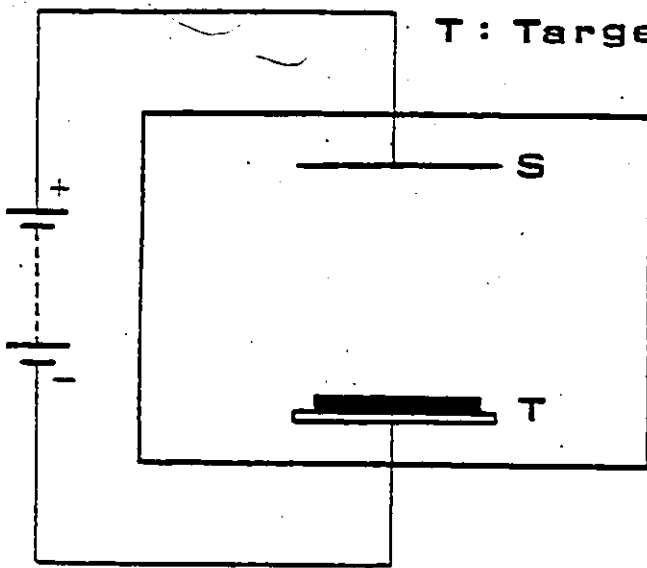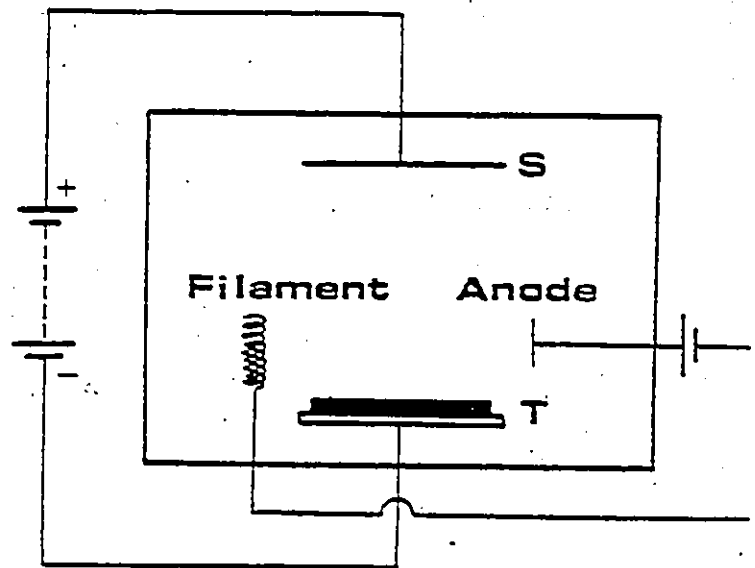
Figure 29   Schematic configuration of target and substrate:

(a)   Diode sputtering

(b)   Triode sputtering.
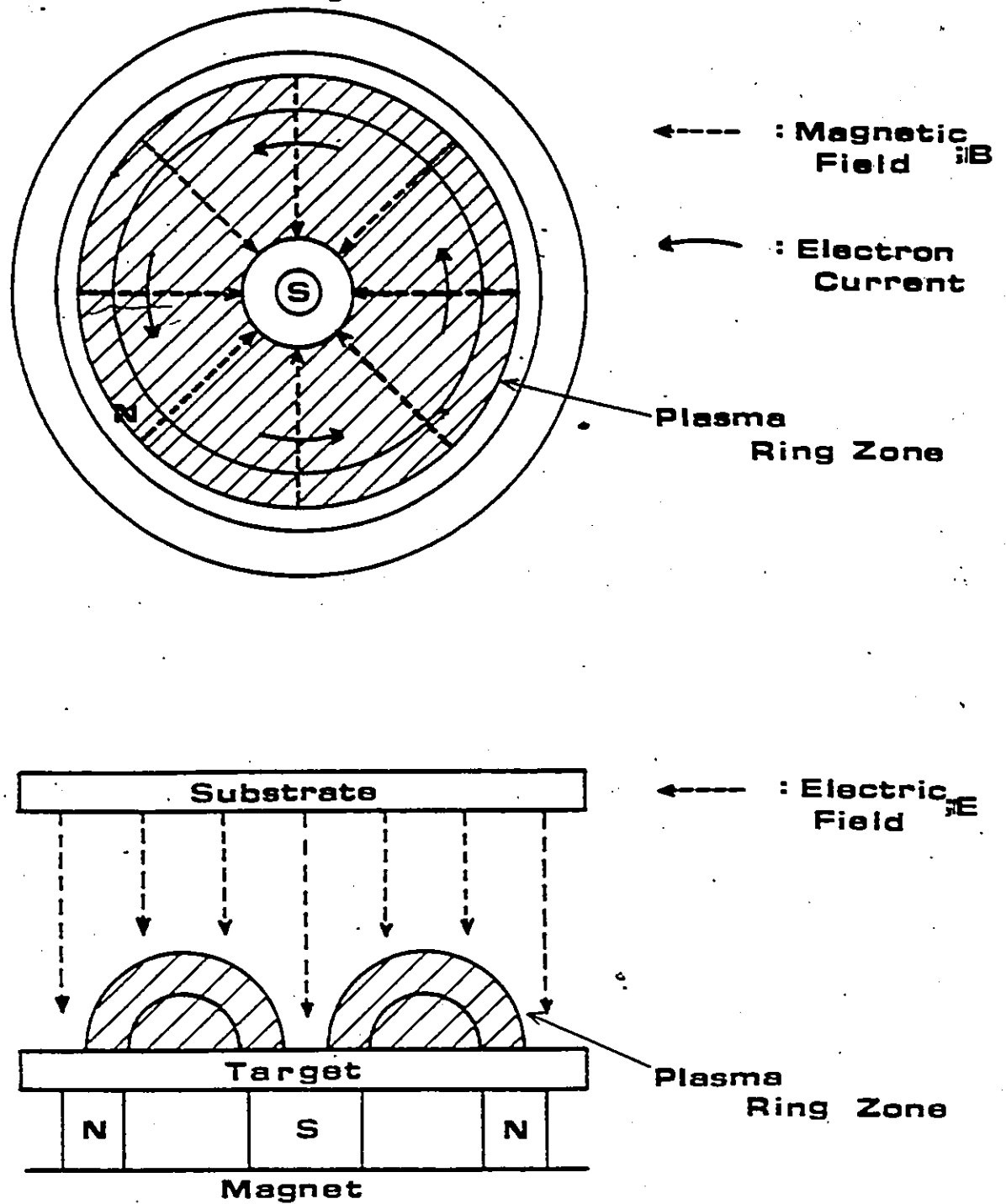
Figure 30   Schematic diagram of electric and magnetic field
            distributions in a magnetron cathode for magnetron
            sputtering method.
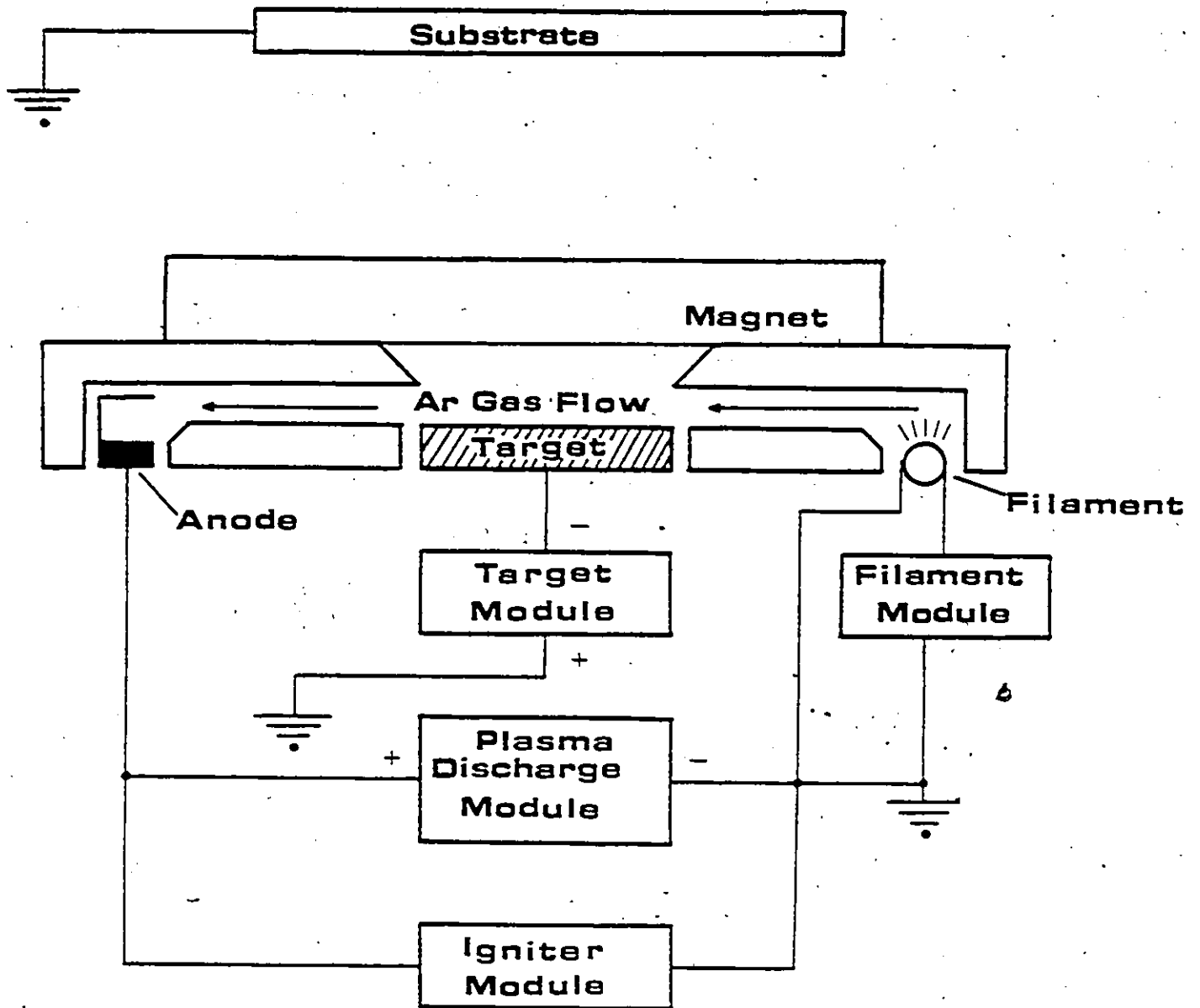
Figure 31 Schematic configuration of triode sputtering source.
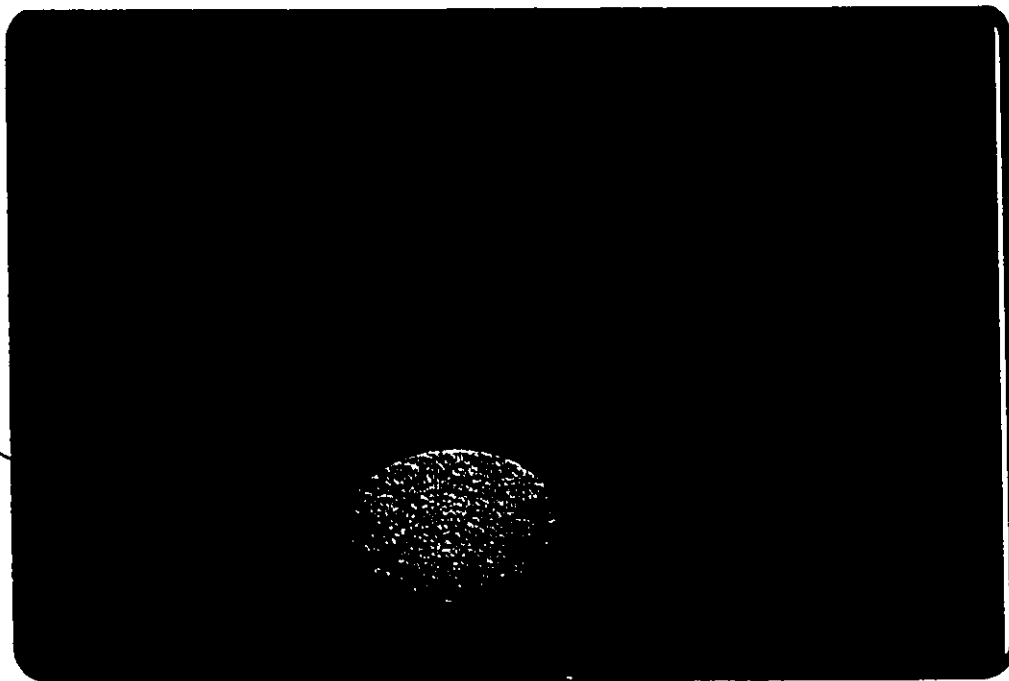
Figure 32 $Ba_2Si_2TiO_8$ sputtering target disk set on modified copper target holder.
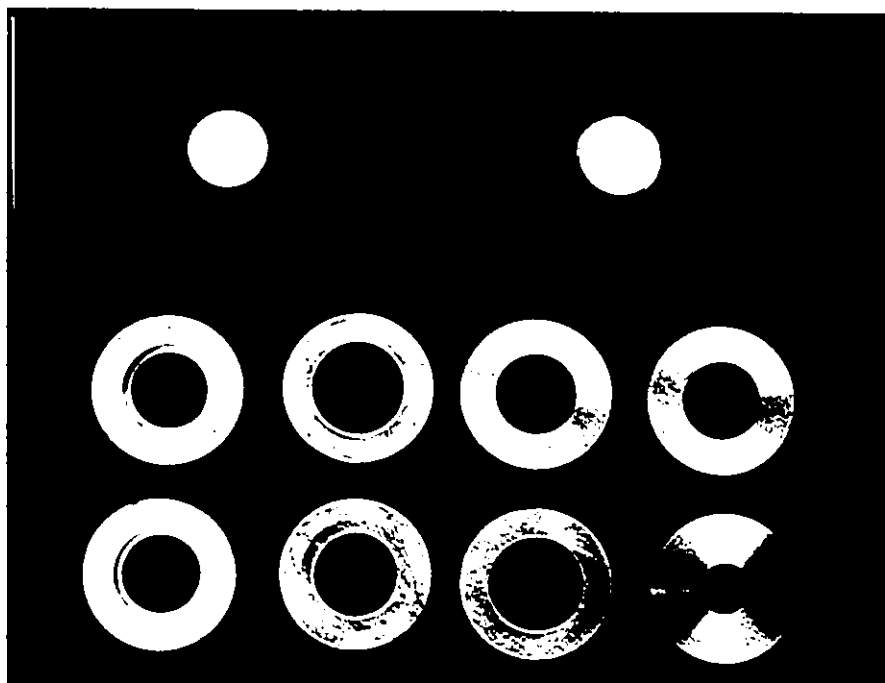
Figure 33   Al ring target inserts of various sizes.

The top twe disks are fresnoite sputtering targets.
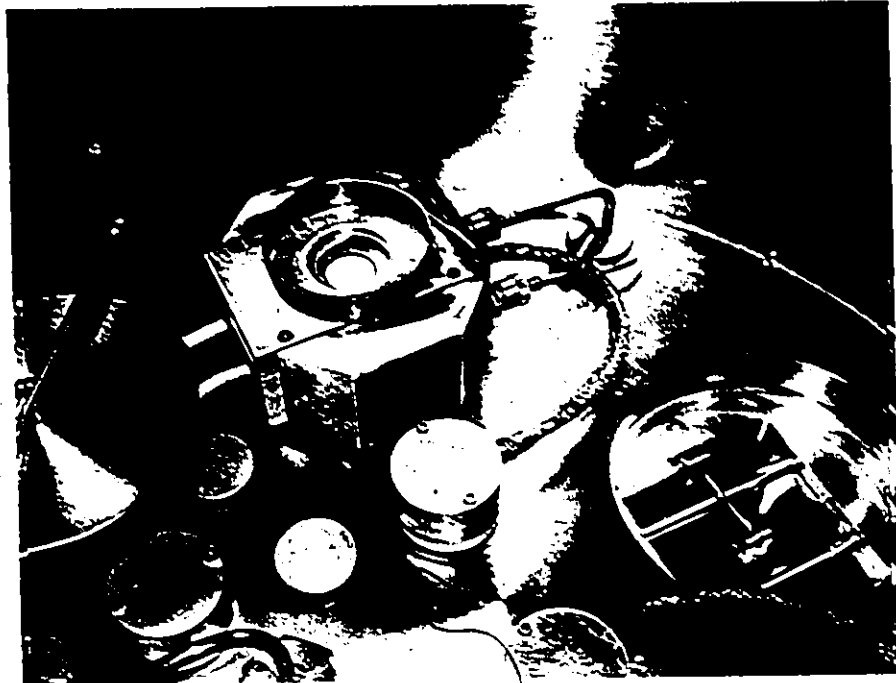
Figure 34   Fresnoite target set in the Tri-Mag sputtering source.
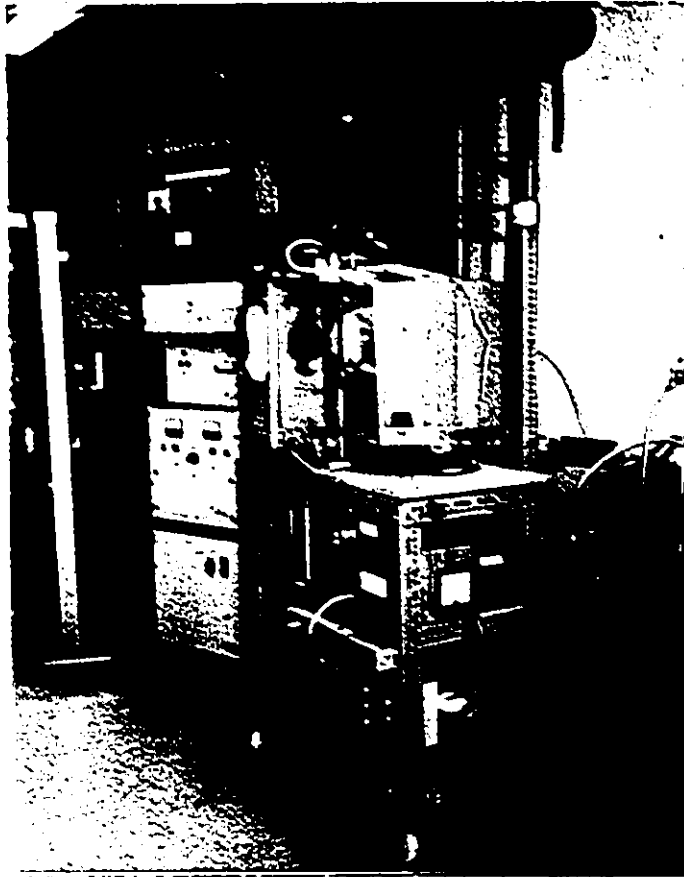
Figure 35   Diode magnetron sputtering deposition system at Queen's
             University.
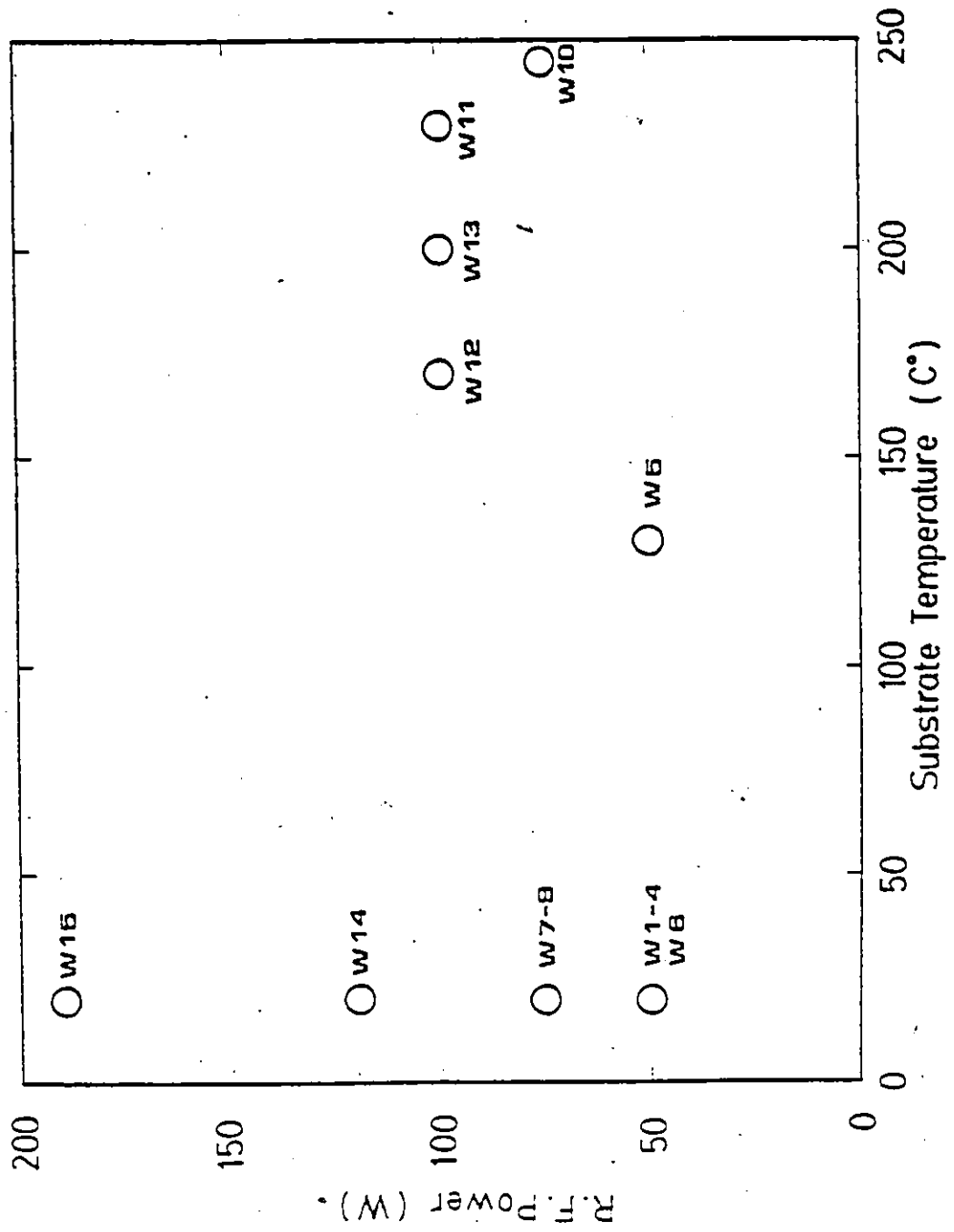
Figure 36   Summary of sample fabrication conditions. Indices(W1=W15) refers specimen numbers tabulated in Table 10.
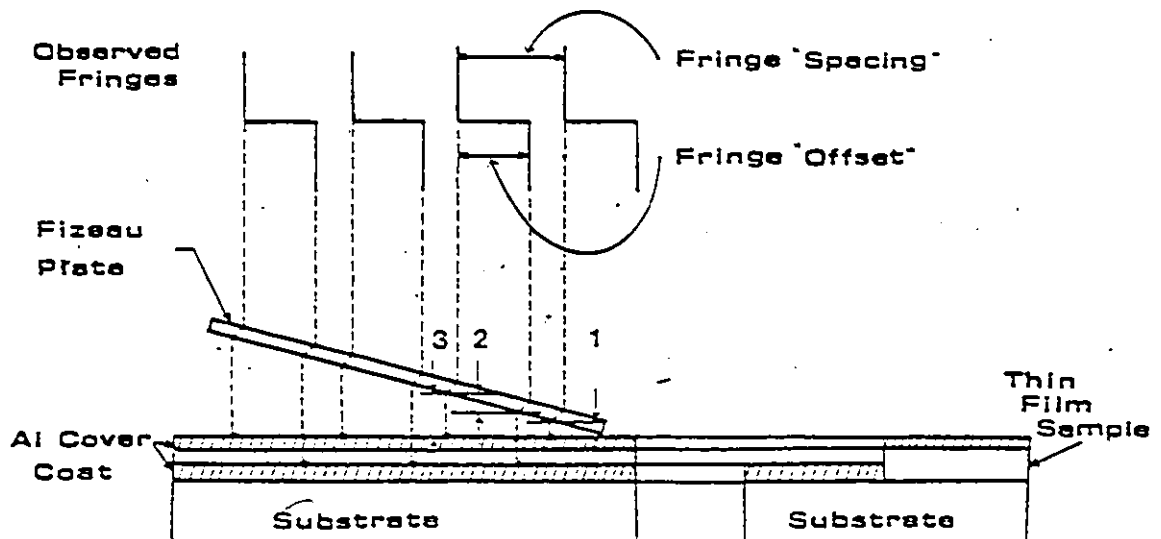
Figure 37   Optical interferometry for thin film thickness measurement.

1: 1/4 WAVELENGTH

2: THIN FILM THICKNESS

3: 3/4 WAVELENGTH
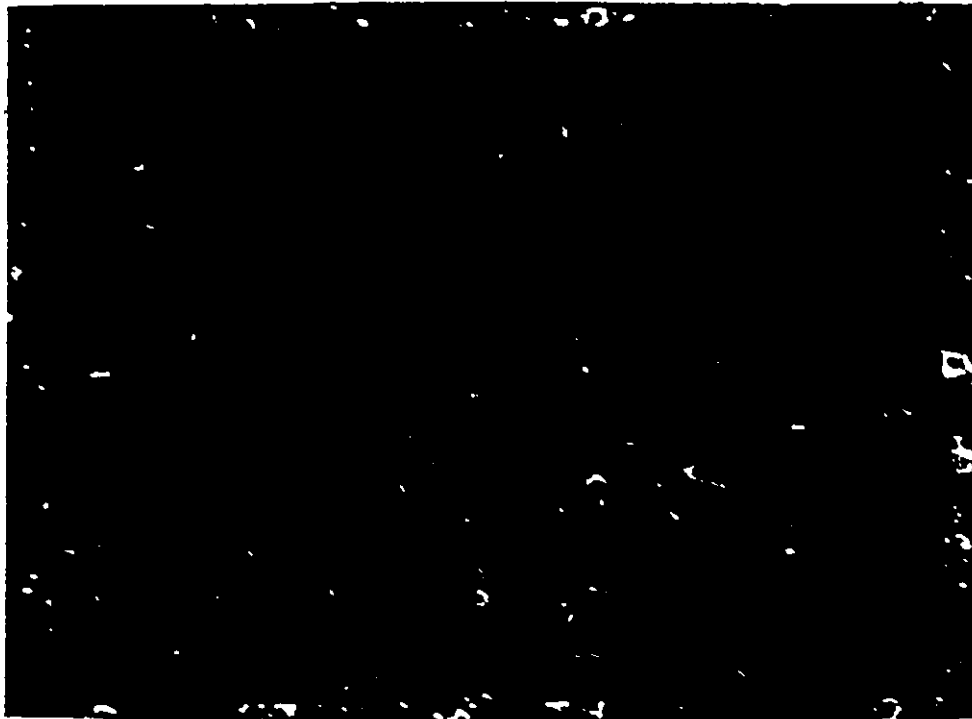
(a)   Mag. ×100

(b)   Mag. × 450

Figure 38   Scanning electron micrographs of BST thin
             film deposited on window glass substrate
             after annealed at 700 °C (Specimen Q5).
             See Tables 7 for preparation conditions of Q5.
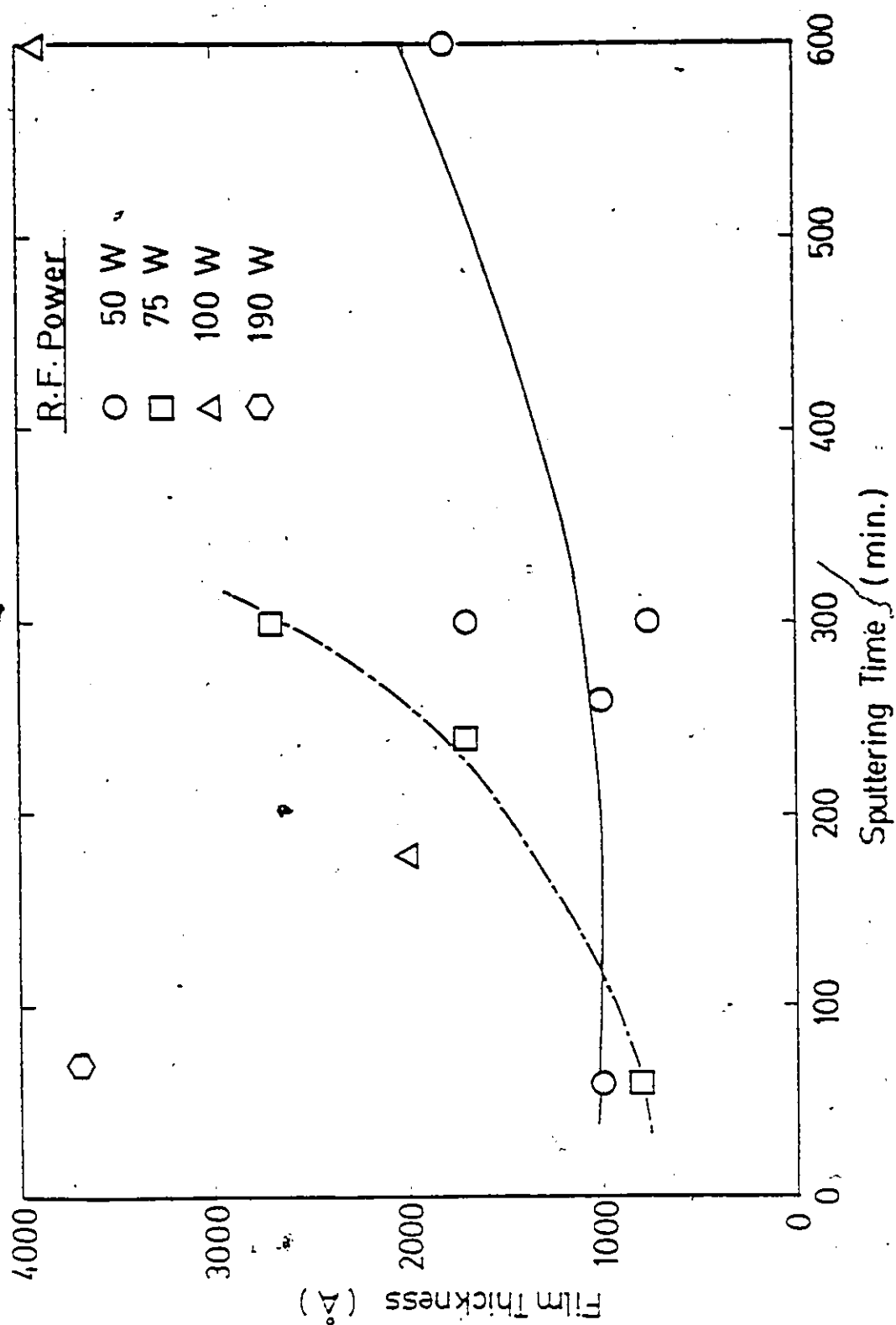
Figure 39   Relation between film thickness and sputtering time for the sputtering deposition system with "Tri-Mag" sputtering source.
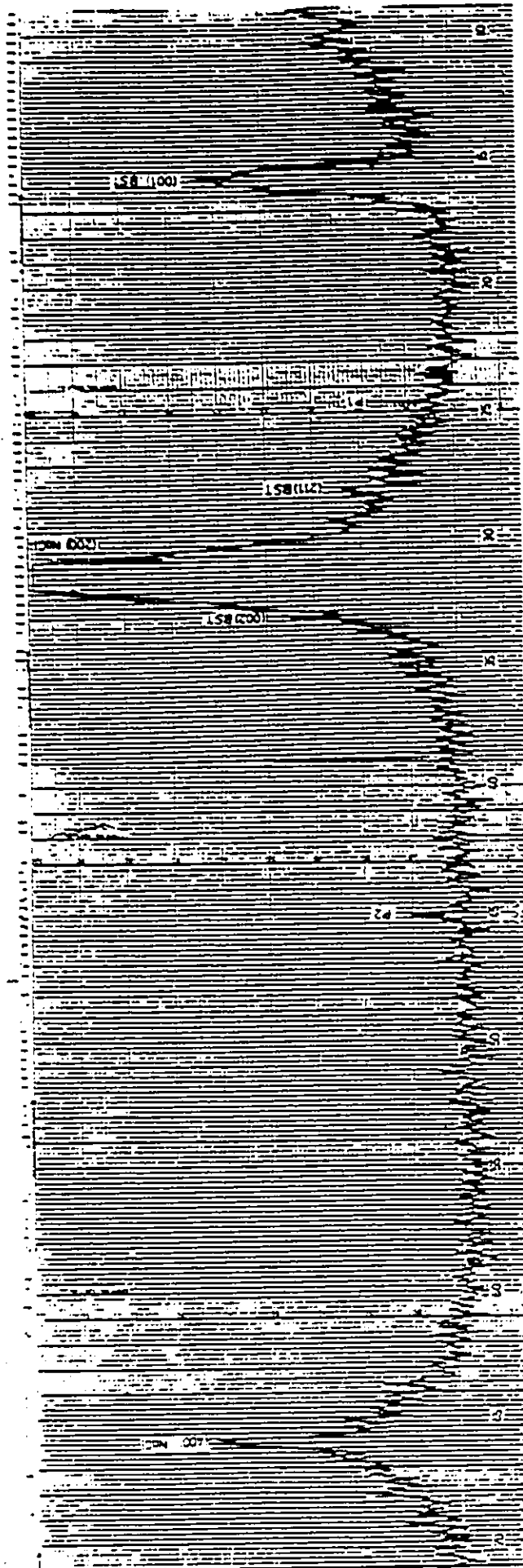
Figure 40   X-ray diffraction pattern for BST thin film fabricated on NaCl single crystal substrate (Specimen W12s).

I(Arbitrary Unit)

(d) Ta=950C°

(c) Ta=800C°

(b) Ta=500C°

(a) Ta=300C°

2θ (°)
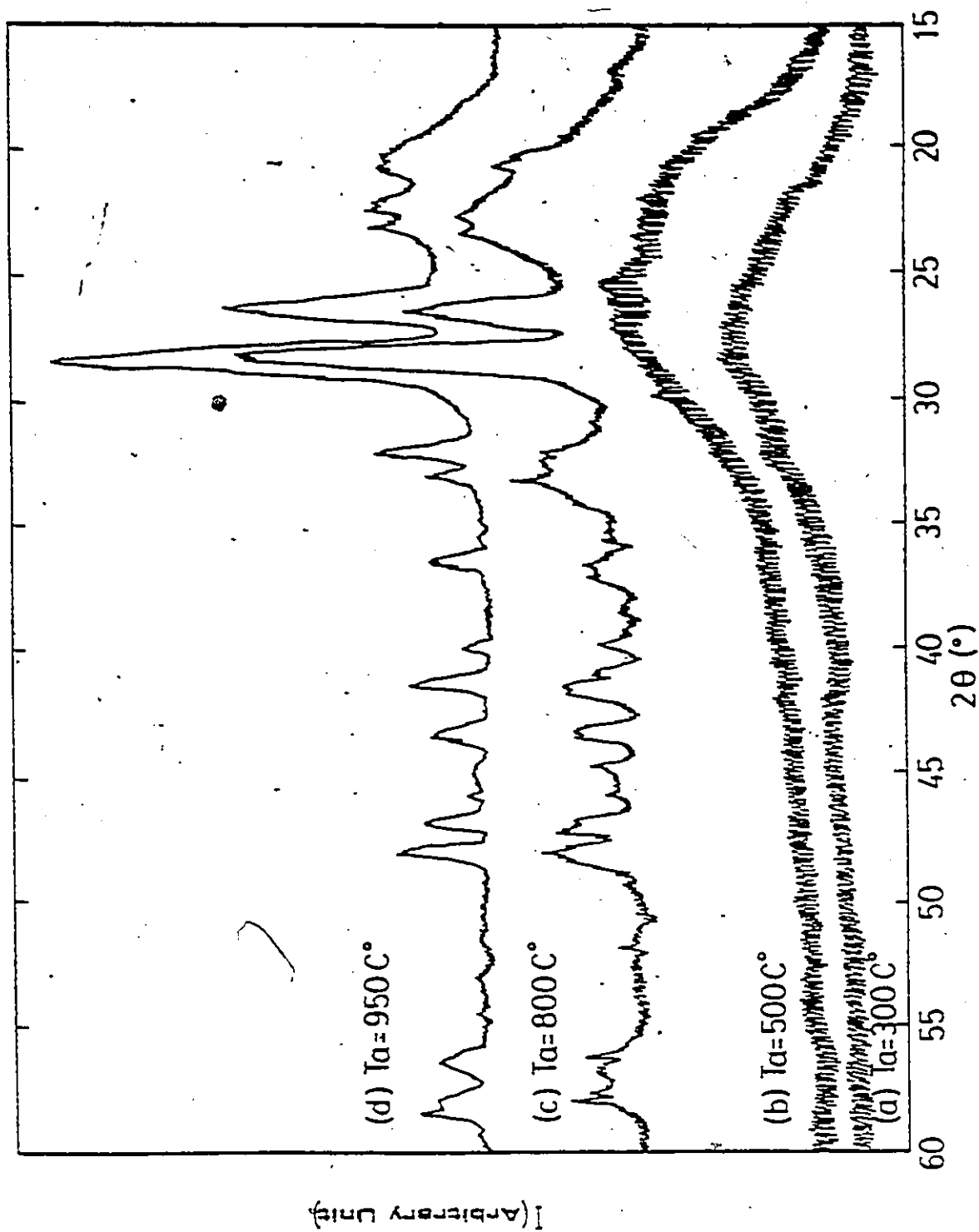
Figure 4.1   Effect of annealing temperature, Ta, on the x-ray diffraction pattern
for a BST thin film sample fabricated on fused quartz substrate.
Amorphous-to-crystalline transition is clearly observed.
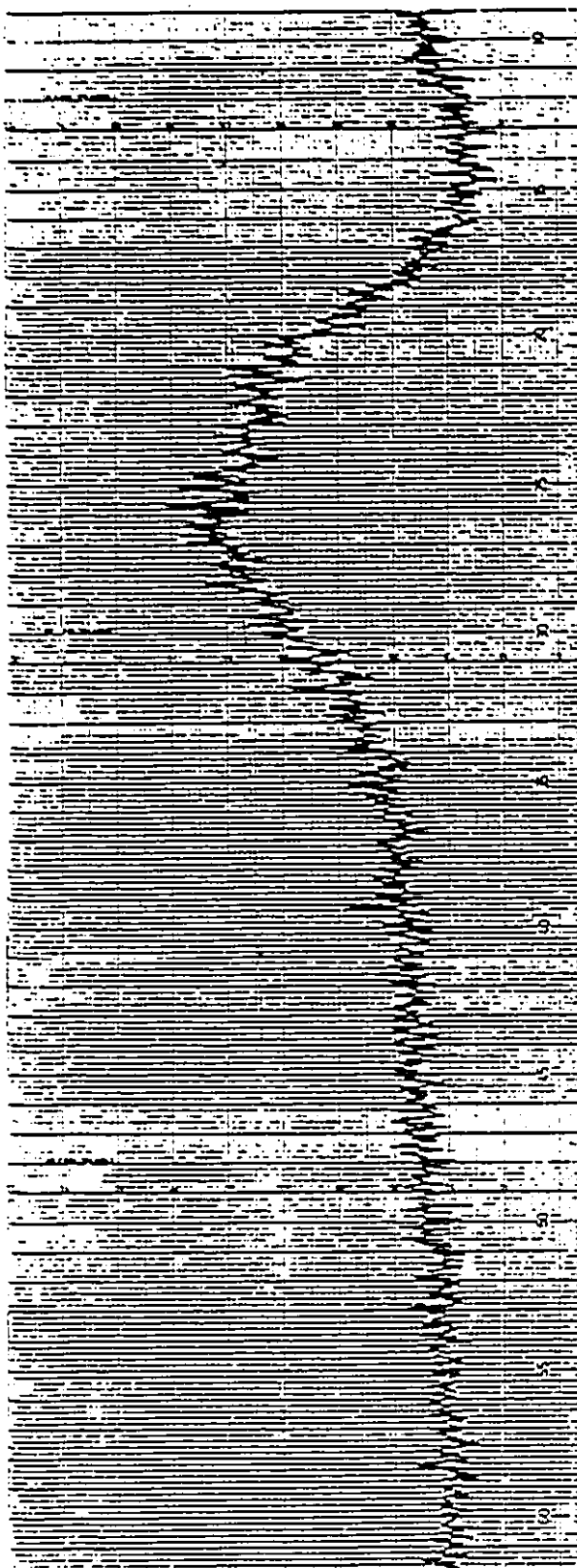
2θ (diffraction angle)

Figure 42 (a) X-ray diffraction pattern for BST thin film fabricated on fused
quartz substrate. Annealed at 500 °C (Specimen W12D).
See Tables 9 and 10 for the specimen preparation conditions.

I (arbitrare unit)

Figure 42 (b)   X-ray diffraction pattern for BST thin film fabricated on fused quartz
substrate.   Annealed at 800 °C (Specimen W12G).
See Tables 9 and 10 for the specimen preparation conditions.

I (arbitrary unit)

2θ (diffraction angle)

Figure 42 (c) X-ray diffraction pattern for BST thin film fabricated on fused quartz substrate. Annealed at 900°C (Specimen W12H).
See Tables 9 and 10 for the specimen preparation conditions.

I (arbitrary unit)
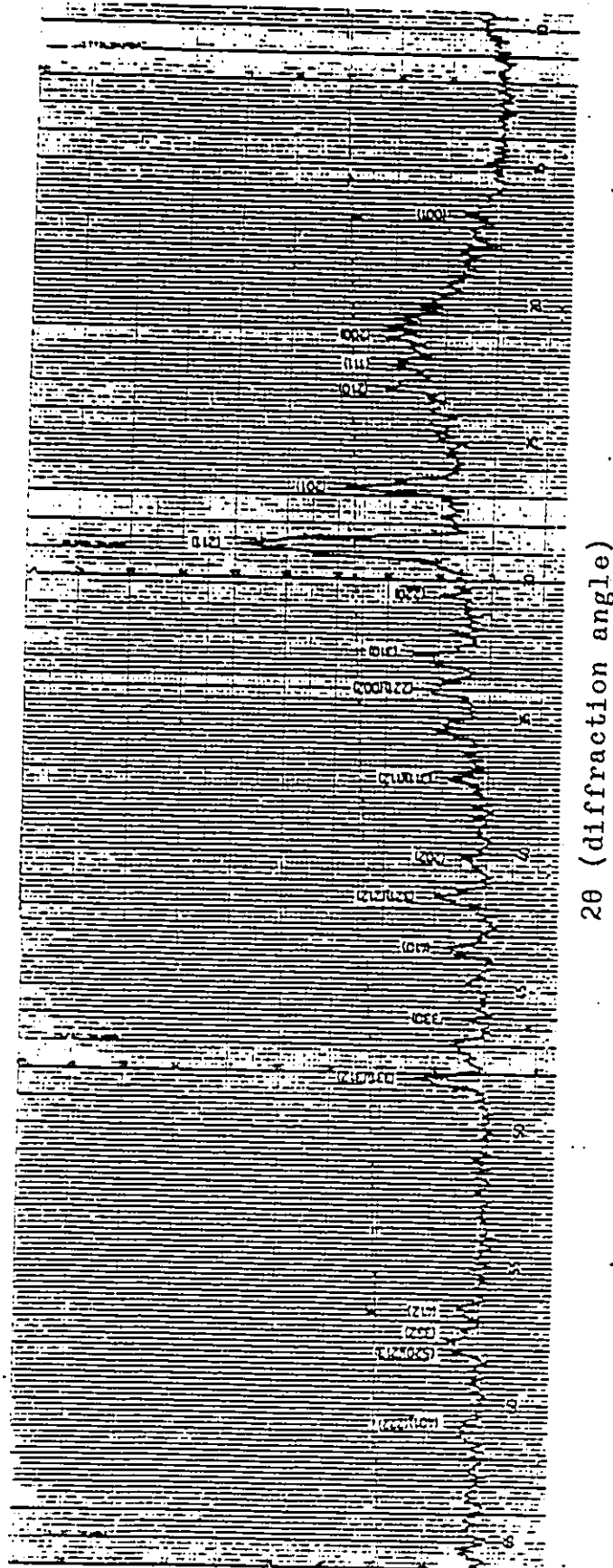
2θ (diffraction angle)

Figure 42 (d) X-ray diffraction pattern for BST thin film fabricated on fused quartz substrate. Annealed at 950 °C (Specimen W12I). See Tables 9 and 10 for the specimen preparation.
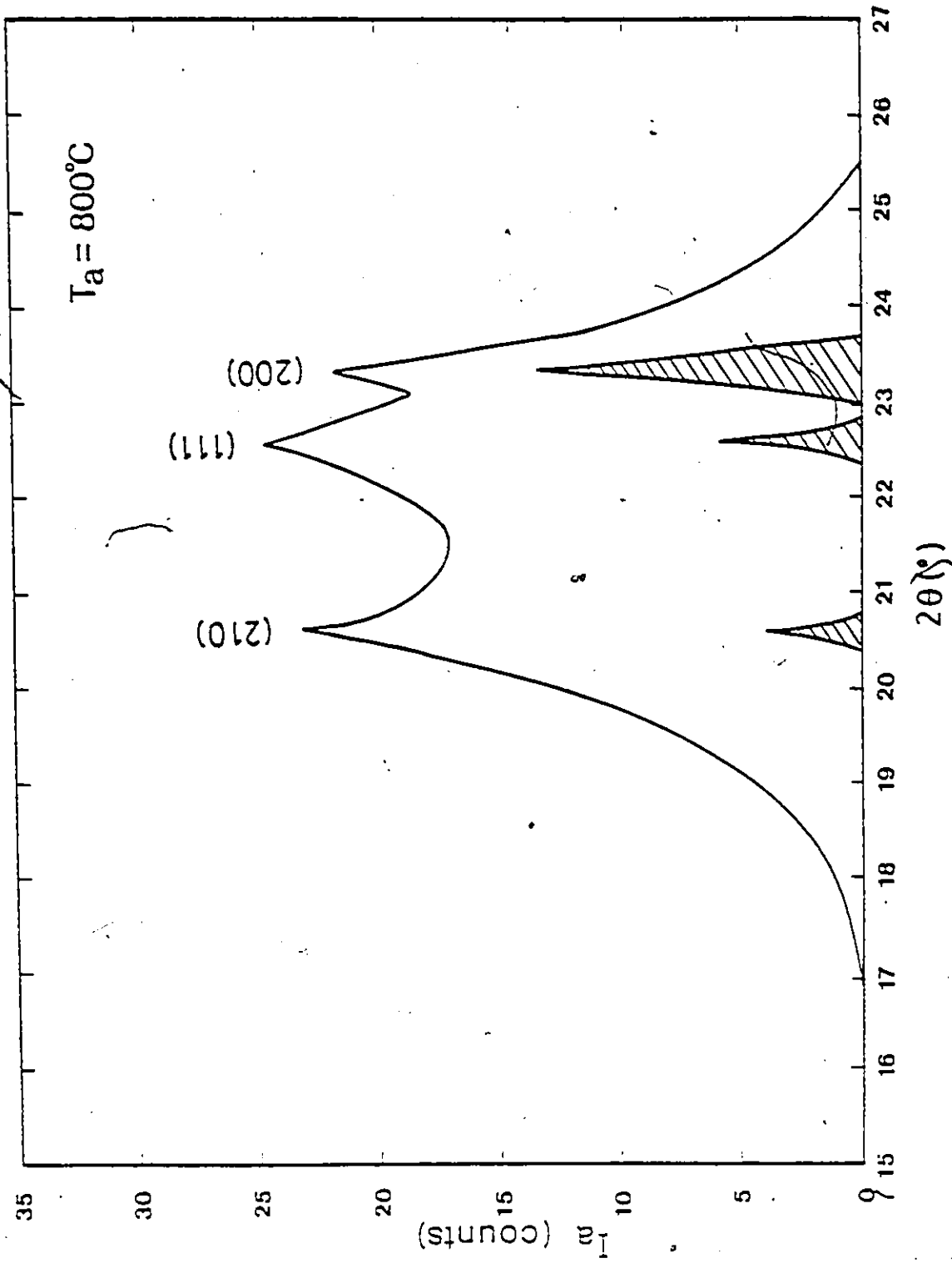
Figure 43   Experimental x-ray diffraction pattern for amorphous+crystalline phases in Specimen W12G annealed at 800°C. Shaded peaks are corresponding 200, 111, and 210 peaks for polycrystalline BST.
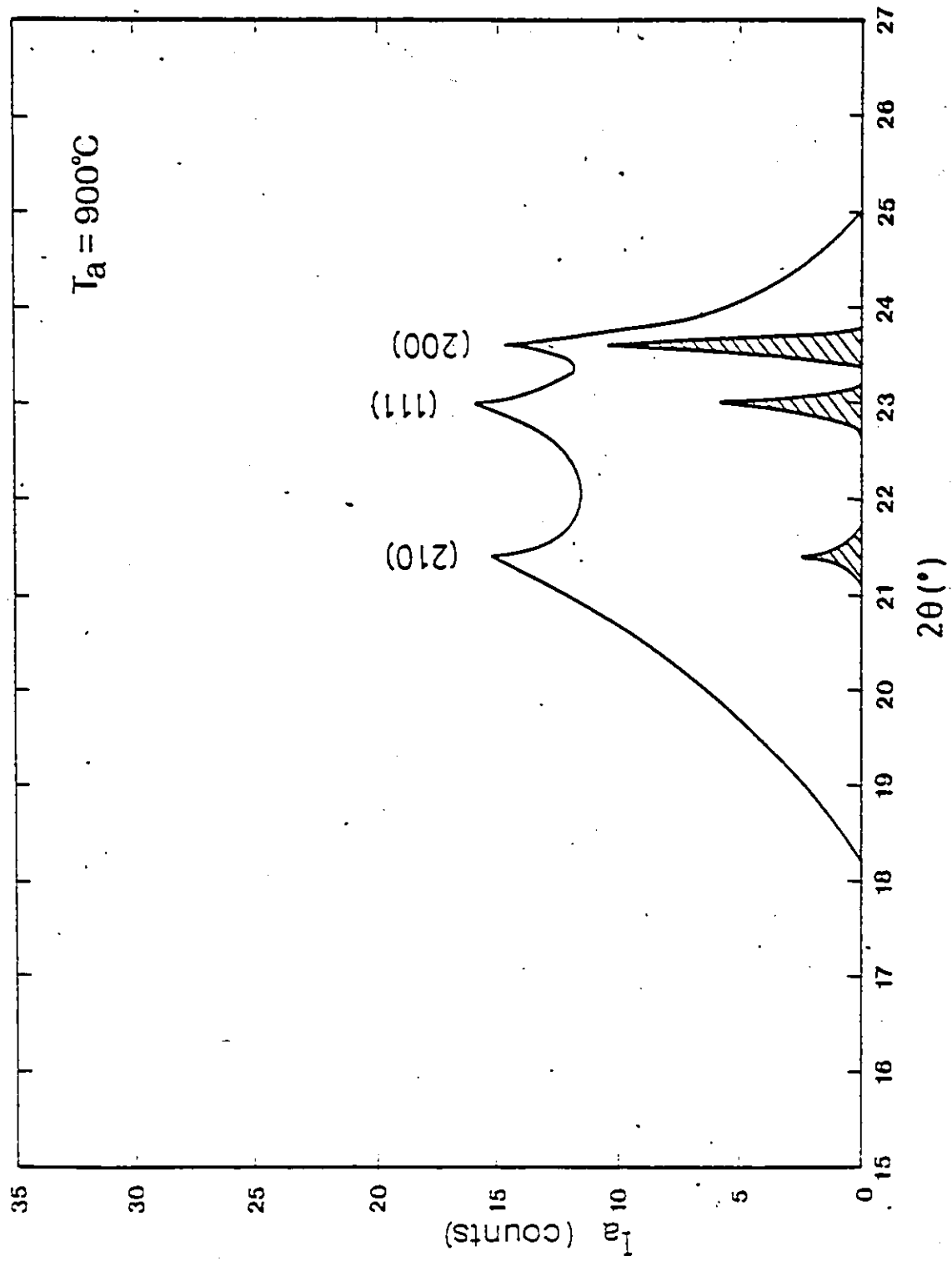
Figure 44   Experimental x-ray diffraction pattern for amorphous + crystalline phases
in Specimen W12H annealed at 900°C. Sheded peaks are corresponding 200,
111, and 210 peaks for poly-crystalline BST.
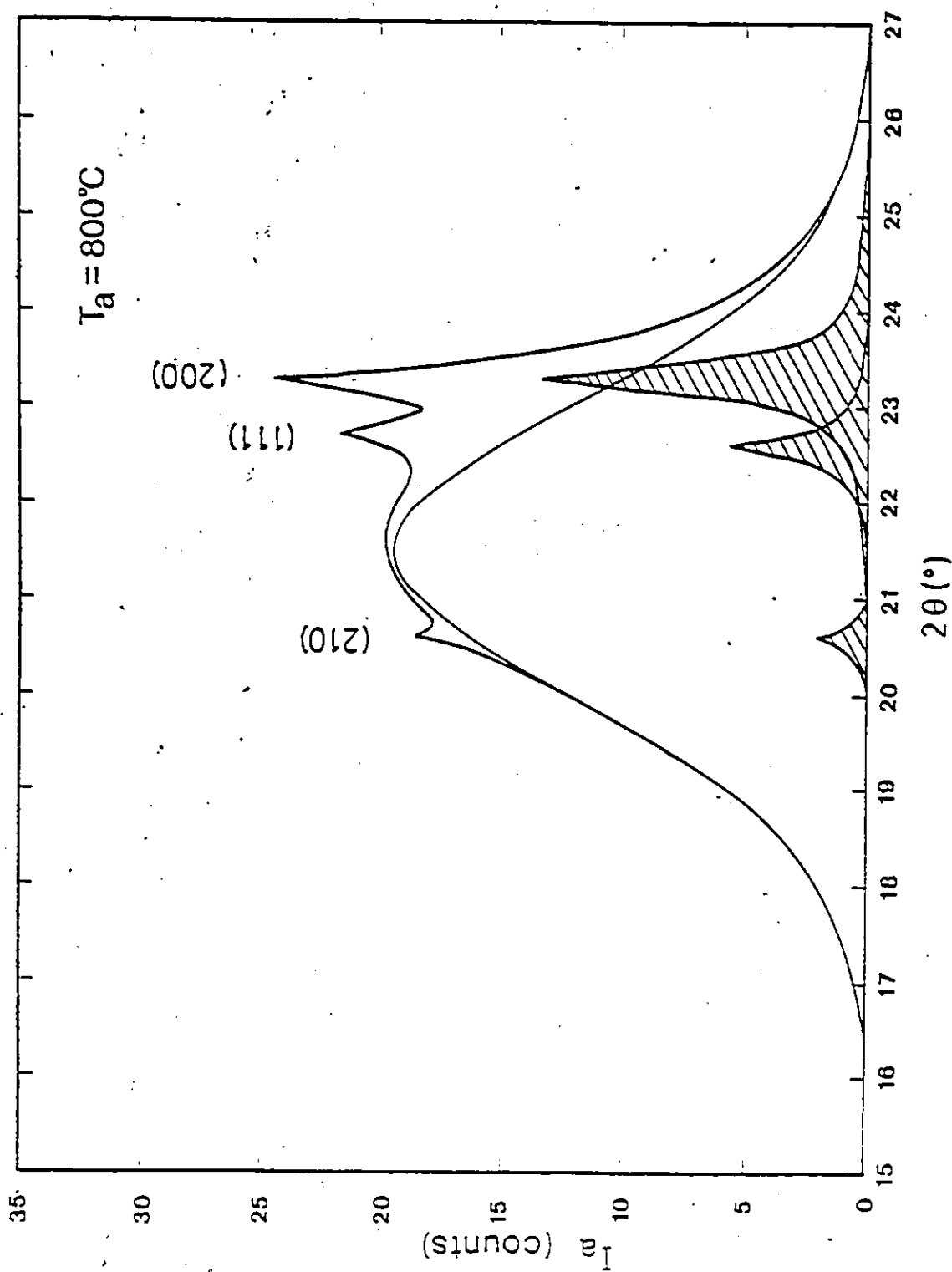
Figure 45   Theoretical x-ray diffraction pattern for amorphous + crystalline phases
in Specimen W12G annealed at 800 °C. Shaded peaks repesents Lorentzian
peaks for crystalline portion and the broad peak is a Gaussian peak for
amorphous portion.

Figure 46   Theoretical x-ray diffraction pattern for amorphous + crystalline phases in Specimen W12II annealed at 900°C.   Sheded peaks represents Lorentzian peaks for crystalline portion and the broad peak is a Gaussian peak for amorphous portion.
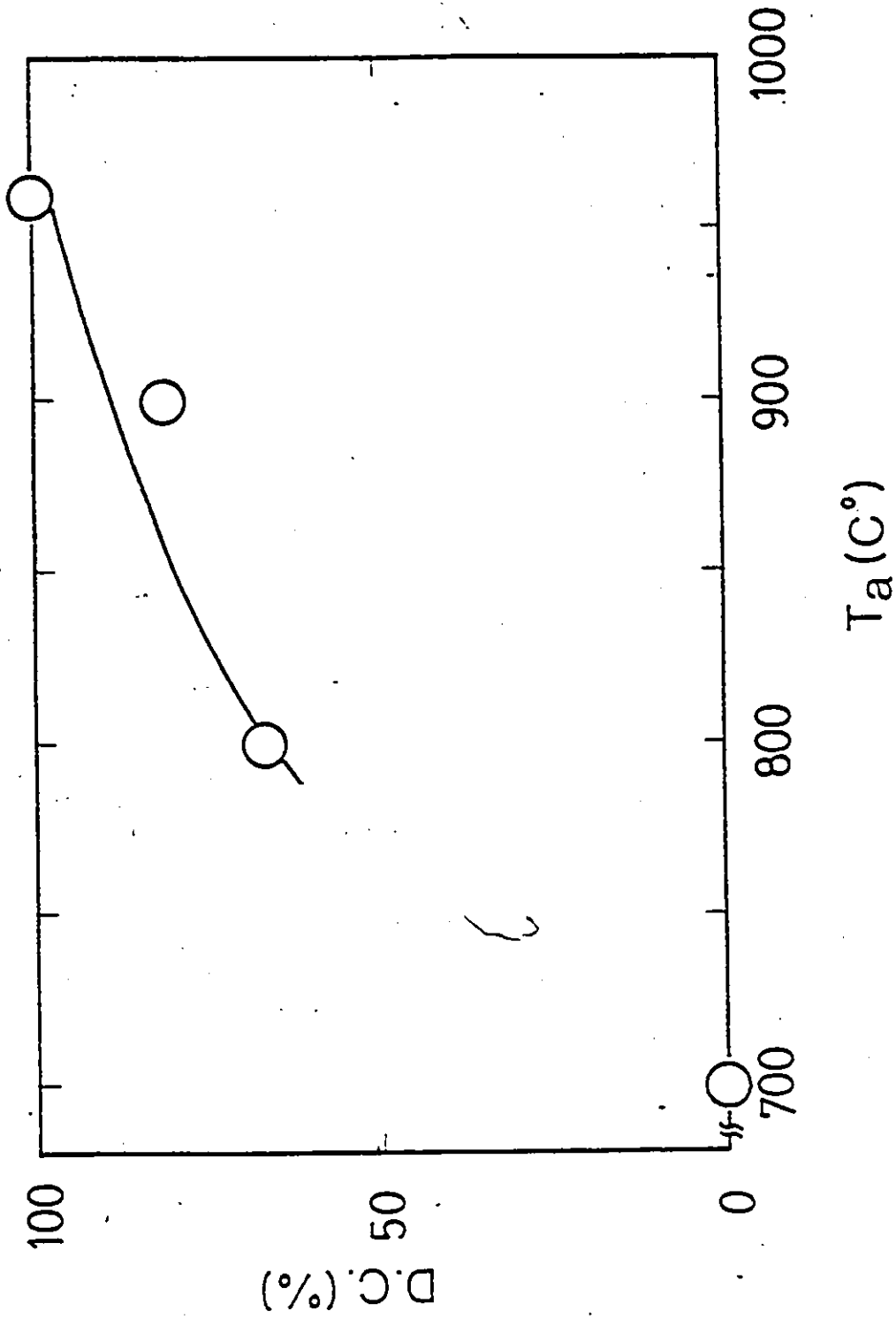
Figure 47 Degree of crystallinity (D.C.) in the annealed BST thin film with respect to annealing temperature, Ta.
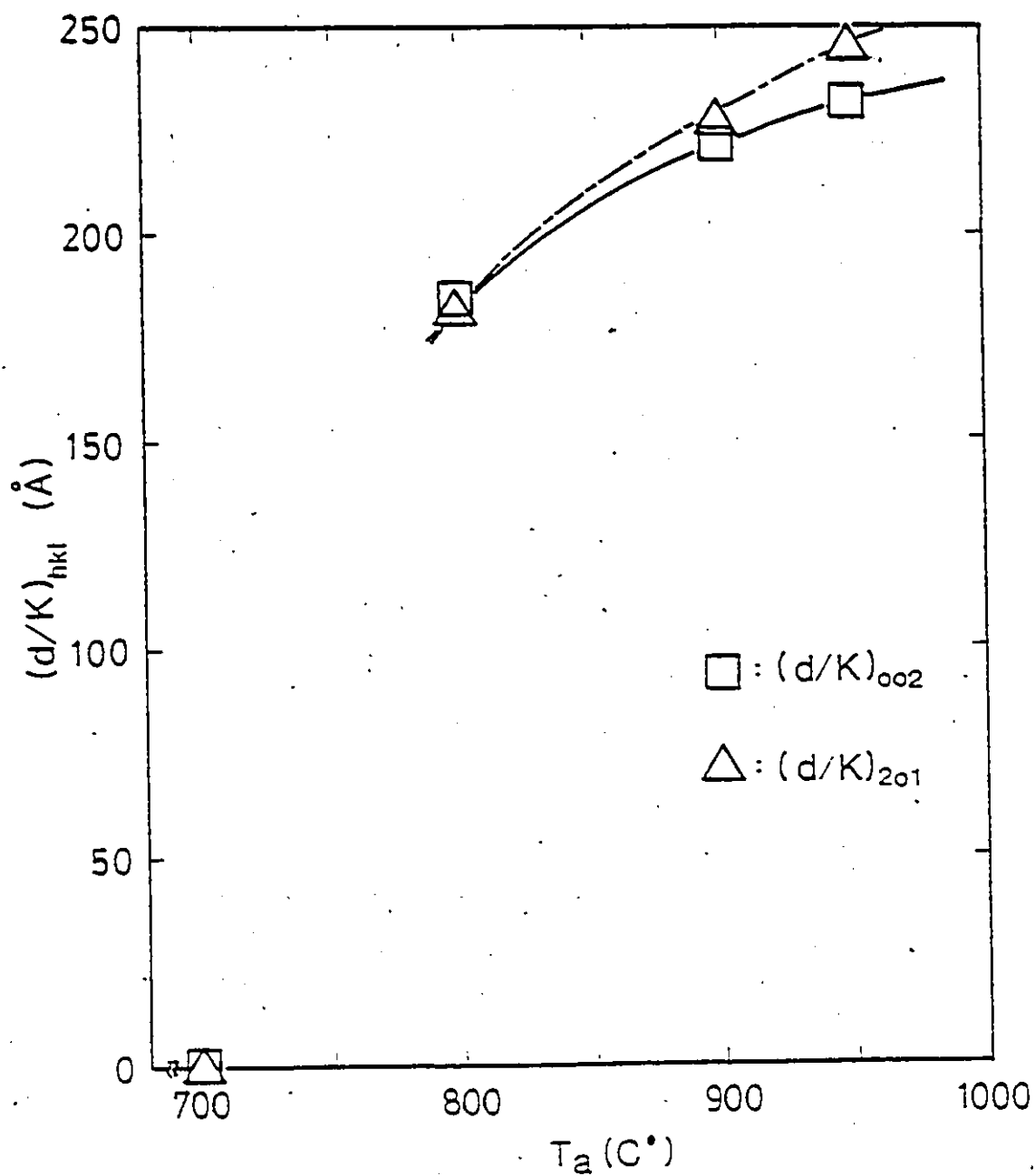
Figure 48   Average grain size, d, normalized by shape factor K, vs annealing temperature, Ta, using 002 and 201 diffraction peaks.
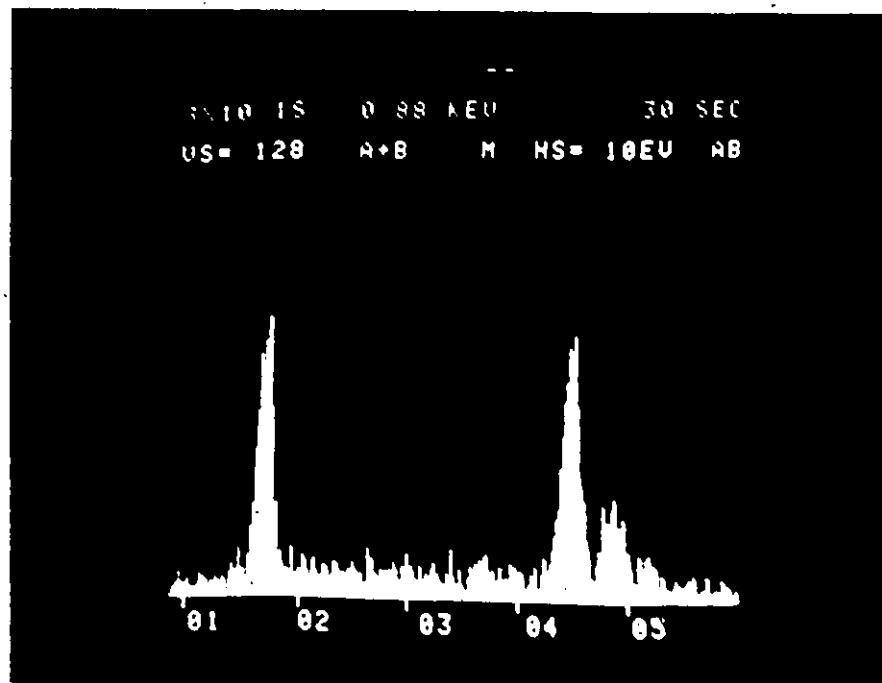
(a)
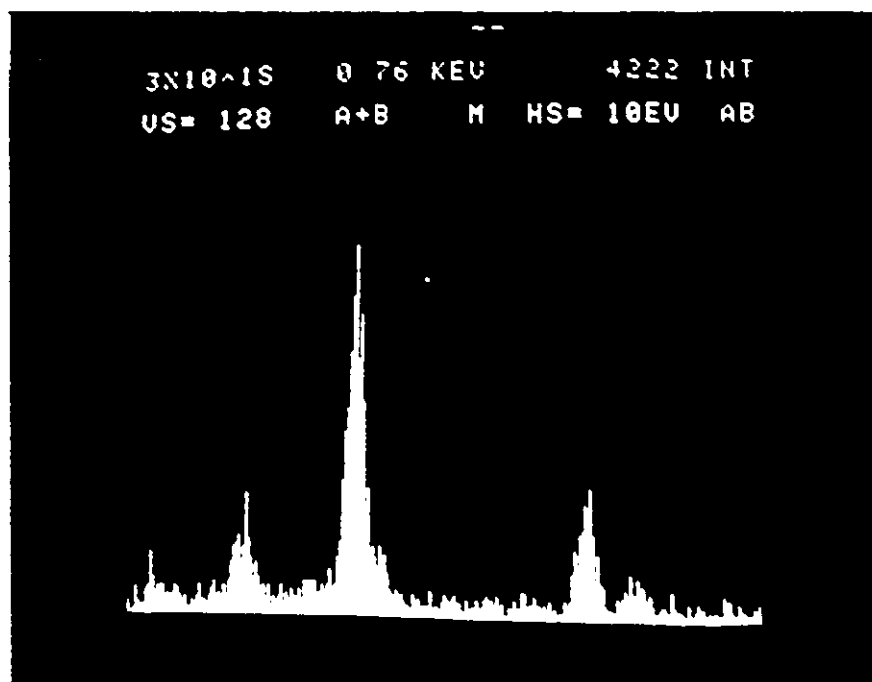
(b)

Figure 49   Energy dispersion spectra using kevex

       (a) for BST thin film deposited on fused
           quartz substrate (Specimen W12q), and

       (b) for BST thin film deposited on NaCl
           single crystal substrate (SpecimenW12s).

Figure 50 Scanning electron micrograph of BST thin film
deposited on NaCl single crystal substrate.
(Specimen W12s). See Table 9 for the specimen
preparation conditions.

(a)

(b)

Figure 51   Scanning electron micrographs of BST thin film
             deposited on fused quartz substrate   annealed
             at 900 °C (Specimen W12E). SeeTables 9 and 10
             for the specimen preparation conditions.
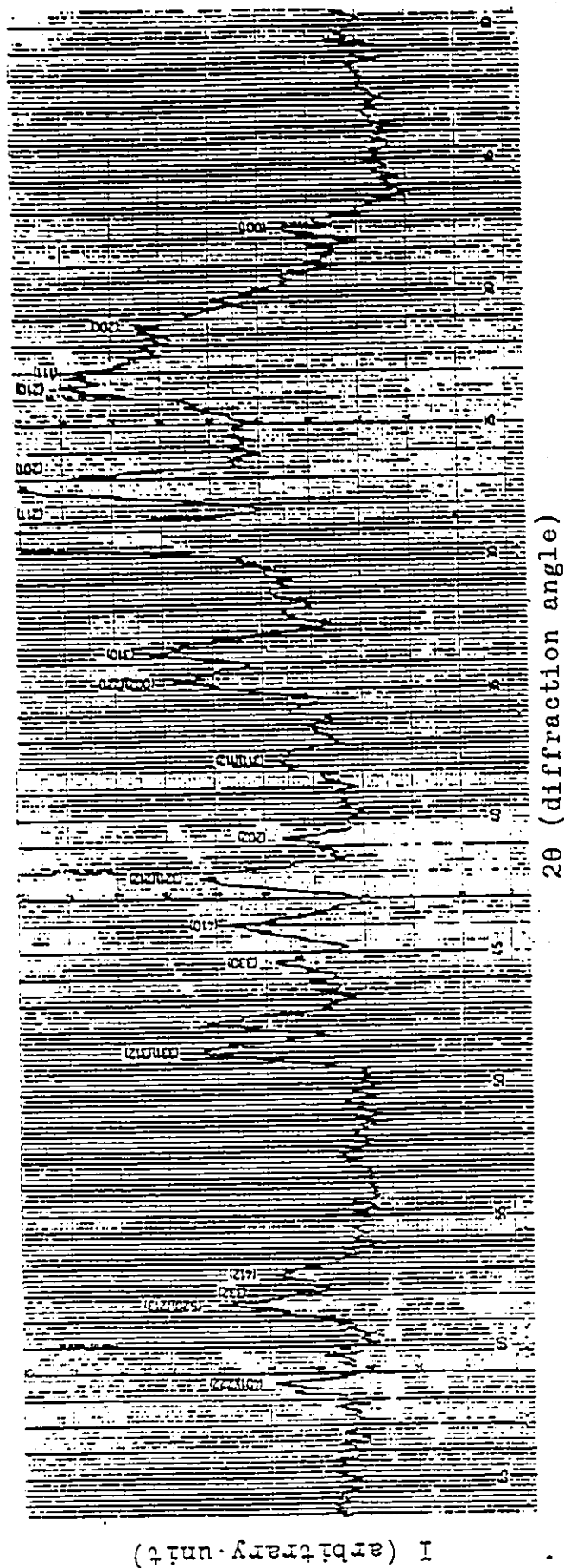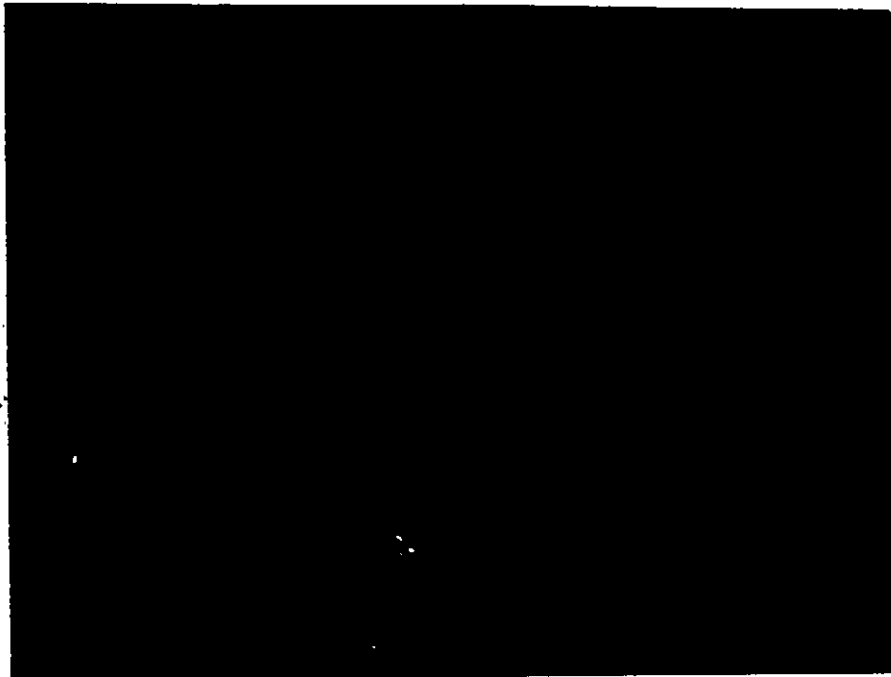
(a)   Mag. ×200
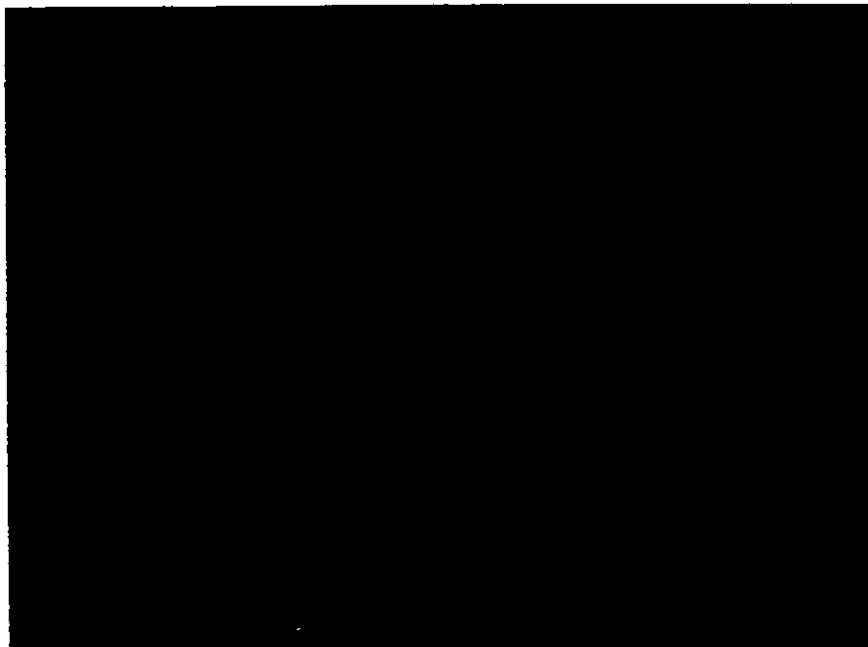
(b)   Mag. ×1,000

Figure 52 Scanning electron micrographs of BST thin film
deposited on fused quartz substrate annealed at
950 °C. (Specimen W12I) See Tables 9 and 10 for
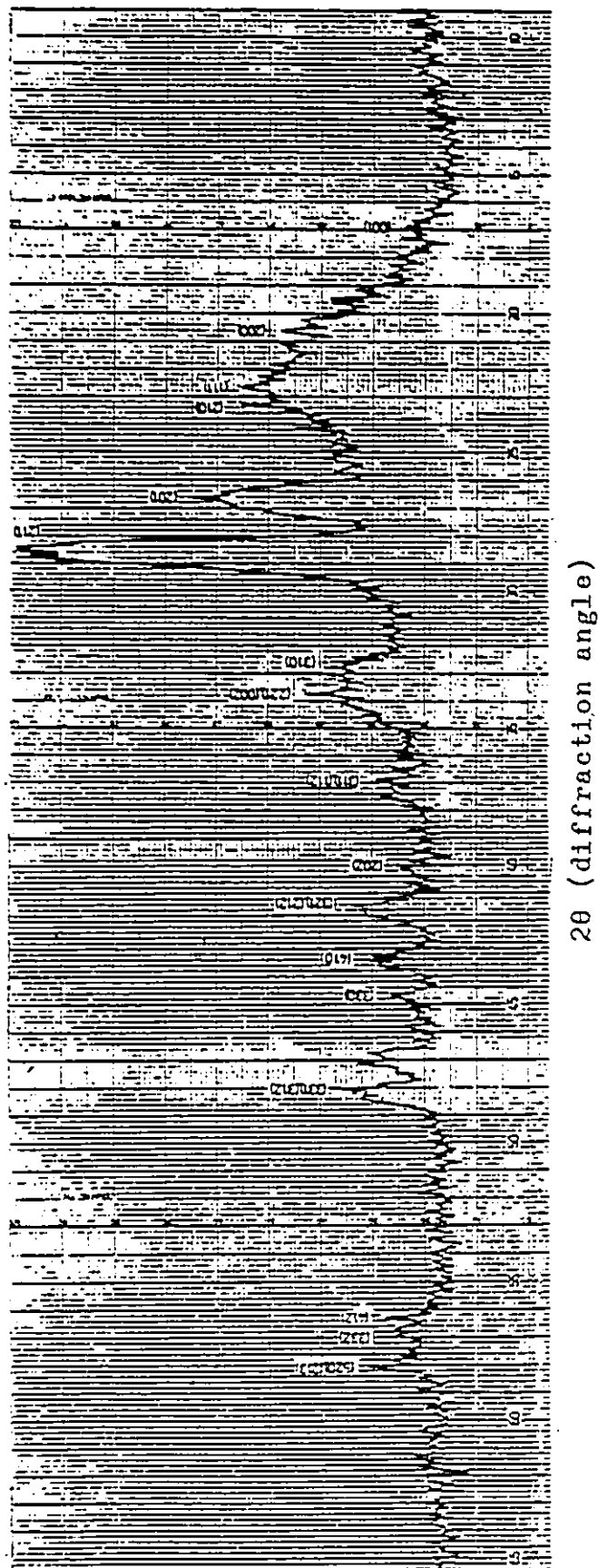the specimen fabrication conditions.

(a)

(b)

Figure 53 Scanning electron micrographs of BST thin film
deposited on window glass substrate annealed
at 500 °C (a) and 550 °C (b).

(c)

Figure 53   Scanning electron micrograph of BST thin film
            deposited on window glass substrate annealed
            at 700 °C.
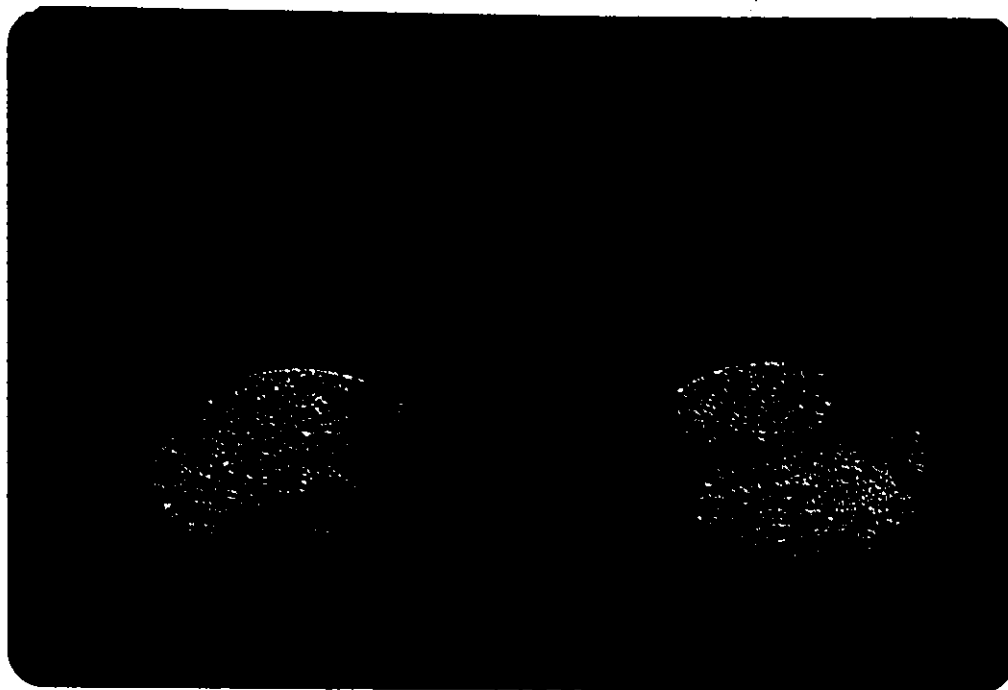
Figure 54   Sintered BST sputtering targets before (left)
and after (right) puttering deposition.
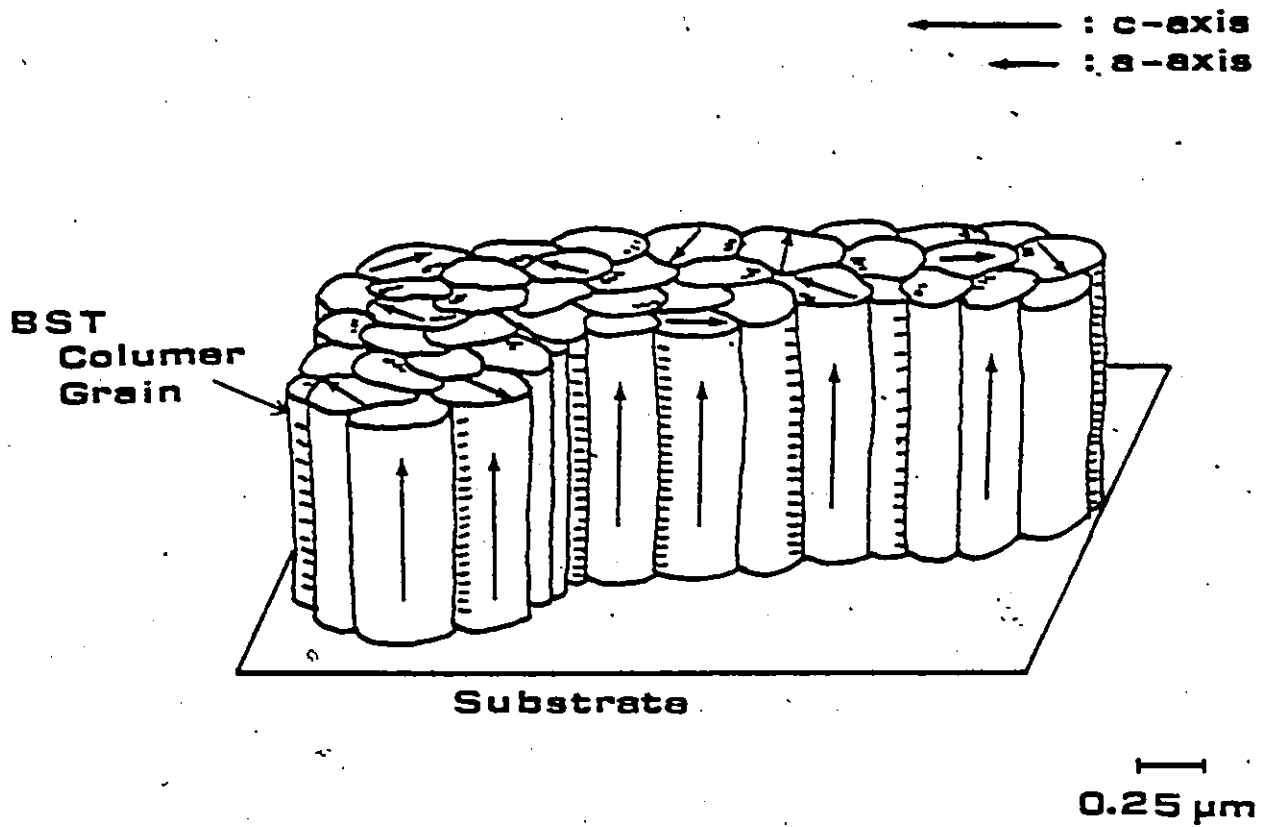
Figure 55 Schematic illustration of c-axis columer grain
oriented $Ba_2Si_2TiO_8$ thin film structure.

(Key to notation)

s=elastic compliances

d=piezoelectric moduli (a)

α=thermal expansion
coefficients

k=permittivities

p=pyroelectric
coefficients

C=heat capacity

T=absolute temperature

*t is a notation of (b)
transpose matrix

class
4mm

Components:

● : zero

● : nonzero

●—● : equal

x : $2(s_{11}-s_{12})$

(c)

class
6mm

Figure 56 Matrixs for point group 4mm (b) and 6mm (c). Ref.(34).

APPENDIXES

APPENDIX A

Operation Procedure of Sputtering Deposition System

A detailed description of the operation procedure of the sputtering system (cf. Sec. 4.4) is given.

A.1 Start-Up Procedure

A.1.1 From Complete Shutdown

a) Close the 'Control Power' breaker.

b) Close the high vacuum valve. Make sure the valve position is horizontal.

c) Select 'Backing' on the combined Backing/Roughing (BRV) valve.

d) Turn on the water supply to the diffusion pump by fully opening the water valve.

e) Switch on the backing pump.

f) When the backing pressure reaches 400 m Torr or less, turn on the diffusion pump.

g) Fill the Liquid Nitrogen reservoir.

h) The diffusion pump must warm up to operating temperature.

A.2 Preparation for Sputtering

A.2.1 Hoist Operation

To raise the chamber lid, first make sure that the high vacuum valve is closed, the BRV is at 'Backing' position and the chamber vent valve is open. Press the appropriate pushbutton. The lid may be swung away from the chamber by pulling the release ring at the back of the

hoist head and pushing the lid.

To close the lid, rotate the lid back to engage the release ring and press the appropriate pushbutton. As the lid nears the chamber carefully guide it into the locating dowels in the top of the chamber.

A.2.2 Substrate Loading

a) Always make sure the circuit breaker is off when working inside the chamber.

b) Adjust the height of the substrate holder to the desired position.

c) Install the desired target into the source which will be powered.

d) Close the lid.

A.2.3 Chamber Evacuation

a) Close the chamber vent valve and fully open the throttle valve. Make sure that the 'pump ready' light is on.

b) Select 'Roughing' on the BRV valve to rough down the chamber.

c) When a system pressure of 200 m Torr or better is reached, select 'Backing' on the BRV valve.

d) Open the high vacuum valve slowly to avoid stalling the diffusion pump.

e) Evacuate the chamber to 10^{-6} Torr or less.

A.3 Sputtering Procedure

A.3.1 Throttle Valve Operation

Repeatable diffusion pump throttling can be achieved

with the micrometer stop. The valve can be fully opened or closed to the present condition by pressing the appropriate pushbutton.

A.3.2 Chamber Cooling

If desired, open appropriate water valve for chamber cooling.

A.3.3 Sputtering Procedures

A.3.3.1 Start-Up

a) Fully open the water valve for target sources. Make sure 'Low Water' light is off.

b) Select the appropriate argon valve and turn it counter-clockwise to open it.

c) Set Electron Emitter current, Plasma current knob to zero.

d) Turn on the 208V circuit breakers.

e) Turn on the PD/20 power supply by pressing the rocker switch upwards.

f) After 10-15 seconds start turning the electron emitter current knob until the plasma ignites as indicated by a plasma reading of about amperes.

g) Adjust the electron Emitter Current knob clock-wise; the plasma voltage drops from an open circuit voltage of about 85 volts to a reading of approximately 45 volts on the meter.

h) Slowly increase the Plasma Current while also adjusting the Electron Emitter Current to maintain the plasma voltage at about 45 volts.

i) If desired, open the oxygen valve.

j) Switch on the R.F. generator power supply circuit breaker and wait until blue R.F. indicator is on.

k) Press the R.F. on pushbutton.

l) Set the Multimeter function switch to the V3Ig position.

m) Turn the power control knob clockwise until the desired power is indicated on the Incident power meter.

n) Set the substrate position.

o) When ready for sputtering, open the shutter to allow the target atoms to reach the substrate.

p) When finished sputtering, shut the shutter.

A.3.3.2 Shutdown

a) Rotate the R.F. Power control knob fully counter-clockwise and switch off the generator circuit breaker.

b) Turn off the Electron Emitter Current and press the power rocker switch downwards.

c) Switch off the main 208V.

d) Turn off the water valve for target source.

e) Close the high vacuum valve and check that the BRV valve is in the 'Backing' mode.

f) Open the air admittance valve.

A.3.4 Complete Shutdown Procedure

a) Close the high vacuum valve and vent the chamber as above.

b) Shut off the diffusion pump and allow it to cool, about 30 minutes.

c)   Switch the BRV valve to the central position and
quickly turn off the mechanical pump.   The backing line will
automatically vent.

d)   Close off all water and gas valves and shut off
the control power at the panel.

APPENDIX B

Diffraction Angle Dependence of Absorption Factor, a

If an x-ray intensity I_o passes through a distance, x, in a material with linear absorption coefficient, μ, its intensity, I_x can be written as:

$$I_x = I_o e^{-\mu x} \qquad (1)$$

The distance x can be calculated from Bragg's law (See Figure B.1).

$$x = 2t/\sin\theta \qquad (2)$$

where t is the thickness of the surface coating film and θ is the diffraction angle. The absorption factor defined in Equation (3) in Appendix B is:

$$a = I_x/I_o \qquad (3)$$

Substituting Eq. (2) into Eq. (1), the absorption factor is obtained as:

$$a = \exp\{-\mu(2t/\sin\theta)\} \qquad (4)$$

Thus, in general, a depends on θ. In order to demonstrate the 2θ dependence of a, using Eq. (4), the linear absorption coefficient of $Ba_2Si_2TiO_8$, μ_{B57}, is required. Since μ_{BST} has not been measured, it is approximated by:

$$\frac{\mu_{BST}}{\rho_{BST}} = (2\frac{\mu_{Ba}}{\rho_{Ba}} + 2\frac{\mu_{Si}}{\rho_{Si}} + \frac{\mu_{Ti}}{\rho_{Ti}} + 8\frac{\mu_O}{\rho_O})/13$$

mass absorption factors (μ/ρ) for Ba, Si, Ti and O used for this calculation were 359, 60.3, 204, and 12.7 cm^2/g, respec-

fully (53). Density ρ_{BST} for thin film is not available, and is approximated by the BST single crystal density, 4.43 g/cm³. The film thickness was 3900Å in the calculation. Results are plotted in Figure B.2. The calculated a is almost constant except at very low diffraction angles ($2\theta < 10^{\circ}$). Thus the assumption of a constant-absorption factor, a is valid for intensities at diffraction angles larger than ~10°.
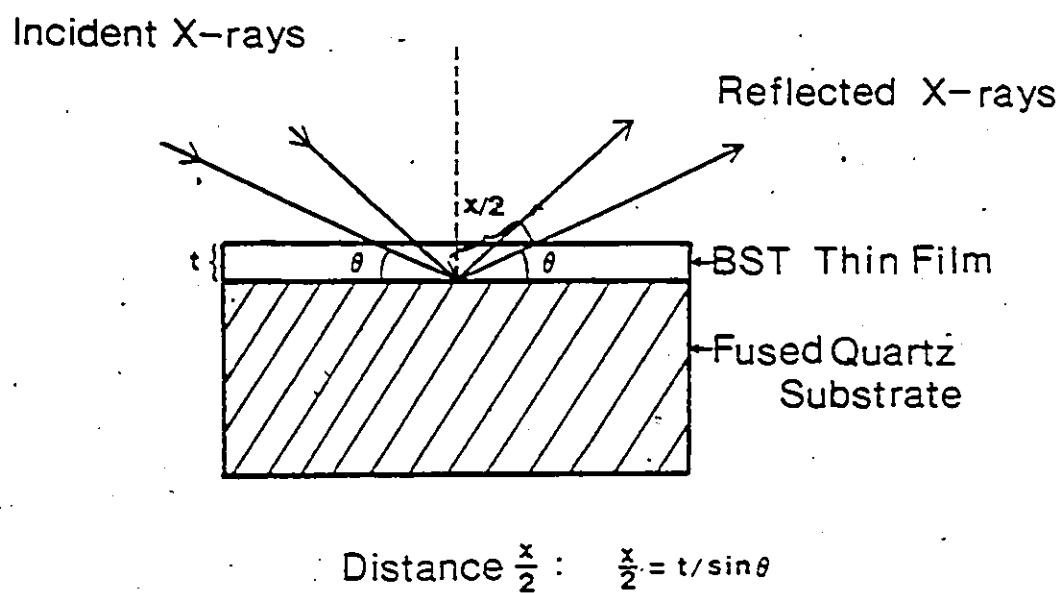
Figure B.1   X-ray beam absorption behaveir in thin film.
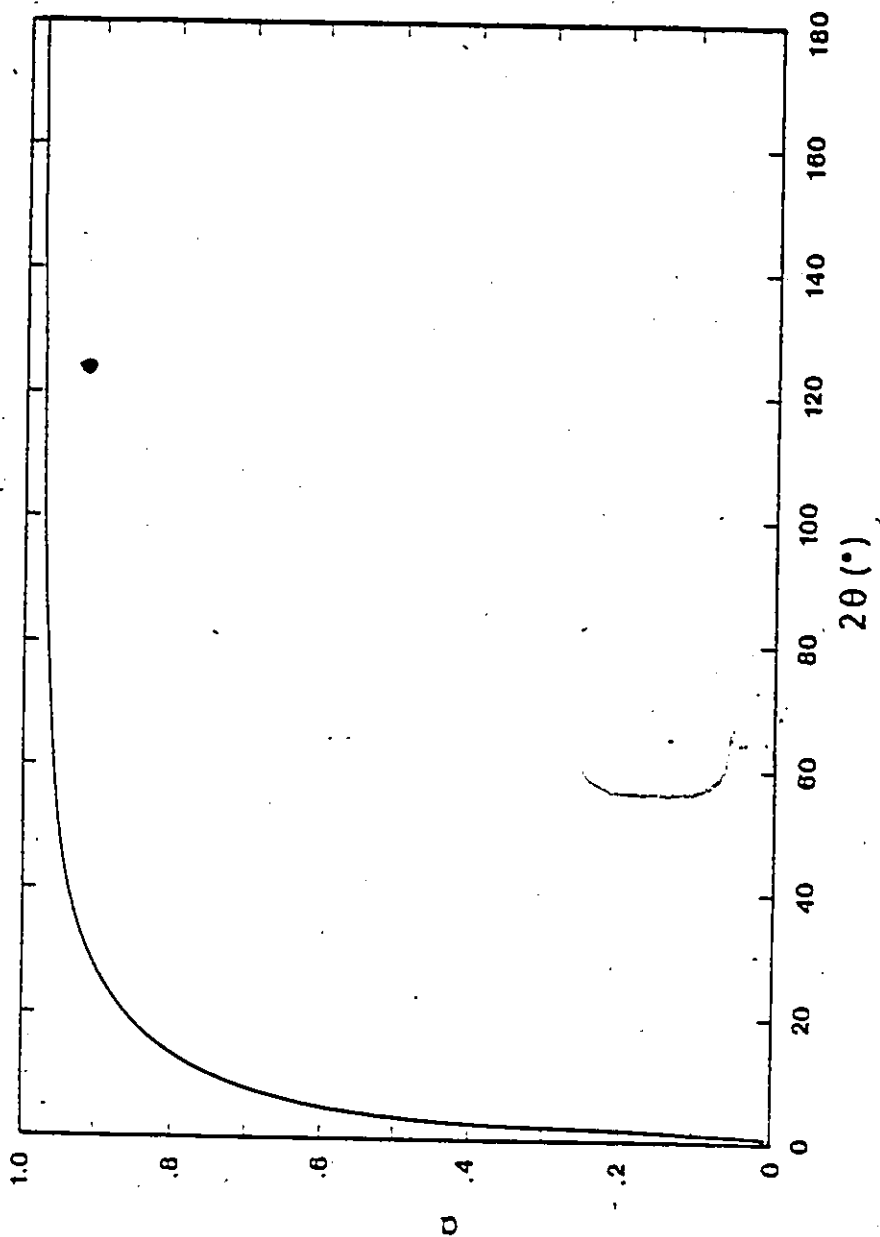
Figure B.2 X-ray absorption factor, a, vs 2θ (diffraction angle) for Specimen W12q.

APPENDIX C

Calculation of Absorption Factor

In order to evaluate the degree of crystallinity, (D.C.) absorption factor, a, was determined for specimens W12D, W12G, W12H and W12I by the following method. As it is mentioned in the text (Section 3.8.4), the total intensity at different angle 2θ, $I_t(2\theta)$ from a specimen with BST film fabricated on fused quartz substrate can be expressed as:

$$I_t(2\theta) = I_f(2\theta) + aI_s(2\theta) \quad (1)$$

where $I_f(2\theta)$ and $I_s(2\theta)$ are intensities from BST film and fused quartz (when no film is formed), respectively, and a is the attenuation or absorption factor of I_s by the BST film. If an x-ray of intensity I_o passes through a distance, x, in a material with a linear absorption coefficient, μ, its intensity, I_x, is given by:

$$I_x = I_o e^{-\mu x} \quad (2)$$

If the distance x can be taken as a constant for a uniform film thickness in the present case, the above expression can be expressed as:

$$I_x = aI_o \quad (3)$$

As discussed in Appendix B, the assumption of constant a is valid for 2θ between $30°$ and $180°$. It is now assumed that the ratio of peak intensities from the BST film at two different diffraction angles 2θ and $2\theta'$ is identical with that of corresponding peaks from BST ceramic disk as long as

168

2θ and $2\theta'$ are larger than ~60° where the contribution from amorphous diffraction is negligible.

$$\left(\frac{I_T(2\theta)}{I_T(2\theta')}\right)_{\substack{BST \\ Ceramic}} = \left(\frac{I_f(2\theta)}{I_f(2\theta')}\right)_{\substack{BST \\ Film}} = \frac{I_t(2\theta)-aI_s(2\theta)}{I_t(2\theta')-aI_s(2\theta')} \quad (4)$$

For various combinations of peaks at high diffraction angles, the absorption factor was determined. In the Table B.1, listed are the operating conditions of x-ray diffractometer employed for measuring $I(2\theta)$ vs. 2θ for the film specimen, I_t, the BST ceramic disk, I_T, and the fused quartz, I_s.

Detailed data for I_T and I_s are given in Table B.2 and B.3. Absorption factors a were calculated for specimens annealed at 500, 800, 900 and 950°C to be 0.65, 0.62, 0.67 and 0.65, respectively. Data for I_t, I_s and calculated I_f are listed in Tables (C.4)-(C.7).

Table C.1

Operating Conditions of X-ray Diffractometer

Radiation Tube	CuK
Operating Voltage	40 kV
Operating Current	20 mA
Full Scale of Intensity	200 cps for Disk Target W12D W12G
	100 cps for W12H
	400 cps for W12I
Scanning Rate	$2°/min.$ in 2θ

Table C.2

X-Ray Diffraction Data of Fresnoite Ceramic Disk
(cf. Specimen T1 in Table

Peak	$2\theta(°)$	Index	Intensity, I_t*
1	17.5	001	5.3
2	21.5	200	3.0
3	23.0	111	7.3
4	23.8	210	14.2
5	27.5	201	30.0
6	29.5	211	61.3
7	33.7	310	19.1
8	34.8	221,002	28.0
9	38.0	311,112	9.1
10	38.5	202	6.9
11	43.5	321,212	19.9
12	44.2	410	15.5
13	45.5	330	15.0
14	48.9	331,312	23.5
15	57.2	412	12.1
16	58.3	332	16.8
17	58.4	520,213	17.0
18	61.5	401	8.0

* Arbitrary Unit

Table C.3

X-Ray Diffraction Data for Fused Quartz Substrate, I_S

$2\theta(^{\circ})$	Intensity, I_S*	$2\theta(^{\circ})$	Intensity, I_S*
15	9.1	41	11.7
16	9.3	42	11.1
17	9.6	43	10.7
18	10.3	44	10.5
19	11.7	45	10.1
20	13.9	46	10.0
21	17.1	47	9.6
22	22.0	48	9.4
23	27.6	49	9.2
24	34.1	50	9.1
25	38.6	41	9.1
26	41.1	52	9.1
27	40.5	53	9.1
28	37.8	54	9.1
29	33.1	55	9.1
30	28.1	56	9.1
31	13.9	57	9.1
32	21.0	58	9.1
33	18.9	59	9.1
34	16.5	60	9.1
35	16.0		
36	15.1		
37	14.1		
38	13.5		
39	12.7		
40	12.1		

* Arbitrary Unit

Table C.4

X-Ray Diffraction Data of BST Film Specimen W12D
Annealed at 500°C

$2\theta(°)$	I_t	$I_f(=I_t-aI_s)$ *
15	5.9	0.0
16	7.4	1.4
17	11.1	4.9
18	16.9	10.2
19	23.9	16.3
20	30.7	21.7
21	36.6	25.5
22	41.8	27.5
23	45.5	27.6
24	48.4	26.2
25	49.9	24.8
26	50.3	23.6
27	49.1	22.8
28	46.3	21.7
29	41.9	20.4
30	37.5	19.2
31	26.4	17.4
32	28.4	14.7
33	24.7	12.4
34	22.4	11.7
35	20.7	10.3
36	19.4	9.6
37	18.5	9.3
38	17.5	8.7
39	17.0	8.7
40	16.4	8.5
41	15.6	8.0
42	15.1	7.9
43	14.8	7.8
44	14.2	7.4
45	14.2	7.4
46	14.0	7.4
47	13.9	7.7
48	13.9	7.8
49	13.9	7.9
50	13.9	8.0

*For calculating I_f, values listed
in Table B.2 are used for I_s and
absorption factor a=0.65 is
employed.

Table C.5

X-Ray Diffraction Data of BST Film Specimen W12G
Annealed at 800°C

Peak	2θ (°)	Index	I_t	$I_f(=I_t-aI)$ *
1	17.3	001	24.5	18.5
2	20.6	200	48.0	38.3
3	22.7	111	55.3	39.5
4	23.3	210	55.0	36.6
5	26.6	201	64.9	39.6
6	28.6	211	100.0	78.2
7	32.8	310	37.9	26.1
8	33.7	221,002	42.8	31.9
9	36.9	311,112	28.5	19.8
10	40.5	202	24.9	17.5
11	41.4	321,212	34.0	26.9
12	43.5	410	32.0	25.5
13	44.7	330	26.5	20.2
14	48.0	331,312	36.0	30.1
15	56.3	412	28.0	22.4
16	57.8	332	26.5	20.9
17	58.1	520,213	31.0	25.4

* For calculating I_f, values listed in Table B.2 are used
for I_s and absorption factor $a = 0.62$ is employed.

Table C.6

X-Ray Diffraction Data for BST Film Specimen W12H
Annealed at 900°C

Peak	2θ (°)	Index	I_t	$I_f (= I_t - aI_s)$ *
1	17.6	001	22.5	15.9
2	21.4	200	37.5	24.2
3	23.0	111	43.5	25.1
4	23.6	210	45.0	23.9
5	27.2	201	57.4	24.7
6	29.2	211	112.1	67.1
7	33.7	310	36.5	24.8
8	34.7	221,002	34.1	23.0
9	37.9	311,112	23.3	14.3
10	40.7	202	23.3	15.4
11	42.2	321,212	31.3	23.9
12	44.0	410	28.5	21.5
13	45.4	330	24.0	17.3
14	48.8	331,312	32.5	26.4
15	57.2	412	24.5	18.4
16	58.2	332	26.0	19.9
17	58.4	520,213	30.3	24.2
18	61.4	401	24.5	18.4

* For calculating I_f, values listed in Table B.2 are
used for I_s and absorption factor a=0.67 is employed.

Table C.7

X-Ray Diffraction Data for BST Film Specimen W12I
Annealed at 950°C

Peak	$2\theta(^\circ)$	Index	I_t	$I_f(=I_t-aI_s)$*
1	17.0	001	21.6	15.4
2	20.2	2-0	32.4	23.3
3	22.9	111	46.6	29.1
4	24.4	210	40.8	17.3
5	27.0	201	67.0	40.7
6	29.0	211	106.0	84.5
7	33.2	310	42.0	26.0
8	34.2	221,002	36.0	25.0
9	37.4	311,112	26.0	17.0
10	----	202	----	----
11	41.7	321,212	37.0	29.7
12	43.6	410	33.0	26.2
13	45.0	330	31.0	24.4
14	48.4	331,312	42.0	36.0
15	56.8	412	32.0	26.1
16	58.0	332	38.8	32.9
17	58.2	520,213	37.0	31.1
18	61.1	401	30.6	24.7

* For calculating I_f, values listed in Table B.2 are used for I_s and absorption factor a=0.65 is employed.

Three different computer programs were utilized for the separation of integrated intensities for the narrow Bragg peaks from the crystalline and for the broad peak from the amorphous. The narrow and broad peaks were fitted with Lorentzian and Gaussian curves, respectively (see 4.8.4.1). Computer program I is for the determination of the A_G, B_G and η_G for the Gaussian curve (See 4.8.4.1 (3) and (4)). Computer program II is for the determination of the twelve parameters such as A_G, B_G, η_G, A_i, B_i and η_i (i=1,2,3) (See 4.8.4.1 (7)), where A_i, B_i and η_i are parameters for Lorentzian curve. These computer programs are based on the method of least square. Finally, the theoretical x-ray diffraction patterns (See Figures 45 and 46) were determined by using computer program III. (See 4.8.4.1 (7)). These computer programs are shown on the following pages.

COMPUTER PROGRAM I

```
 1          DIMENSION XI(40),TT(40),AL(8),BL(5),RL(5),TTL(5),DXI
            (40),ALV(8)
 2          KVRVL=6
 3          READ(5,10) NEXD
 4    10    FORMAT(I10)
 5          DO 100 I=1, NEXD
 6   100    READ(5,11) XI(I),TT(I)
 7    11    RORMAT(2F10.2)
 8          READ(5,10) NBP
 9          DO 101 I=,NBP
10          READ(5,12) RL(I),TTL(I),AL(I)
11    12    FORMAT(3F10.4)
12          BL(I)=(AL(I)/RL(I))**2
13          AL(I)=AL(I)**3/(RL(I)**2)
14   101    ALV(I)=AL(I)
15          READ(5,12) BG,TTG,AG
16          M1=NBP+1
17          M2=NBP+2
18          M3=NBP+3
19          AL(M1)=AG
20          AL(M2)=BG
21          AL(M3)=TTG
22          ALV(M1)=AG
23          ALV(M2)=BG
24          ALV(M3)=TTG
25          SSDXI=1.0E20
26          ALV(KVRVL)=0.1*AL(KVRVL)
27   105    IF(KVRVL.LE.NBP) BL(KVRVL)=(ALV(KVRVL)/RL(KVRVL))**(
            2.0/3.0)
28          SDXI=0.0
29          DO 102 I=1,NEXD
30          DXI(I)=XI(I)
31          DO 103 J=1,NBP
32   103    DXI(I)=DXI(I)-ALV(J)/((TT(I)-TTL(J))**2+BL(J))
33          DXI(I)=DXI(I)-ALV(M1)*EXP(-ALV(M2)*(TT(I)-ALV(M3))**2)
34   102    SDXI=SDXI+DXI(I)**2
35          SL=0.0
36          DO 106 ISL=1,NBP
37   106    SL=SL+ALV(ISL)/SQRT(BL(ISL))
38          SL=3.141592653*SL
39          SG=1.772453851*ALV(M1)/SQRT(ALV(M2))
40          WRITE(6,13)
41    13    FORMAT(//)
42          WRITE(6,14) (ALV(I),BL(I),TTL(I),I=1,NBP)
43    14    FORMAT(3F15.4)
44          WRITE(6,15) ALV(M1),ALV(M2),ALV(M3),SDXI
45    15    FORMAT(3F15.4,5X,E16.7)
46          WRITE(6,16) SL,SG
47    16    FORMAT(' SL=',E16.7,5X,'SG=',E16.7)
48          IF(SDXI.GT.SSDXI) GO TO 104
49          SSDXI=SDXI
50          ALV(KVRVL)=ALV(KVRVL)+0.01
51          GO TO 105
52   104    STOP
53          END
```

COMPUTER PROGRAM II

```
 1        DIMENSION XI(40),TT(40),AL(8),BL(5),RL(5),TTL(5),DXI
          (40),ALV(8)
 2        KVRVL=3
 3        ALHS=0.5
 4        ALHE=0.8
 5        AGS=18.0
 6        AGE=20.0
 7        GCNST=8.5209
 8        NMASU=11
 9        NMBSU=11
10        READ(5,10) NEXD
11   10   FORMAT(I10)
12        DO 100 I=1, NEXD
13  100   READ(5,11) XI(I),TT(I)
14   11   FORMAT(2F10.2)
15        READ(5,10) NBP
16        DO 101 I=1,NBP
17        READ(5,12) RL(I),TTL(I),AL(I)
18   12   FORMAT(3F10.4)
19        BL(I)=(AL(I)/RL(I))**2
20  101   AL(I)=AL(I)**3/(RL(I)**2)
21        READ(5,12) BG,TTG,AG
22        M1=NBP+1
23        M2=NBP+2
24        M3=NBP+3
25        AL(M1)=AG
26        AL(M2)=BG
27        AL(M3)=TTG
28        HL=ALHS/AL(KVRVL)
29        EL=ALHE/AL(KVRVL)
30        DO 200 I1=1,NMASU
31        FC=HL+((EL-HL)/FLOAT(NMASU-1))*FLOAT(I1-1)
32        DO 201 I2=1,NBP
33        ALV(I2)=FC*AL(I2)
34  201   BL(I2)=(ALVI2)/RL(I2))**(2.0/3.0)
35        DO 200 I3=1,NMBSU
36        ALV(M1)=AGS+(AGE-AGS)*FLOAT(I3-1)/FLOAT(NMBSU-1)
37        ALV(M2)=(GCNST/ALV(M1))**2
38        ALV(M3)=AL(M3)
39        SDXI=0.0
40        DO 102 I=1,NEXD
41        DXI(I)=XI(I)
42        DO 103 J=1,NBP
43  103   DXI(I)=DXI(I)-ALV(J)/((TT(I)-TTL(J))**2+BL(J))
44        DXI(I)=DXI(I)-ALV(M1)*EXP(-ALV(M2)*(TT(I)-ALV(M3))**2)
45  102   SDXI=SDXI+DXI(I)**2
46        SL=0.0
47        DO 106 ISL=1,NBP
```

(COMPUTER PROGRAM II CONTINUE)

```
48 106    SL=SL+ALV(ISL)/SQRT(BL(ISL))
49        SL=3.141592653*SL
50        SG=1.772453851*ALV(M1)/SQRT(ALV(M2))
51        WRITE(6,13)
52   13   FORMAT(//)
53        WRITE(6,14) (ALV(I),BL(I),TTL(I),I=1,NBP)
54   14   FORMAT(3F15.4)
55        WRITE(6,15) ALV(M1),ALV(M2),ALV(M3),SDXI
56   15   FORMAT(3F15.4,5X,E16.7)
57        WRITE(6,16) SL,SG
58   16   FROMAT(' SL=',E16.7,5X,'SG=',E16.7)
59 200    CONTINUE
60        STOP
61        END
```

COMPUTER PROGRAM III

```
 1        DIMENSION REAL PI(150),PJ(150),PK(150),AG(150),EXPT(150)
 2        DO 10 I=1,120
 3        X=15.0+I*0.1
 4        PI(X)=AL1/(BL1+(X-TTL1)**2)
 5        PJ(X)=AL2/(BL2+(X-TTL2)**2)
 6        PK(X)=AL3/(BL3+(X-TTL3)**2)
 7        AG(X)=AG*EXP(-BG*((X-TTG)**2))
 8        EXPT(X)=PI(X)+PJ(X)+PK(X)+AG(X)
 9        PRINT,X,PI(X),PJ(X),PK(X),AG(X),EXPT(X)
10   10   CONTINUE
11        STOP
12        END
```

VITA AUCTORIS

1958	On 26th July, born in Nagasaki, Japan.
1976	Graduated from Omura High School, Nagasaki, Japan.
1981	Graduated from Kyusyu Institute of Technology, Kitakyusyu, Japan with a degree of B.E. in Metallurgical Engineering.
1982	Accepted into the Graduate School of the University of Windsor as a candidate for the degree of M.A.Sc. in Engineering Materials.